Politecnico di Torino

Master of Science in Automotive Engineering

Politecnico
di Torino

Master's Degree Thesis

Design of modular battery system for low voltage battery electric vehicle

Supervisors

Prof. Andrea Tonoli

Dott. Stefano Favelli

Dott. Raffaele Manca

Dott. Eugenio Tramacere

Candidate

Marco Rubechini

304559

July 2024

A Cecilia

Abstract

The importance of environmental concerns has become one of the most relevant and discussed subject in recent years. New targets for vehicle emissions are getting so stringent, that electrification of the powertrain represents the only realistic and feasibile solution for the near future. Despite the maturity of conventional internal combustion engines technology, and the existing distributed refueling infrastructures, ICE are obviously incapable of meeting the zero-emission limitations established by the European community for 2035 (engine ban). However, eliminating liquid fossil fuels is not an easy goal to be reached, and several challenges must be addressed to meet and fulfill customer needs, which can't be ignored in this electrification process. Main drawbacks of battery electric vehicles (BEVs) include the limited vehicle range and charging times. Particularly due to the latter reason, combined with a generally high purchasing price, many customers nowadays refrain from switching to electric cars. A promising alternative to conventional charging that can be exploited to address this problem is Battery Swap. The objective of this thesis is to design a low-voltage swappable modular battery system suitable for integration into the FIAT 500e, ensuring flexibility of the battery pack for both urban (frugal configuration) and extra-urban (dual configuration) missions. An initial battery sizing analysis has been performed to fulfill the requirements concerning vehicle range and battery capacity, identifying the best cell in terms of weight and costs. Subsequently, a comprehensive thermo-electrical model of battery cell is formulated, and validated using a cell available on the market for which a complete datasheet and experimental results were provided. The validated system is then exploited to predict the thermal behavior of the previously defined optimal cell for the proposed application of low voltage vehicle.

Table of Contents

List of Tables

List of Figures

Acronyms

BaaS Battery as a Service

BEV Battery Electric Vechicle

BMS Battery Management System

BSS Battery Swap Station

BTMS Battery Thermal Management System

DLC Direct Liquid Cooling

ECM Equivalent Circuit Model

EV Electric Vechicle

LIB Lithium Ion Battery

NEDC New European Driving Cycle

NMC Nichel Manganese Cobalt

OEM Original Equipment Manufacturing

ODE Ordinary Differential Equation

PCM Phase Change Material

RMSE Root Mean Square Error

SOC State of Charge

SOH State of Health

TtW Tank to Wheels (emissions)

WLTC Worldwide Harmonized Light-vehicles Test Cycle

WtT Well to Tank (emissions)

Nomenclature

A_{air}	Surface of convection heat transfer cell air
$A_{\text{air-cp}}$	Surface of convection heat transfer cold plate air
A_{cond}	Surface of conduction heat transfer
C	Cell capacity
C_1	Cell transient response in charging and discharging
C_2	Cell polarization characteristic
C_{cell}	Cell heat capacity
C_{cp}	Cold plate heat capacity
c_{cell}	Cell specific heat capacity
c_{cp}	Cold plate specific heat capacity
ΔS	Entropy change
E_{cond}	Thermal energy dissipated by conduction
E_{conv}	Thermal energy dissipated by convection
E_{tot}	Total thermal energy dissipated
F	Faraday number
h	Convection heat transfer coefficient of air
i	Current
k_{cell}	Thermal conductivity of the cell
k_{cp}	Thermal conductivity of the cold plate
λ	Thermal inertia of the cold plate

m	Cell mass
m_{cp}	Cold plate mass
n	Number of electrons for the reaction
$\dot{Q}$	Thermal power absorbed
$\dot{Q}_{\text{cond}}$	Cell conductive thermal dissipated power
$\dot{Q}_{\text{cond-cp}}$	Cold plate conductive thermal dissipated power
$\dot{Q}_{\text{conv}}$	Cell convective thermal dissipated power
$\dot{Q}_{\text{conv-cp}}$	Cold plate convective thermal dissipated power
$\dot{Q}_{\text{entropy}}$	Thermal power generated for entropy change
$\dot{Q}_{\text{in}}$	Thermal power generated
$\dot{Q}_{\text{joule}}$	Thermal power generated for joule effect
$\dot{Q}_{\text{out}}$	Thermal power dissipated
ρ	Density of cold plate material
R	Electrical resistance
R_{cond}	Equivalent conductive thermal resistance cell coldplate
$R_{\text{cond-cp}}$	Equivalent conductive thermal resistance coldplate cell
R_{conv}	Equivalent convective thermal resistance cell air
$R_{\text{conv-cp}}$	Equivalent convective thermal resistance coldplate air
R_1	Cell electrochemical polarization resistance
R_2	Cell concentration polarization resistance
R_{int}	Cell internal resistance
s_{cell}	Cell height
s_{cp}	Cold plate thickness
T_0	Initial temperature of the cell
T_{air}	Temperature of the air
T_{cell}	Temperature of the cell
T_{cp}	Temperature of the cold plate

T_{cp0}	Initial temperature of the cold plate
t	Time
τ	Time constant
τ_{th}	Thermal time constant
V	Cell output voltage
V_1	Voltage drop of the first RC branch
V_2	Voltage drop of the second RC branch
V_{ocv}	Open circuit voltage

Chapter 1

Introduction

The existing propulsion system based on Internal Combustion Engine has reached a high maturity level in the years, but considering the increasingly stringent regulations on engine emissions, it's evident that shifting towards the electrification of powertrains is the sole feasible option in the near future.

According to the European Commission, nowadays passenger cars and vans are responsible for the 19% of the total EU emissions of CO_2, the predominant gas directly correlated to the greenhouse effect.

The latest regulations within the European community, implemented in 2020, stipulate that passenger cars must adhere to an emissions limit of 95 gr of CO_2/km, while vans are subject to a limit of 147 grams of CO_2/km [1]. Looking ahead, from 2025 through 2029, a 15% reduction in these emission limits has been provided, translating to 81 gr of CO_2/km for passenger cars.

These reductions will be assessed through homologation tests that will now be based on WLTC cycles, departing from the previous reliance on NEDC cycles. Due to the higher average speeds, more realistic acceleration profiles and the almost total absence of idle conditions, the WLTC cycle simulates better the real world driving conditions and allows more accurate and reliable results. As a result even

if the ICE works more efficiently in this new driving cycle, the energy demand is much higher and as consequence, also CO_2 emissions for the same engine will result higher compared to the NEDC cycle.

The imperative for powertrain electrification arises not just from the steadily tightening emissions standards (further reductions on CO_2 emissions by 55% from 2030 to 2034), but primarily from the engine ban set for 2035 by the European community, that establishes zero emissions (0g CO_2/km) for all vehicle types, independently of their weight.

For this reason fossil fuels are unsustainable in the foreseeable future and even hybrid vehicles, currently considered as the best compromise between consumer needs and environmental needs, will inevitably yield market dominance to fully electric alternatives.

The most notable advantage of electrification of transportation is its comprehensive environmental benefits, including the elimination of noxious emissions, noise pollution, and carbon dioxide emissions at the local level (zero Tank to Wheel - TtW - emissions). In terms of performance, electric motors offer instant high torque at very low speeds, leading to superior acceleration, climbability, elasticity, and smoothness compared to internal combustion engines (ICE).

Also engine efficiency is a key feature of electric motors, which can convert over 70% of electrical energy from the grid into power at the wheels; in contrast, internal combustion engines (ICE) convert approximately 20% of the energy stored in fossil fuels into usable power at the wheels.

Furthermore, electric motors enable regenerative braking, which allows the recovery of part of the kinetic energy that would otherwise be completely dissipated, as happens with traditional mechanical brakes. This recovered energy is then converted into electrical energy, which can be used to recharge the vehicle's batteries.

However, the shift towards electrification is not straightforward: in order to reach

the goal of zero emissions, despite the numerous benefits of electric vehicles, significant challenges must be addressed.

From an environmental standpoint, EVs guarantee zero emissions only at the local level. When considering a broader perspective, emissions include not just tank-to-wheel but also those associated with the production of batteries and electricity. Therefore, it is incorrect to claim that electric transportation produce zero emissions on a global scale, as we must account for well-to-tank (WtT) emissions, which - even for EVs - are not negligible. Lastly battery manufacturing and recycling processes are not mature yet and improvements are still needed.

It is important to note that environmental and social needs differ from those of private end users, whose requirements must be met to promote the widespread adoption of EVs.

One major obstacle is the higher initial cost and purchase price of EVs compared to ICE vehicles, that makes them not affordable by everyone. Additionally, the vehicle range is more limited than ICE vehicles due to the lower specific energy and energy density of batteries compared to fossil fuels. Despite substantial progresses in recent years, nearly quintupling the energy storage capacity of batteries, we are still far from the energy density (kWh/kg) of fossil fuels.

Another critical issue is the availability of infrastructure and the widespread network of recharging stations, particularly in rural or less developed areas, which makes customers less comfortable in choosing to switch to an electric vehicle.

Lastly, the charging time is a significant concern: recharging batteries takes considerably longer than refueling ICE vehicles.

To address the issues of range anxiety and lengthy charging times, and to make electric vehicles more appealing to potential future customers, battery swapping technology offers a promising solution.

With this approach, drivers do not need to wait at charging stations. Instead,

in the Battery Swap Station (BSS) the depleted battery is quickly replaced with a fully charged one, in a process that takes about the same amount of time as refueling at a traditional gas station.
This technology, while not yet fully mature, is gaining traction worldwide, with numerous companies —both startups and established automotive firms— actively involved.
Stellantis, as we will discuss later, has established a partnership with Ample in order to produce an initial fleet of 100 FIAT 500e equipped with this technology, for a car-sharing service in Madrid by the end of the year.
However, despite the advantages of battery swapping, numerous challenges must still be addressed for this technology to achieve widespread adoption. These issues will be explored in detail in the next chapter.

1.1 Objectives

This work investigates the feasibility of converting a FIAT 500e into a vehicle suitable for battery swapping. The focus, is on defining a proper low-voltage swappable modular system that can be adapted according to the mission that has to be satisfied: a single module for urban missions (frugal configuration), and a dual module for extra-urban missions (dual configuration).
In both scenarios battery system must meet the requirements both in terms of WLTC range and battery capacity. Detailed specifications will be provided in the preliminary battery sizing section.
Currently the 500e is equipped with a lithium battery with SAMSUNG 63Ah NMC622 prismatic cells. The project aims to identify alternative cell types available on the market, which can satisfy not only the previously mentioned requirements but which at the same time have a lower weight and reduced costs. This is not only to lighten the vehicle and make it less energy demanding, but above all to

facilitate the battery replacement process, which would otherwise be more complex with heavier batteries.

The second objective of this thesis project is to develop a comprehensive thermo-electrical model of the battery cell and subsequently validating this model through experimental data.

However, due to the challenging availability of the chosen cell, the thermal model and experimental validation has been conducted using the cylindrical SAMSUNG INR 21700 30T for which experimental results and complete datasheets were provided. Nonetheless, once the accuracy of the thermal model is confirmed, we can ascertain its broader applicability: the aim is to validate the thermodynamic equations of the model, which do not depend on the specific type of cell utilized. It will be then possible to simply adjust the input data of the code to generate the thermal model for any desired cell.

Predicting the thermal evolution of battery cells according to the different current profiles will be fundamental for determining as future work which would be optimal cooling method for the new battery pack to be installed in the 500e revealing whether air cooling is adequate or if liquid cooling is necessary. One of the critical challenges addressed in the following chapter in fact is the integration of the cooling system into the battery pack, a crucial aspect for battery swap to be considered.

1.2 Overview

A short overview of this work is here reported, before diving in to the detailed project. After this short Introduction, the first chapter is the State of the Art, in which an in-depth description and analysis of Battery Swap is presented, defining the levels of automation of the process and identifying the different typologies of solutions. Also the challenges to be faced are highlighted in order to make a better

understanding of which are the problems that still have to be solved to promote the diffusion of this technology.

In particular the cooling of the battery is a critical aspect to be taken into account when we talk about battery swap, and a dedicated section for this will be presented. The review is then concluded with a brief description of the existing solutions and the companies involved in this field.

Chapter Three details the methodology and overall procedures employed to achieve the desired results. The chapter begins with a preliminary battery sizing, analyzing various battery cells available on the market to identify potential battery packs suitable for the 500e. This analysis aims to determine the optimal solution in terms of feasibility, weight, and cost.

Once the optimal cell is selected, and the corresponding battery pack configuration for both frugal and dual conditions is defined, geometric constraints are considered. The focus is on the battery pack, utilizing the available chassis space of the 500e without requiring additional modifications.

The chapter then introduces the thermal model, starting with the formulation of the initial equations and their implementation in MATLAB and Simulink. Initial analyses explore different scenarios, considering convection with air and conduction with a cold plate at both constant and variable temperatures.

A more realistic thermo-electric system is then developed, by varying the internal resistance (R_{int}) of the battery pack according to the state of charge (SOC), rather than treating it as a constant. The thermal model is integrated as a subsystem within the overall model and combined with an equivalent circuit battery model.

Chapter Four presents the validation of this model through the analysis of the simulation results obtained on the cylindrical SAMSUNG IN21700 30T cell and comparing them with the experimental data from previous laboratory studies.

Subsequently, the focus shifts to the prismatic CALB L221N147A, which is the

cell identified as optimal solution for our application. The evolution of the cell temperature is analyzed together with the temperature evolution of the cold plate using the validated model. The chapter is concluded with the sensitivity analysis conducted to examine the impact of cold plate thickness and material on system thermal behavior. The final chapter summarize the main findings and outline potential future research directions in the "Future Works" section.

1.3 Overview of MOST- Spoke 2

This work has been developed in the framework of MOST -Centro Nazionale per la Mobilità Sostenibile - and in particular in the context of Spoke 2, called "Sustainable Road Vehicles".

The center is financed by the European Community with the funds of PNRR -Piano Nazionale di Ripresa e Resilienza- and collaborates with CNR and other important universities including Politecnico di Torino.

It focuses its work and effort in several specific areas and sectors with the aim of realizing a green and sustainable mobility. In particular, the goal of Spoke 2 of MOST is to develop new vehicle concepts to reduce the impact of the transport system on global emissions. The idea is that small, light, reconfigurable vehicles integrated into data and charging networks are an answer to creating an environmentally, economically and socially sustainable transport system [2].

Current efforts are concentrated on developing zero-emission vehicle architectures which include high-efficiency electric and hydrogen engines but also the integration of assisted and autonomous driving technologies.

Innovations extend beyond the powertrain to other vehicle components, such as tyres and suspensions, that can be transformed into efficient solutions aimed at improving not only performances, but also sustainability. In fact ensuring a circular economy for these components is another crucial objective of Spoke 2.

When talking about sustainable mobility, integrating vehicles into charging infrastructures is essential, and the expansion of the network in both urban and rural areas is clearly needed.

MOST operates also towards the development of smart charging solutions designed to optimize energy consumption and promote economic growth. Wireless charging represents a possible alternative to conventional charging, but Battery Swap technology is the most promising solution that has garnered increasing interest in this field in recent years. In particular the goal of this work is the development of a low-voltage battery pack suitable for this application. Among the several advantages of low voltage battery systems (systems characterized by V_{dc}<60, also indicated as A class systems), safety is for sure the most important one and the first to be mentioned: with low voltage batteries the risk of electric shock is almost null and this means that there is no need of electrical isolation or mechanical protection and shielding.

For this reason simpler and cheaper electronics can be used, significantly reducing costs with respect to high voltage systems. The much more limited number of components, leads not only to an easier integration of A class systems on existing vehicle electronic setup, but also to a simpler maintenance and a significant weight reduction. For all these reasons, low voltage batteries represent the best solution in terms of modularity for realizing swappable battery systems, especially due to their versatility in different configurations.

The main challenge to be addressed when dealing with low voltage systems are the high currents: reducing the voltage inevitably leads to higher C-rates to reach the same output required power. For this reason the definition of a valid thermal model, capable of predicting the thermal behavior of the pack under demanding current profiles, is needed to determine if the battery designed is suitable for this challenging application. The project presented in this thesis is part of the research

activities carried out in collaboration between Politecnico di Torino and CRF - Centro Ricerche Fiat- both involved in the PNRR Spoke 2 of MOST project.
CRF is a research and development organization affiliated with FCA - Fiat Chrysler Automobiles - now part of the Stellantis group. It collaborates with international research programs and partners with automotive companies and academic institutions. The aim of CRF is guaranteeing the competitiveness of Stellantis in the automotive industry with the development of innovative and sustainable technologies that can also enhance vehicle performance and efficiency.

Chapter 2

State of the art

We have already mentioned in the introduction that electrification of transportation is the only viable solution to achieving zero emissions by 2035. To attain this objective and facilitate a broader adoption of battery electric vehicles (BEVs), a comprehensive and expansive charging infrastructure is essential, which has to be postulated also by potential vehicle buyers [3].

Establishing a widespread network of charging stations presents significant challenges, particularly in rural areas, also considering the high costs associated with developing new infrastructures. Consequently, it is difficult to precisely determine the required amount of public charging stations but studies have demonstrated that the demand for charging can exceed the effective charging need.

This perception of abundant charging options positively influences the intent to purchase BEVs and can attract additional customer segments. The presence of charging stations and the compatibility of connectors are crucial elements that influence the charging experience for electric vehicle owner [4]

2.1 Classification of charging infrastructures

Charging systems can be classified into public charging stations if located in public areas available to everyone, and home charging stations if they are installed in private properties.

When we talk about charging infrastructures we can consider different possible solutions and make a distinction between on-board charging systems, mainly home charging stations, and off-board charging systems. The first one is typical of conductive complete charging and it's usually referred as AC charging, since the current flowing in the cable is an AC signal. The latter one instead is the typical solution for partial fast charging and it's generally referred as DC charging, since the conversion from AC to DC is already performed in the charging station and not on-board.

Both of these two solutions present advantages and also some drawbacks. As highlighted by Dini et al.[5], public off-board charging stations offer the advantage of fast charging speeds, making them ideal for long-distance travel and compatible with a wide variety of vehicles. However, they can be more expensive than home charging due to usage fees, and their benefits may be diminished in areas with congested charging spots.

On the other hand, on-board home charging allows vehicle owners to keep their vehicles ready without the need of going to public charging stations, and it can also result in lower long-term costs since charging can be scheduled for nighttime when energy rates are cheaper. The downsides include a high initial installation cost and a slower charging speed compared to DC fast charging.

2.1.1 Wireless Charging

When discussing charging infrastructures, the focus is typically on conductive charging. However, other options, although not yet widespread, do exist.

One such option is wireless charging, which can be a smart solution to consider. This method involves partial on-board charging, where power transfer occurs between a transmitting coil (Primary Stage), embedded in the ground and a receiving coil (Secondary Stage), on the vehicle floor.

Figure 2.1: Wireless Charging

With this technology short stops at traffic lights and intersections can be leveraged to maximize charging efficiency, minimize delays, and reduce costs [6]. In this case we talk about stationary wireless charging.

Nevertheless, establishing an appropriate energy scheme for wireless charging infrastructure is not an easy task but an important challenge to be faced. Dynamic wireless charging instead allows the vehicle to charge while driving at a constant speed in a dedicated lane equipped with the charging system.

However, Panchal et al. [7] have listed some main drawbacks of this technology, such as the limited power transfer due to the air gap between the coils and their potential electromagnetic incompatibility and misalignment. Moreover, wireless charging is predominantly feasible in large cities with intersections and traffic lights, but becomes impractical in rural and less developed areas, thus failing to alleviate

customer concerns about the availability of charging infrastructures in such regions.

2.1.2 The risk of Lithium Plating

As previously discussed, a primary concern for customers regarding electric vehicles (EVs) is the lengthy battery charging times. DC fast charging, through high current rates, aims to address this issue, but it still cannot match the speed of refueling internal combustion engine (ICE) vehicles. Additionally highly efficient batteries are required, as well as a forced cooling system, due to significant charging losses. Fast charging also poses challenges such as accelerated aging and reduced capacity of lithium-ion batteries: high C-rates can lead to lithium plating instead of intercalation on the carbon anode, accelerating performance degradation and raising reliability concerns.

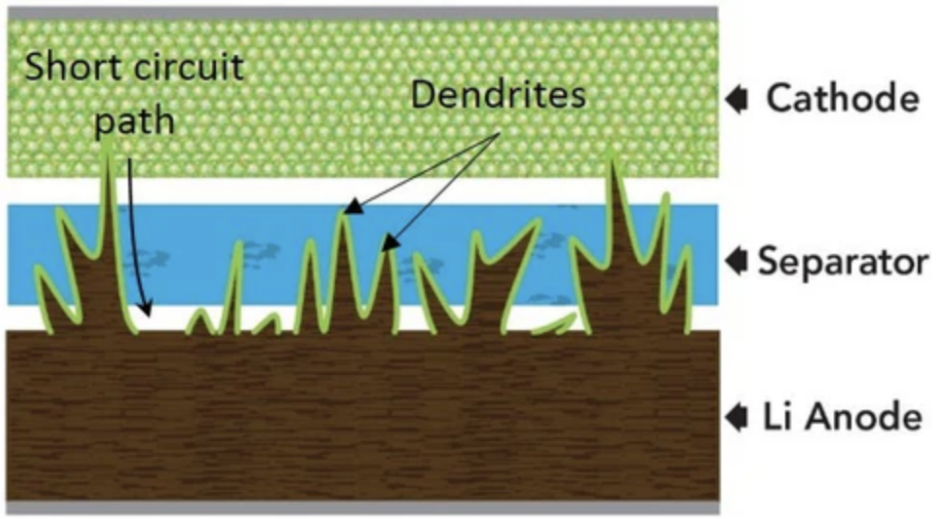

Figure 2.2: Dendritic Lithium

Lithium plating consists in metallic lithium deposition on the anode in the form of dendrites and it is the major cause of battery aging and safety incidents for LIBs[8]. This not only diminishes battery capacity but dendritic lithium can also

pierce the separator, inducing internal short circuit by creating a direct connection of conductive material between anode and cathode.

Lithium deposition is an exothermic reaction, with the risk of generating excessive heat that can lead to an uncontrollable rise in temperature and pressure within the battery, potentially resulting in thermal runaway. Lithium plating is particularly critical with graphite anodes and tends to occur under specific conditions, notably at high C-rates, at high SOC (battery is overcharged) and low charging temperatures. Moreover as presented by Bugga et al. [9], the effects are not fully reversible during the subsequent discharge phase.

Another alternative to conductive and wireless charging, without having the drawbacks of fast charging, is Battery Swapping. This work focuses on this emerging technology and as aforemetioned, Stellantis plans to produce a fleet of one hundred 500e based on battery swapping by the end of the year.

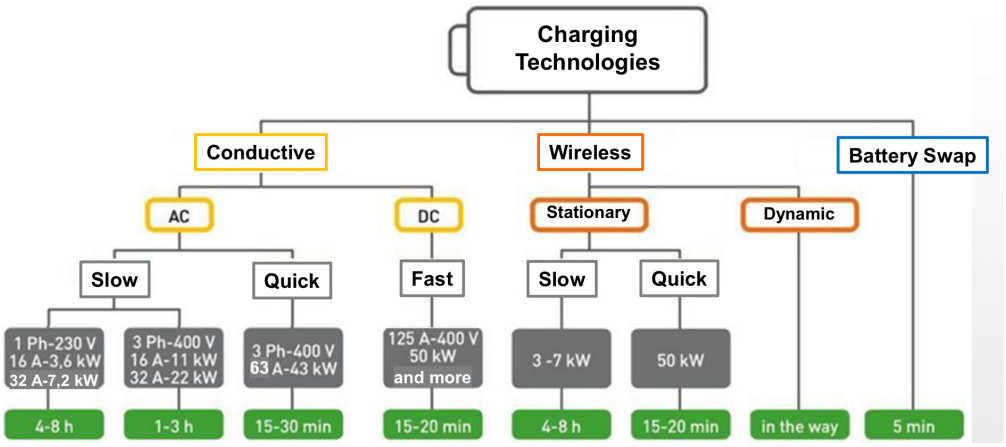

Figure 2.3: Existing Charging technologies

2.2 Background of Battery Swap Technology

As we said, battery swapping is currently one of the most promising technologies for addressing the issues of range anxiety and charging times in electric vehicles (EVs).

The vehicle enters inside a Battery Swap Station (BSS) and the discharged battery is replaced with a fully charged one in few minutes (comparable with the refuelling time of ICE vehicles) without reducing battery life as occurs with DC fast charging. With the development of this new technology, it is essential to establish a corresponding, adequate, and comprehensive infrastructure to support a widespread adoption and functionality of battery swap. This network must include strategically located battery swap stations, robust communication systems for real-time monitoring and management, and efficient logistics for battery storage and transportation. Without this infrastructural system, the full potential of the technology cannot be realized, and its benefits couldn't be fully exploited.

Thus the demand for battery charging must be estimated by using historical data, to prevent congestion at battery swap stations and associated delays. Battery usage trends have to be identified, giving a prediction on the peak times and on the sufficient number of available charged batteries when the demand is the highest, not to make drivers experience long waiting times. Furthermore, accurate planning and forecasts would determine allow for better resource allocation and planning, reducing operational costs and improving the overall user experience.

2.2.1 Insights into the battery swapping procedure

We can now discuss in detail how the swapping process is performed, making reference to the work of Adegbohun et al. [10], which illustrates Tesla's BSS as case study and provides insights into its operational mechanics.

To initiate the battery swapping process, the vehicle sends a notification to the

station asking for the availability of a charged battery ready for the swap. Once confirmation has been received the vehicle enters inside the station and climbs a slight ramp, before stopping on a dedicated swapping platform. The engine is switched off and the car is raised up by a vehicle lift to facilitate the replacement procedure. Horizontal doors underneath the vehicle are opened, granting access to the battery compartment and a robotic arm removes the depleted battery. It's then replaced with a charged one taken from the storage rack, where the batteries ready for the swap are stored, and after the swap is performed, the fasteners are engaged and the doors are closed.

As soon as the process is completed, The vehicle is then lowered back to ground level and ready again to travel with a fully charged battery. The depleted battery that has been substituted is checked , and its state of charge (SOC) and state of health (SOH) are monitored, as well as its battery age and the number of charging and discharging cycles undergone.

It's then important to charge it immediately, to satisfy the swapping demand of other drivers approaching the station without incurring in delays.

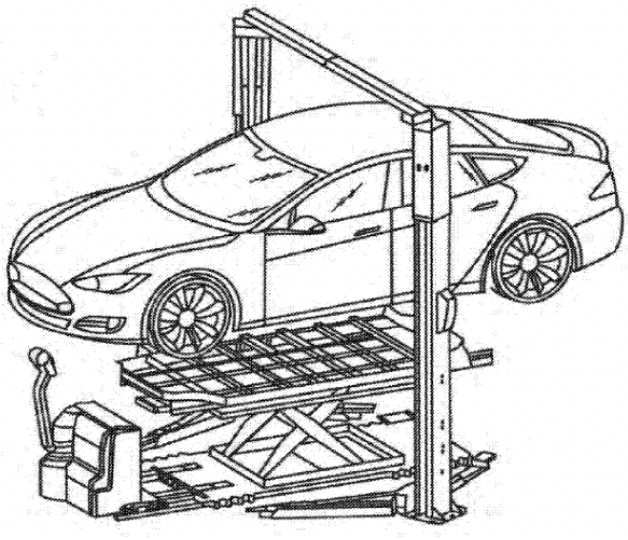

Figure 2.4: Tesla Battery Swap Station [10]

2.2.2 Different Battery Swapping techniques

The described process presented by Tesla is an automated bottom swapping, which is the most common solution in this field for passenger EVs. But it's important to underline that battery swap can be performed with different levels of automation:

- Manual battery swapping:
  Battery swapping is performed manually by a human operator without any automation in the process. Time and costs in this case are increased due to the involvement of manpower and this solution is only feasible for small light modular batteries.

- Assisted battery swapping:
  In this partially automated swapping, the machine and manpower collaborate in the process. Most of the activities are performed by the robots, especially battery removal and transport, but some human assistance and occasional interventions are required.

- Fully automated battery swapping with human supervision:
  The battery pack is replaced without any interference of manpower but human supervision is still required. This is the level of automation presented previously in the Tesla example and represents the State of the Art of Battery Swap Stations.

- Fully automated battery swapping without human supervision:
  In this case no human effort is required; the process is completely automated and the system doesn't even need to be controlled remotely. This solution is not feasible yet but represents the future vision of BSSs, in which robotics can cooperate with AI.

The different swapping techniques can be discriminated also according to the

position of the battery in the vehicle and the point of application of the robotic arm [11].

- Sideways Swapping:
  This type of solution could be ideal for vans or vehicles with very low ground clearance, as it eliminates the need for lifting the car. For this reason sideways swapping is suited for realizing BSS in narrow spaces, as it only requires lateral motion, but not vertical one. The risk of having a battery mounted in this position however is that in case of lateral collision, it's much more difficult to guarantee the integrity of the battery compartment.

- Rear Swapping:
  This solution could be adopted for vehicles in which the battery is mounted in the back. Also in this case no significant vertical space is required inside the BSS as well as no lateral clearance. But additional space behind the car would be needed to accommodate the robotic arm for extracting the battery and replace it with a new one. Also in this case it's difficult to preserve the integrity of the battery compartment in case of rear collision.

- Top Swapping:
  In this case the batteries are placed below the roof and are much more protected in case of impact, but the battery compartment inevitably increases vehicle height, aerodynamics and can affect also vehicle aesthetic. For this reason this is the most suitable solution for electric buses, since there are no particular requirements on aesthetics and also because there is no need of lifting the vehicle; the weight of a bus couldn't be sustained by the lifting platform.

- Bottom Swapping:
  It is the most promising solution for passenger cars, and it's used as standardized approach by major battery swapping companies. With this technique,

the battery can be placed in the floor frame and reinforced on the sides, such that the integrity of the battery compartment in case of lateral collision can be guaranteed. But as drawbacks, a certain ground clearance must be present to ensure the access to the battery for maintenance or in case of emergency and furthermore a lifting platform is required, increasing the cost and the complexity of BSS.

It's evident that the choice of the swapping technique depends on vehicle design and infrastructure capabilities, but the coexistence of different solutions may represent a challenge for the need of battery swap standardization, which will be discussed in detail in the dedicated section of battery swap challenges.

2.2.3 Battery Swap Station Models in academic research and their advantages

The efficiency of Battery Swapping is particularly beneficial whenever maintaining a consistent operational schedule is crucial.
As a result, for example, it is progressively gaining acceptance among shuttle bus services[12]. Public transportation in fact, features predefined routes, schedules and service hours, making easy and predictable to plan where the BSSs must be located and when the swap has to be performed during the day, minimizing the stoppage time. The ability to quickly swap out depleted batteries for fully charged ones ensures that shuttles can remain in continuous operation without losing time for charging, enhancing overall fleet productivity. For this reason battery swap for electric public transport is becoming more appealing than conventional charging.
Jain et al.[13] presented battery swapping stations as a fascinating solution for powering electric vehicles (EVs). This technology can eliminate the problem of long waiting times and reduce the demand at conventional charging stations, providing benefits not only for battery swapping vehicles but also for those using traditional

charging methods. The ease and speed of changing the battery can also alleviate range anxiety by reducing concerns about running out of charge during long trips. Other significant benefits of battery swap in the EV driver's point of view have been investigated by Arora et al. [14]. The cost of EVs can be tremendously reduced when the battery is leased rather than purchased, as it is the core of EV's cost representing between the 25 and 50% of the price.

With this technology in fact, the battery is not necessarily owned by the driver when purchasing the vehicle (see the dedicated section Battery as a Service -BaaS-), as it needs to be swapped. This approach makes the vehicle much more affordable to a larger customer segment, thereby promoting sustainable mobility. Initial costs when purchasing an EV could be further reduced even because with battery swap the owner doesn't need to install a charger at his place. However, issues related to battery ownership, which will be discussed in the challenges section, can arise.

Additionally swapping offers longer battery life not only because batteries are charged independently and optimally as per the maximum battery life, but also because of centralized maintenance, since regular checks on battery state of health are performed at the BSS.

Different features of BSS have been investigated. For example, in the study proposed by Wu et al. [15], EV drivers should send an advance notice to the battery swapping station where they intend to swap their battery. This notice should include the estimated arrival time, the remaining battery capacity, and its state of health (SOH). The BSS then would use these infos to determine the charging schedule through a mathematical optimization algorithm.

The goal of this algorithm is to minimize operational costs, which depend on factors such as the number of batteries being charged, the potential damage from varying charging rates and the costs of electricity. With the algorithm it's possible to obtain a wise BSS energy usage, by charging depleted batteries in the off-peak hours if

possible, or when the rates for the electricity are cheaper.
Battery Swap can have also environmental benefits since a centralized management of batteries facilitates efficient recycling and disposal.
Sarker et al.[16] highlighted how BSS could maximize profits by providing not only charged batteries but also services to the infrastructure system, such as voltage support, regulation reserves or energy arbitrage.
To improve the coverage and service of BSSs, an effective idea is to switch from passive battery swapping mode, to an active one: the EV battery swapping device can be installed on an electric van, which is transformed into a mobile BSS [17].
Differently from the passive battery swapping that has been discussed up to now, the mobility of the van removes the constraints of location of BSS: the driver doesn't need to travel to the closest BSS, but thanks to this solution energy replenishment can be performed anytime and anywhere.
This solution has been developed to address the problem of range anxiety: the EV users can decide: i) to stop to a conventional BSS, ii) to wait for a battery swapping van, iii) to keep driving until the van catches up with them. In this model in fact, the van would be equipped with a GPS positioning and communication system through which it can communicate to the battery swapping service management and the EV users current informations on its position, direction, and battery storage levels. On the other side the user that calls the service, has to communicate his speed, direction and position as well as the level of SOC of his vehicle battery. The battery is swapped only if the SOC is lower than a certain threshold, not to limit its service life.
The van is then refilled with charged batteries at the BSS or directly at the battery factory; the amount of time required for this process depends on the amount of battery swapping requests and on its distance to the BSS.
The main limit of this solution proposed however, is that the vans would have a

much more limited capacity of storing charged batteries compared to conventional BSS and they could serve only a limited number of EVs; for this reason the service area should be divided in small districts, each of them served by a specific number of vans.
Nevertheless, this active battery swapping solution remains highly futuristic and will not be further examined in this thesis.

2.3 Battery Swap Challenges

We have discussed the benefits of Battery Swapping Systems and how it is possible to get a fully charged battery in a time comparable to the one that takes to refuel a conventional ICE vehicle's tank.
For this reason it represents a revolutionary technology in the field of sustainable mobility, making it an attractive option for drivers interested in a quick and seamless energy replenishment.
Since we are dealing with a new innovative solution, there are also several challenges to be faced for a successful widespread adoption of Battery Swap.
One important challenge that will be discussed in a dedicated section is the choice of the battery cooling system. Air cooling is rarely adopted for vehicle's batteries, and liquid cooling is not that suitable for this application, since the coolant would start to leak when the battery has to be swapped. Possible solutions could be a cooling system integrated in the battery pack itself, or the usage of valves to close the cooling channels during the swap.
Other significant challenges are here presented.

2.3.1 BSSs Infrastructure Network and Logistics

As we have already said, the need of an adequate diffusion of BSS network on the territory is for sure the first aspect to be considered, since EV drivers range anxiety is mainly related to the scarcity of infrastructures, especially outside big city centers.

Investigations and predictive studies on the possible future battery swap demand must be performed for the different areas, guaranteeing a complete covering of the territory, to satisfy EV users needs. The location of the BSSs, has to be strategically defined to achieve a widespread market penetration of this technology, convincing customers to accept the BSS model over traditional charging methods.

Chen et al. [18], presented in their work a distinction between Diffused BSS in which both charging and swapping are performed, and an alternative solution defined Centralized BSS, in which the two processes occur in different locations. In this latter case the definition of an optimized distribution of the infrastructures is even more challenging and coordination between the different facilities is required.

2.3.2 High initial costs and economic feasibility

It's important to consider also the economic feasibility for the development of these new infrastructures: BSSs not only need more allocation space (which can be a problem in urban areas), but the associated construction costs are much higher than that of a conventional charging station.

Robotic systems, battery storage and all the other BSS components require significant investments, which are summed to the need of purchasing a number of batteries way larger than the number of battery swap vehicles, in order to fulfil customers demand and limit waiting times.

But as we have previously mentioned, battery pack is one of the most expensive components of EVs, and in this case it would be in charge of the BSS companies,

as well as all the maintenance costs. For this reason the number of initial batteries for a new BSS is another important decision in construction planning [19].
Furthermore charging a large number of batteries represents a challenge to the distribution grid since the charging module would consume high power locally. Optimized charging process management models have to be developed to use the charging power efficiently, balancing the load on the grid and reducing operational costs; for example varied/time-of-use electricity pricing can be exploited to encourage energy consumption during off-peak hours.

2.3.3 Interchangeability and Standardization

With swapping technology, battery models should converge into universal interchangeable standards, with similar shapes [20], in order to guarantee a totally automated swapping process at the BSS.
The standardization is not an easy task considering that each manufacturer has its own battery specifications to ensure competitive advantages and it's difficult for OEMs to share compatible battery architectures.
Battery packs should be designed for swapping purposes: as light as possible (to facilitate the swap), with a certain robustness in removing and reinstalling them from the vehicle since the process would be repeated many times during car's life. Ensuring a high reliability and safety standards while maintaining performance is not only technically challenging, but it also increases manufacturing costs[19].
However, a certain heterogeneity should be still considered to satisfy the different EV drivers demands, and different types of modular batteries can coexist.

2.3.4 Battery Ownership

If on one side not owning the battery could be beneficial for making the EV more affordable and cheaper, on the other side the shift to leasing or renting batteries

can be less appealing for many customers.
There are users who would predominantly use home and/or public charging, and BSS services only occasionally; for this reason they would be more interested in taking care of their own battery instead of having it swapped for one of unknown SOH and capacity [21].
Furthermore the lease could be charged on each swapping (lease-on-each-swap option), forcing many customers for a less usage of BSS if conventional charging stations are available.
To address this issue the Chinese brand NIO has proposed the alternative solution of Battery as a Service (BaaS), which consists in paying monthly rental fees independently from the number of swaps performed, like a sort of subscription (details in the dedicated section).

2.3.5 Battery Degradation

Lastly there is the problem of Battery Degradation that has to be managed. Batteries have to be stored between 25° and 40° with minimum temperature differences among the different packs, and maintaining a large inventory under these conditions can be expensive.
In the model proposed by Vallera et al.[20], the average residence time of batteries in swapping station would be of two days, with 75% of them being swapped within 24h.
Maximum battery range decreases over time and cycles of use, for this reason accurate SOC and SOH estimations are fundamental to ensure a safe operation and satisfying battery performances.
However customers would prefer receiving a new battery pack, rather than an older pack with lower energy storage, even if the latter one is still perfectly adapt for vehicle application, and this would drastically reduce the number of battery

operating cycles.
Nowadays once LIBs are discarded from EVs they still have 70-80% state of health which means that they can be recycled and brought to second life in different applications for which a very high SOH is not required [22].

2.4 Battery Cooling

As we have already mentioned, one of the main concerns when talking about battery swap is the definition of suitable cooling system, that can allow the replacement process.
An adequate battery thermal management system (BTMS) is needed to guarantee that battery is kept in the proper temperature range previously defined (20°-40°) during its operation.
During charging and discharging of the battery, a significant amount of heat is generated which has to be dissipated rapidly to the ambient atmosphere, not to reduce battery efficiency, power and energy capability.
Two principal sources of heat can be defined in LIBs [23]: reversible heat, generated by the electrochemical reactions occurring inside the battery, which can be positive or negative according to the charging or discharging process, and the irreversible heat, due to the current flowing in the battery and dissipated by Joule Effect, since a real battery has a certain internal resistance R_{int}. Further insights into this topic with the related equations will then be discussed in the next chapter.
If the temperature increases too much, the major safety issue is the risk of thermal runaway, which is a chain of internal exothermic chemical reactions that leads to a further temperature rise of the battery which can't be stopped, bringing the pack to irreparable damages, melting and battery burst. In the worst cases it can lead to the emissions of poisonous gases, and even fires and explosions. Thermal runaway risk starts around 80°/90° and becomes critical above 100° [24].

Cooling system is required also for guaranteeing temperature uniformity of the battery pack and the maximum temperature difference among the cells should be of 5°. But the heat produced at the positive electrode is around three times more than the one produced in the rest of the battery [25], and excessive local temperature heterogeneity and variance between among cells and with the coolant, can cause reduction of battery cycle life [26].

Cycle life is different from the calendar life even if both are used referred to battery life. The first one represents the number of complete cycles of charging and discharging the battery can perform before its capacity reaches 80% of the initial capacity and has to be discarded from EVs application. Calendar life instead is not a number of cycles but indicates the amount of time the batteries can be stored before reaching 80% of initial capacity.

Also low temperatures can be dangerous: if battery temperature goes below 0°, the transfer of ions through the electrolyte becomes much more complicated, leading to discharge capacity degradation and power delivery reduction. Additionally as we have mentioned before in the dedicated section, when the battery is charged at high C-rates and low temperatures, the phenomenon of lithium plating is very likely to occur.

For all these reasons, an appropriate cooling system is necessary for efficient performances, minimizing battery aging and degradation and ensuring safety.

Vehicle battery cooling systems for LIBs can be classified in air cooling, liquid cooling and phase change material (PCM) cooling, according to the different cooling medium.

2.4.1 Air cooling

Air cooling systems are generally adopted because of their low costs, high reliability, minimum maintenance and simple structure. Thanks to their lightweight, easy

integration due to their small size, and lack of coolant leakage, air cooled based BTMSs would be a suitable option for battery swap applications.
However this solution is generally adopted for applications with low heat dissipation requirements. Limiting the maximum battery temperature and keeping pack temperature uniformity, can be challenging with charge and discharge rates way larger than 2C [27], due to the low specific heat capacity and thermal conductivity of air.
Air cooling can be distinguished into natural cooling which exploits the natural airflow generated by the motion of the vehicle without the need of active components, and forced air cooling which is instead based on a cooling fan.
The effectiveness of natural cooling is strictly related to the ambient temperature, and with a hot climate performances are drastically reduced. Furthermore due to the limit cooling capacity of this solution, natural cooling can determine an uneven temperature distribution of the battery pack.
Forced air cooling instead provides consistent cooling performances less dependent on the external conditions. This is translated into a higher cooling efficiency, and an improved thermal uniformity that prevents localized overheating and uneven degradation of battery cells.
Air based BTMSs can be also classified into passive cooling systems and active cooling systems. In the first case less components are required since no external power sources are involved for battery cooling except for the cooling fan, and the air is the one coming from the outside, without performing any recirculation.
Despite lower costs and noise, and higher reliability, active air cooling is generally preferred for its higher cooling capacity.

With this second solution air recirculation is performed and an active evaporative AC/heater system is used to provide additional cooling or also heating of the pack. Going into more details, performances of air based BTMSs depend on several

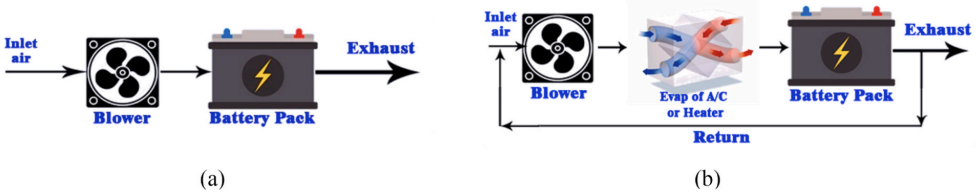

Figure 2.5: a)Passive Air cooling vs b)Active Air cooling [24]

factors: first of all an increase of the air flow rate generally leads to a decrease of the maximum temperature rise of the battery pack [28]. Also the path of the airflow and the heat transfer area are key factors to be considered. Mohammadian et al.[29] have demonstrated how the use of pin fins can guarantee a better temperature distribution of the battery pack by increasing the surface of contact between air and cells. For this reason the width of air ducts should be larger close to the highest temperature cells and smaller close to the lowest temperature cells [30].
Moreover cell arrangement has to be chosen accurately to maximize the BTMS performance. Fan et al. [27] have conducted a study on the energy efficiency of the air cooling system of a 4p8s module, considering three different module layouts: aligned, staggered and cross battery pack.

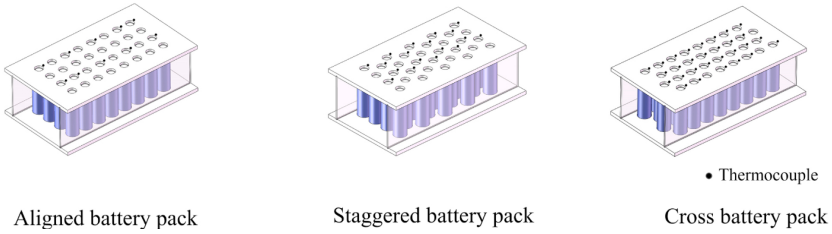

Figure 2.6: Possible module layouts [27]

According to their work, the aligned configuration presented the best cooling effectiveness for the same operating conditions, guaranteeing lower energy consumptions and higher heat dissipation.
Also the proper air inlet velocity is an important factor to be determined, in fact

higher air speed improves the performance of the cooling, but increases also the associated power consumptions.

2.4.2 Liquid cooling

Liquid cooling is a more efficient cooling method, already applied by Tesla and General Motors because of the high thermal conductivity and high specific heat capacity of the coolant [31].

It guarantees a better control over temperature rise and a better temperature uniformity because of liquid superior thermophysical properties compared to air.

Also liquid based BTMS can be classified into passive cooling and active cooling. In the first case the cooling is performed through a radiator as heat sink: the coolant absorbs heat from the battery cells while circulating in the cooling channels, and releases it to the ambient through the radiator.

As we have already seen for air cooling systems, even if passive solution is simpler, more reliable, cheaper and less power consuming, its cooling capacity is strictly depending on the temperature difference between ambient air and cells. For example during summer, this cooling strategy can become inefficient.

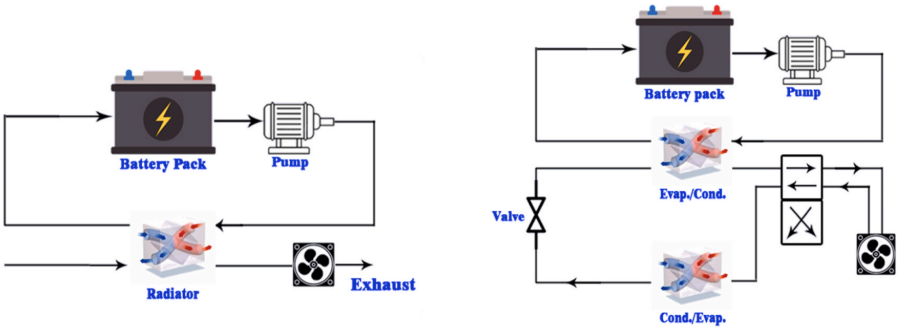

Figure 2.7: Active and Passive liquid cooling[24]

Active liquid based BTMSs instead are characterized by a primary loop, which corresponds to the passive cooling system, coupled with a secondary loop through

a heat exchanger that works as evaporator/condenser for keeping the liquid coolant in a proper temperature window.

This solution, even if more expensive and complex, is generally preferred because of the more accurate and precise battery temperature control that can be achieved with respect to passive liquid cooling, for discharging rates up to 4C [32].

Coolants used for this application can be of different nature: water and glycol mixtures are widely adopted, but also mineral oils, nanofluids and liquid metals [33].

Conventional Liquid based BTMSs are also defined as Indirect Liquid cooling systems since the liquid doesn't have a direct contact with battery cell surfaces but flows inside a cold plate. This solution leads to an increase of thermal resistance and a reduction of the heat transfer efficiency of the system, since the heat has to pass through the surface of the cooling channels inside the cold plate before being removed by the coolant.

An advanced cooling strategy which is gaining interest because of its cooling effectiveness also under extreme operating conditions, is direct liquid cooling (DLC).

DLC would reduce the thermal resistance between coolant and battery cells, enhancing heat dissipation efficiency thanks to the direct contact between the coolant and the battery modules; the absence of cooling plate guarantees a compact and low weight structure. In this case coolant compatibility is a key aspect to be considered: a high electrical resistance, and no chemical reactivity with the material of the cells are mandatory.

Coolants with low boiling temperature can also enable the benefit of two-phase cooling with much superior cooling efficiency than indirect liquid cooling [34]. The study conducted by Li et al. [35] has demonstrated how the transition of liquid SF33 from single phase to two phases determines a significant increase in heat

transfer coefficient, keeping battery temperature in a suitable range even with a discharge rate of 7C.
This solution is starting to be adopted for example in electric racing cars [36], but it's still not widespread, and won't be further analyzed in this work since due to the risk of coolant leakage and lack of standardization, is not a suitable option for battery swapping. Furthermore the need of robust sealings and the high costs of these specific coolants, make this option expensive and not suitable yet for mass production.

2.4.3 Phase Change Material cooling

Compared to the two previous BTMSs, this solution is less conventional. Dedicated studies would be required, but some insights on this type of technology can be interesting and needed to be cited as an existing alternative on the market, even if not yet so diffused.
Phase Change Material (PCM) cooling, is a passive Battery Thermal Management System that have gained attention in recent years for its energy efficiency. PCMs are materials capable of storing or releasing thermal energy by changing their phase, with minimum temperature rise.
When temperature increases above their phase transition threshold, PCM turns from solid to liquid: the endothermic fusion process absorbs thermal energy as latent heat, thereby cooling the battery and ensuring thermal uniformity within the pack. On the contrary when temperature decreases below the phase transition one, the PCM undergoes an exothermic transition from liquid to solid, releasing the previously stored thermal energy.
The benefits of this solution are not only the low power consumptions and better thermal homogeneity, but also its space efficiency and simplicity, since no fans or cooling plates are required.

Sabbah et al. [26] proposed in their study a comparison between the cooling effectiveness of active air cooling and PCM cooling, showing that PCM is capable of keeping battery temperature below 55° up to a discharge rate of 6.67C.

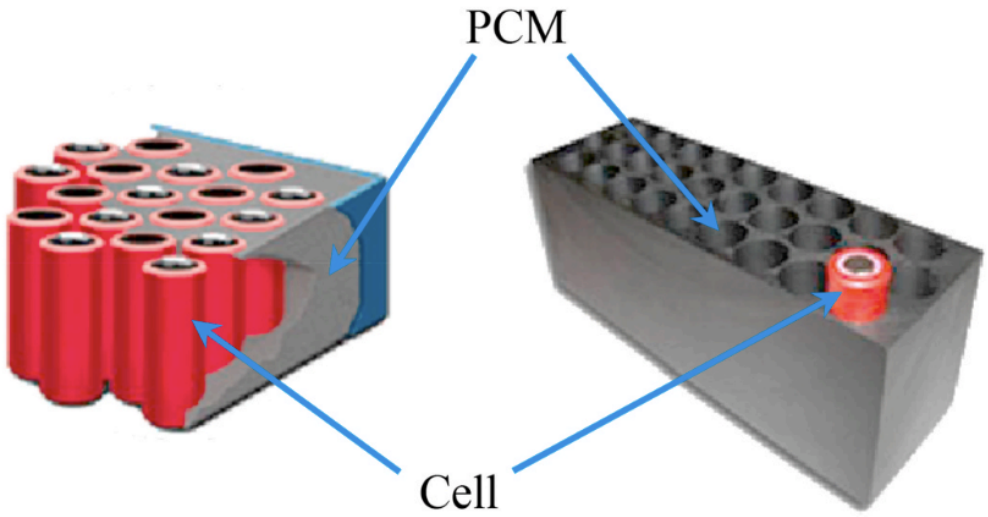

Figure 2.8: PCM Battery Thermal Management System [37]

However it's not easy to find a proper material suitable for this application, since several criteria are required [38]: first of all its phase transition temperature must be in the desired range in which the battery pack has to be kept, then a high latent heat and specific heat capacity are needed. Additionally PCM must be chemically stable, not flammable and with a very low thermal expansion, not to have problem of packaging during phase transitions.

PCMs can be divided into organic, inorganic and eutectic. One of the best options is represented by the solid state of paraffin, called paraffin wax [39] which is a non corrosive organic PCM characterized by a stable melting temperature. However thermal conductivity of paraffin is low and for this reason composite solutions would be preferable, adding metal foam, conductive particles or carbon materials [34][39].

Despite the cooling performances, low thermal conductivity is not the only disadvantage. The low reliability of this BTMS and the high costs of composite PCMs must be considered, as well as the risk of subcooling - when the PCM remains liquid below its melting point, degradating cooling performances - and the risk of leaks when PCM is in the liquid state.
Garud et al. [34] affirmed in their study that cooling performances and reduction of temperature rise with this solution can be improved by combining PCMs with cold plates and liquid cooling. This hybrid BTMS however is not practical for long-term commercial applications and due to its heavy weight it wouldn't be adapt for battery swap applications.
Summarizing, as we have said the definition of a suitable BTMS is fundamental for ensuring that the battery constantly operates in the optimal temperature range. Analyzing the battery thermal evolution when subjected to a current profile that simulates the conditions of a real driving scenario, if the temperature rise is sufficiently low, forced air cooling system can be adopted, otherwise liquid cooling has to be introduced. In case of battery swap applications, with liquid-based BTMS a solution has to be found to prevent the leakage of coolant at the interface sections of cooling channels when battery is removed. Two possible approaches could be implemented:

- Interface valves that would come into operation and close cooling channel sections during at the interface with the removable battery during the replacement process. This solution however would increase the complexity of the system and its integration on the existing 500e would be more challenging.

- Internal BTMS, that is swapped together with the battery, based on a cooling plate in contact with the base surface of battery cells. This method appears more effective and suitable for a swappable modular battery, thanks to its simplicity and effectiveness. For this reason this will be the solution considered

in the complete thermo-electrical cell model described in the fourth chapter.

2.5 Existing Realities

We can conclude this chapter by examining the main companies and corporations currently involved and active in the market within this technology field.
Better Place was an American-Israeli company, the first to implement battery swapping strategy as a solution for passenger EVs. It was founded in 2007, and started collaborating with the Israeli government for the creation of a proper BSS network for the development of this new technology.
Renault decided to take part in this ambitious program, providing 100,000 Fluence ZE, but the sales have resulted less than 1% of what was expected [40]. Due to this low market penetration and high initial investments, in May 2013 Better Place went bankrupt for business failure.
The company's failure can be attributed to multiple factors, extensively analyzed in numerous articles. According to Sovacool et al.[41], Better Place's financial difficulties were caused by technological immaturity: electric vehicles had limited range and battery designs not yet ready for extensive commercial deployment.
The number of electric vehicles was still too low, and the reduced battery swapping demand, together with the lack of substantial government support with subsidies, was not compatible with the constructive costs of Battery Swapping Stations.
Also Tesla in 2013, tried to develop battery swapping services, realizing the first BSS in California on the interstate between San Francisco and Los Angeles, but already in 2015 the project was abandoned.
In this case the failure was related firstly to the lack of customer density, which means that Tesla would have needed a large number of BSSs to guarantee easy access to the service to all the users, and secondly to the fact that most of US customers preferred charging the battery overnight exploiting the lower electricity

price, instead of swapping it.

Despite these firsts unsuccessful attempts, thanks to the evolution of EV technology, battery swap seems has nowadays the potential to develop and apply in some specific scenarios.

Below some of the most important players in this field are mentioned, before going into details with the world leader of battery swap, NIO.

The first example of an already existing battery swap system in Italy is the X-EV YOYO. The vehicle is embedded with a 3-modules battery of 10.4 kWh with an autonomy of 150km, positioned in the rear, which can be swapped in 3 minutes manually by a technical operator.

Focusing instead on automated swapping, a Chinese company gaining prominence in the battery swap industry is Geely, which aims to establish a common battery swap network in collaboration with NIO, to promote the standardization of this technology.

Also one of the world's largest manufacturer of electric vehicle batteries, CATL, has officially launched its battery swap service in China providing an alternative to recharging, and keeping the same costs of DC fast charging service [42].

Another important Chinese company that is focusing of large scale deployment of BSS network is BAIC. The aim is to promote this service not for private passenger cars but for ride-sharing EVs and electric taxis, which require rapid battery replacements to maintain a high number of daily rides.

BAIC BSS has an L shaped structure that covers around 67 square meters, it can store 28 batteries and potentially perform 216 swaps per day. These stations are realized starting from a container, in order to reduce costs and to make them easier to build in just 4 hours [43].

This thesis work has been realized because also Stellantis is actively engaged in the development and implementation of this new technology. In 2023 it has signed a

binding agreement with Californian startup Ample, to establish a partnership in EV battery swap.
The two partners have agreed to work toward integrating Ample's Modular Battery Swapping solution in Stellantis EVs [44].
The advantage of Ample's swappable battery architecture -as we can read from their website- is that "modules can accommodate any make, design, model or driving profile, without the need of carmakers to redesign their cars".

2.5.1 Battery as a Service, the case of NIO

The world leader in the field of battery swap is NIO, a Chinese brand established in November 2014, which realized in 2018 the first BSS in Nashan, Shenzhen with the aim of implementing this technology on its vehicles.
NIO has been the first company to introduce the idea of Battery as a Service, implementing the separation of vehicle and battery: the EV driver buys the vehicle but not the battery - which as mentioned previously is the most expensive component of EV - reducing significantly the costs and making the car more affordable to customers.
With this strategy, under a subscription plan buyers pay a fixed monthly fee of 152$ to lease the battery and can use free charging and swapping services [45].
Battery production is not directly performed by NIO, but in collaboration with CATL. However since the beginning of 2023, to reduce this dependency, NIO has started introducing new suppliers such as CALB and WeLion with the goal of realizing a new generation 150 kWh solid state battery with a range autonomy of more than 900 km [46].
Solid electrolytes are not commercially used yet, but they have several advantages [47]: i) Higher energy density, and so a lighter battery for the same capacity, which is beneficial for battery swap applications; ii)safety improvement, since there is no

risk of leakages and they are not flammable; iii)longer lifespan and less degradation, since there is no formation of dendrites on the surface of the cathode, which can determine the phenomenon of lithium plating; iv) faster charging, since they can tolerate higher currents and voltages; v) lower environmental impact, since WtT carbon emissions required for solid state batteries are approximately 40% of conventional Li-ion battery carbon emissions.

Figure 2.9: NIO Battery Swap Station

Differently from Better Place, the timing for the introduction of battery swap in this case has been much more favorable. EV population has increased drastically in recent years, and in China the majority of residents live in apartments without private parking spaces, necessitating reliance on public charging stations.
For this reason when NIO decided to realize its first BSS, battery swapping demand increased rapidly, also largely driven by the reduction in vehicle purchasing costs associated with BaaS strategy. This growth was also facilitated by substantial technological advancements and the maturity of the service provided by the Chinese company.
In October 2020 NIO completed the first 1 million swaps, then 2 millions in March 2021 that have been doubled to 4 millions swaps already by the end of September

of the same year [48]. Today NIO counts more than 2,400 BSSs, and is planning to expand to 3000 stations globally by the end of 2025.
According to their website, the new NIO's Power Swap Station 4.0, can provide 480 swaps per day, by completing the process in just 144 seconds thanks to a 640kW Liquid-Cooled Power Charger, boasting a maximum current of 765A and a voltage of 1,000V [49].

Chapter 3

Methodology

Having provided a comprehensive overview of the technological context, including the advantages of battery swapping and the challenges to be faced, the third chapter is now dedicated to the methodology conducted in this work of thesis. This section details the procedures and steps followed in the project, ensuring a thorough understanding of the approach and its outcomes.

As stated in the introduction, the goal of this thesis is to define a low-voltage, modular battery for the Fiat 500e, equipped with a cooling system suitable for battery swapping applications.

The work has been conducted in two major phases to achieve this objective.

First, battery capacity and range requirements specified for urban and extra-urban conditions are analyzed and a preliminary sizing of the battery is conducted, considering the suitable cells available on the market. The optimal cell in terms of performances, weight and costs is then identified. This process is further detailed in the preliminary battery sizing section.

The second phase consists in the development of a thermal model to accurately predict the thermal behavior of the cell under real driving current profiles. Validation of the model is then performed in the last chapter of this work.

Based on the observed temperature increases, it can be determined whether forced air cooling would be sufficient or if a liquid-based BTMS using a cooling plate is necessary. As it has been already said the preference in battery swap applications, would be for forced air cooling due to its lightweight and no risk of leakage during the swap process.

3.1 Preliminary Battery Sizing

As explained in the Introduction, low voltage systems (voltage lower than $60V_{\mathrm{dc}}$) with their lightweight and easier integration on the existing vehicle electronic setup with respect to class B systems, represent the best solution for the realization of a suitable battery for our application.
In particular we are considering a 52V modular battery system consisting in two separate modules that can be swapped independently based on the driver's specific mission requirements. The voltage of 52V has been selected as it represents the highest average voltage of the NMC battery pack for which the corresponding maximum voltage remains within the low voltage range, at 58.5V.
For this reason for each of the analyzed cells available on the market two different battery pack configurations have been defined:

- Frugal configuration, consisting in a single module if the mission is only urban without high requirements on battery capacity
- Dual configuration with a double module if instead the capacity requirement and required battery sizing are larger

This modular approach ensures that unnecessary components and weight are not carried when not required, optimizing efficiency and performance, and solving problems of standardization, since the two swappable modules are identical.
Detailed requirements of range and consumptions for frugal and dual configurations

are indicated in the tables below.
Battery sizing is expressed both in the form of energy (kWh) and in the form of capacity.

Declared Range		
WLTC-City Range	**200**	**km**
Consumption		
WLTC-City Consumption	**7.1**	**kWh/100km**
Battery Sizing		
WLTC-City Battery Size	**14.2**	**kWh**
WLTC-City Capacity Requirement	**274**	**Ah**

Table 3.1: Requirements and Constraints in Frugal configuration

This first table indicates the Requirements and Constraints for the Fiat 500e, based on the WLTC standards in case of urban mission, so the requirements that must be fulfilled by the frugal configuration.
The expected vehicle's range in urban environment is specified as 200km, with an energy consumption of about 7.1 kWh/100km.
From these two data is easy to calculate the total energy storage capacity in kWh, needed for the declared range under city driving conditions:

$$\textit{Battery size [kWh]} = \textit{Declared range [100km]} \times \textit{Consumption [kWh/100km]} \quad (3.1)$$

Capacity requirements in Ah instead represents the electrical charge storage and it indicates how much charge the battery has to deliver over a specific period.
The Ah rating depends on the nominal voltage (52V) of the battery pack:

$$\textit{Capacity Requirement [Ah]} = \frac{\textit{Battery size [kWh]}}{\textit{Nominal battery voltage [V]}} \quad (3.2)$$

The main drawback of low voltage batteries, as we can understand from the formula 3.2, is that to achieve the same energy and output power of B class systems, higher currents are required, which is translated into higher losses due to the battery internal resistance R_{int}.
For this reason in the following cell comparison section, investigations on the max C-rate which can be tolerated by each cell, will be performed.

Declared Range		
WLTC Range	**250**	**km**
Consumption		
WLTC Consumption	**11.0**	**kWh/100km**
Battery Sizing		
WLTC Battery Size	**27.5**	**kWh**
WLTC Capacity Requirement	**529**	**Ah**

Table 3.2: Requirements and Constraints in Dual configuration

Same considerations can be performed also in extra-urban conditions.
The declared range to be satisfied by the dual configuration is 250km instead of 200km, and the average consumptions are increased to 11.0 kWh/100km.
This increase is justified by the higher average speeds when driving on highways, and also the higher aerodynamic drag. Furthermore differently from urban scenarios, in this case it's not possible to exploit regenerative braking.
For these reasons the requirements on sizing and capacity are basically doubled for the dual configuration and the concept of a bi-modular battery pack emerges as the most effective and intelligent solution, as indicated in the scheme here represented.

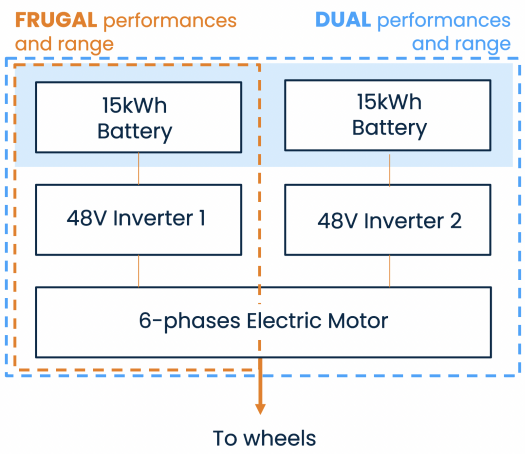

Figure 3.1: Scheme of frugal and dual configuration

Tables 3.1 and 3.2 represent the starting point to support discussions on battery sizing present in the following section, giving concrete data that have been provided. After delineating the requirements to be satisfied for both configurations, we can effectively start with the sizing, defining for each of the cells under consideration in this thesis, the corresponding battery packs.

All the data presented in this section are accessible via EVlithium[50] and Battery-design [51] websites.

The procedure employed is consistent across all cells, hence a detailed description of the equations used, will be provided only for the first cell considered. For the subsequent cells the focus will be directly on the sizing outcomes.

3.1.1 Frugal and Dual battery pack configurations

The primary objective of this sizing process is to identify the optimal solution in terms of weight and cost.

A lightweight battery pack is essential for battery swap applications for several technical reasons. The ease of handling, is fundamental in case of manual battery swapping, reducing the risk of injury of the operator, but it's important also if the

process is automated: thanks to the lower mechanical and structural demand on the robotic arm, its performance and durability can be enhanced.
Lighter battery packs can also improve benefits and efficiency of battery swap technology, since they can be exchanged more rapidly, thereby accelerating the swapping process and minimizing congestion at Battery Swap Stations.
Additionally, reducing the battery weight is beneficial for the overall infrastructure: lighter batteries can be transported and stored more easily, requiring less structural support at the BSS and lower construction and maintenance costs.

Cell Nominal Voltage	**3.65**	**V**
Cell Nominal Capacity	**63**	**Ah**
Cell Specific Energy Density	**172**	**Wh/kg**
Cell Weight	**1.337**	**kg**

Table 3.3: Fiat 500e Samsung SDI battery cell characteristics [51]

We can start our analysis considering the actual Samsung SDI cell of FIAT 500e battery pack, whose characteristics are indicated in table 3.3.
Cell Nominal Capacity is a fundamental design parameter for the sizing of the battery, influencing the series and parallel arrangements in the two configurations, to achieve the desired specifications for voltage and energy storage of the battery pack.
When cells are connected in series, the total voltage is the sum of each voltage, while the capacity is the same of the single cell. If instead cells are connected in parallel the total capacity is the sum of each capacity, and the voltage is the same of the single cell.
The arrangement of cells in the frugal configuration can now be calculated

$$N^{\circ}\ of\ series = \frac{Nominal\ Voltage\ [V]}{Cell\ nominal\ voltage[V]} \tag{3.3}$$

where the nominal voltage is the 52V of the battery pack.

$$N^{\circ}\ of\ parallels = \frac{Capacity\ requirement[Ah]}{Cell\ nominal\ capacity[Ah]} \tag{3.4}$$

where capacity requirement is specified in table 3.1.
The total number of cells can be easily computed:

$$N^{\circ}\ of\ cells = N^{\circ}\ of\ series \times N^{\circ}\ of\ parallels \tag{3.5}$$

Once we have the number of cells, the nominal ampere hours capacity in Ah of the battery pack is:

$$Nominal\ Ampere\ hours\ [Ah] = Cell\ nominal\ capacity\ [Ah] \times Number\ of\ parallels \tag{3.6}$$

We can determine the energy capacity of each cell is calculated by multiplying the cell's nominal voltage by its nominal capacity.

$$Energy\ capacity\ cell\ [Wh] = Cell\ voltage\ [V] \times Cell\ capacity\ [Ah] \tag{3.7}$$

The energy capacity of the battery pack, will be the sum of the energy capacities of the individual cells.

$$Energy\ capacity\ battery\ [kWh] = Energy\ capacity\ cell\ [Wh] \times N^{\circ}\ of\ cells \tag{3.8}$$

Nominal capacity [kWh] is the design parameter of the battery which must satisfy the requirement expressed in table 3.1. In our analysis a further step has

been the definition of a usable capacity, which is generally lower than the nominal one specified on the datasheets. Usable capacity has been considered as 90% of the nominal one, so we have just introduced a safety factor of 0.9.

$$Usable\ energy\ capacity\ battery\ [kWh] = Energy\ capacity\ battery\ [kWh] \times 0.9 \quad (3.9)$$

This correction is needed to ensure that the battery pack defined is actual capable of meeting the requirements.
With this first cell analyzed we can observe from table 3.4 and 3.5that the usable capacities are 14.5 kWh and 29.0 kWh respectively in frugal and in dual configurations, indicating that they are above the energy demands (14.2 kWh and 27.5 kWh tables 3.1 and 3.2).
The mass of the single cell is obtained from the data in table 3.3:

$$Cell\ mass\ [kg] = Mass\ cell\ [kg] \times N°\ of\ cells \quad (3.10)$$

The mass of the cells has been computed multiplying the mass of the single cell of the FIAT 500e reported on the datasheet [51], by the number of the cells.

$$Total\ cells\ mass\ [kg] = Mass\ cell\ [kg] \times N°\ of\ cells \quad (3.11)$$

But battery mass exceeds this weight, since in equation3.10, only cells have been considered. Battery pack instead comprehends also a BMS, a thermal management system, a protective metallic housing with reinforcements, electronic cables and busbars. Each of these components have a non negligible weight to be considered. For sake of simplicity, knowing that the battery cells represent the major contribute on the overall weight, cells mass has been considered as 85% of the total battery mass.

$$Battery\ mass\ [kg] = Total\ cells\ mass\ [kg] + 0.15\ Total\ cells\ mass\ [kg] \quad (3.12)$$

Battery Pack Specific energy density will be the ratio between the nominal capacity computed in equation 3.8, and the battery mass calculated in equation 3.11.

$$Battery\ specific\ energy\ density\ [Wh/kg] = \frac{Energy\ capacity\ battery\ [kWh]}{Battery\ mass\ [kg]} \quad (3.13)$$

Numerical results are displayed in table 3.4.

Nominal Capacity	**16.1**	**kWh**
Useable Capacity	**14.5**	**kWh**
Is Useable Capacity > WLTC-city requirement	**YES**	
Cell Specific Energy Density	**172**	**Wh/kg**
Number of Series	**14**	-
Number of Parallels	**5**	-
Number of Cells	**70**	-
Cathode Material	**NMC622**	-
Nominal Voltage	**52**	**V**
Nominal Ampere-Hours	**315**	**Ah**
Battery Mass	**110.10**	**kg**
Battery pack Specific Energy Density	**146.20**	**Wh/kg**

Table 3.4: Frugal configuration 500e battery cells

As we have already mentioned, battery pack in dual configurations consists in two modules each of them corresponding to the frugal configuration, which can be swapped independently.
For this reason for the number of series, the same value obtained in frugal configuration has been kept since the nominal voltage is still 52 V. For the number of parallels, instead of considering the capacity requirement in table3.2 (529 Ah), we have just doubled the number of parallels found in frugal configuration since as we said, the two modules have to be identical.
The requirements in this case are indicated in table 3.2. The rest of the calculations are the same and are displayed in table 3.5.
The battery mass will be of course the double of the one of the frugal, while the battery pack specific energy density is kept the same.

Nominal Capacity	**32.2**	**kWh**
Useable Capacity	**29.0**	**kWh**
Is Useable Capacity > WLTC requirement	**YES**	
Cell Specific Energy Density	**172**	**Wh/kg**
Number of Series	**14**	-
Number of Parallels	**10**	-
Number of Cells	**140**	-
Cathode Material	**NMC622**	-
Nominal Voltage	**52**	**V**
Nominal Ampere-Hours	**630**	**Ah**
Battery Mass	**220.20**	**kg**
Battery pack Specific Energy Density	**146.20**	**Wh/kg**

Table 3.5: Dual configuration 500e battery cells

The battery mass will be of course the double of the one of the frugal, while the battery pack specific energy density is kept the same.

3.1.2 Comparative Analysis and Cost Evaluation

Same calculations have been performed on other cells and for each of them, dual and frugal configurations of the corresponding battery packs are reported in Appendix A, as well as the corresponding battery masses. The analysis is carried out not only with cells from existing EVs' batteries [51], and the configurations obtained are summarized in table 3.6.

Cell	**Cell type**	**Configuration frugal**	**Configuration dual**
Fiat 500e	Prismatic	14s5p	14s10p
Bmw i3 2016	Prismatic	14s3p	14s6p
Bmw i3 2018	Prismatic	14s3p	14s6p
Kia Niro	Pouch	14s5p	14s10p
Volkswagen ID 3	Pouch	14s4p	14s8p
CALB L300F177A	Prismatic	16s2p	16s4p
CALB L7914897	Prismatic	14s2p	14s4p
CALB L221N113A	Prismatic	14s3p	14s6p
CALB L173F280A	Prismatic	15s1p	15s2p
CALB L221N147A	Prismatic	14s2p	14s4p
EVE D21	Pouch	14s6p	14s12p
Lexus UX 300e	Prismatic	14s6p	14s12p

Table 3.6: Recap of frugal and dual battery configurations from Appendix A

These calculations have been performed considering the battery pack's nominal capacity but as we defined in equation 3.9 the usable capacity is instead 10% lower. As we can see from Appendix A, not for all cells with the configurations defined,

the requirements of tables 3.1 and 3.2 are met also by this usable capacity (BMW i3 2016, Kia Niro, CALB L173F280A). Consequently, these three solutions have been excluded to ensure adequate capacity margins with respect to the requirements.
It's also possible to note that not all the cells are prismatic. The main advantage of pouch cells is their lower weight per energy storage but the development of a BMS is much more complicated [52].
The aim of thesis work is to define a battery pack that can be easily integrated on the existing Fiat 500e. For this reason prismatic cells are preferred in this application: since the actual 500's battery cells are prismatic, switching to pouch cell would require a complete redesign of the pack and of the BMS, significantly increasing the costs.

Cell	**Battery mass frugal**	**Battery mass dual**	**Energy density**
Fiat 500e	110.10 kg	220.20 kg	146.20 Wh/kg
Bmw i3 2016	97.67 kg	195.34 kg	148.75 Wh/kg
Bmw i3 2018	108.21 kg	216.42 kg	170.00 Wh/kg
Kia Niro	73.96 kg	147.93 kg	206.13 Wh/kg
Volkswagen ID 3	116.14 kg	232.28 kg	137.28 Wh/kg
CALB L300F177A	118.50 kg	237.00 kg	153.00 Wh/kg
CALB L7914897	87.14 kg	174.30 kg	181.90 Wh/kg
CALB L221N113A	88.94 kg	177.88 kg	198.31 Wh/kg
CALB L173F280A	95.63 kg	191.25 kg	160.30 Wh/kg
CALB L221N147A	77.09 kg	154.18 kg	204.90 Wh/kg
EVE D21	73.15 kg	146.30 kg	216.75 Wh/kg
Lexus UX 300e	87.55 kg	175.10 kg	181.04 Wh/kg

Table 3.7: Recap of frugal and dual battery masses and specific energy density from Appendix A

From table 3.7 it's clear that the best solutions for battery weight reduction are the cells with higher battery specific energy densities. In particular the pouch cells of Kia Niro and EVE D21, and the prismatic cell CALB L221N147A seem the most promising alternatives. For this reason we focused the attention to costs and C-rates in charging and discharging only of these three cells in table 3.8. In particular with the last option is possible to obtain a 30% lighter battery with respect to the weight of the pack that would be required with the actual cells of Fiat 500e.

Cell	**C-rate discharge**	**C-rate charge**	**Cells price**
Kia Niro	2.34C	1.202C	4900€
CALB L221N147A	4.63C	3.51C	2464€
EVE D21	0.33C	0.33C	3444€

Table 3.8: C-rates and cost evaluations of the best cells identified

We have already mentioned that one of the drawbacks of having a low voltage battery pack is that higher currents (which lead to higher losses) are required to obtain the same output power.
Increasing the charge or discharge rate in fact, leads to an increase of the cell temperature, proportional to its internal resistance. For this reason it's important that the cell chosen for our battery swap application can withstand large C-rates both in charge and in discharge, not to damage the pack with demanding current profiles.
From table 3.8 we can immediately discard cell EVE D21: even if the corresponding battery pack is the lightest among the cells analyzed, the C-rates are way too low to be a suitable solution for our application. Furthermore as we said, prismatic cells are preferred over pouch ones for the easiness of integration.
Also Kia Niro cells are discarded, but not only for being pouch cells, and having

lower C-rates than the CALB, but also because as we mentioned previously, with these configurations their usable capacity is not capable of satisfying the requirements.
Even if it's not the primary goal of this work, also cells costs must be taken into account. As previously affirmed, with the solution proposed by NIO (BaaS) the battery is in charge of the OEM, not of the driver. For this reason to ensure the economic feasibility of this solution, minimize the costs of each battery is another key aspect. Also in this case CALB L221N147A represents the best choice, with a price much more competitive than EVE D21 and basically half of Kia Niro cells price.

Summarizing, the first objective of the thesis was the definition of the optimal cell for our battery swap application.
According to our analysis we can affirm that cell CALB L221N147A is the best solution for several characteristics:

- Very high nominal capacity and energy density: less cells in parallel are required and as consequence, the corresponding battery pack is much lighter than other possible solutions.
- Usable Capacity larger than requirements: differently for the Kia Niro solution, in this case there is a certain capacity margin that enables to satisfy requirements even considering the usable capacity.
- Prismatic cell: having a prismatic cell is better not to redesign completely the Fiat battery pack and its BMS.
- High max C-rates both in charging and discharging: having a high C-rate both in charge and in discharge is a fundamental requirement in our application, since for low voltage batteries, to get the same output electrical power, higher currents are required.

- Lower price: Having a lower price with respect to the other solutions is essential for ensuring the economic feasibility of the project, considering the large number of batteries that would have to be stored in the BSS.

3.1.3 Geometrical Constraints

Once the cell with the best performance for our study case has been defined, it's necessary to verify if the corresponding battery pack with the configuration obtained, would satisfy the geometrical requirements.
As we have previously said we are looking for a battery pack that could be easily integrated on the fiat 500e chassis without the need of redesigns; for this reason geometrical constraints must be taken into account.
The proposed solution battery with CALB L221N147A cells, must fit in the actual battery housing, used for the Samsung SDI battery cells of the 500e.
The available space for the battery modules is a rectangular battery housing with an additional front end extremity as illustrated in figure 3.2. Our primary focus is on the geometric requirements for width and length to optimize the utilization of available space on the chassis.

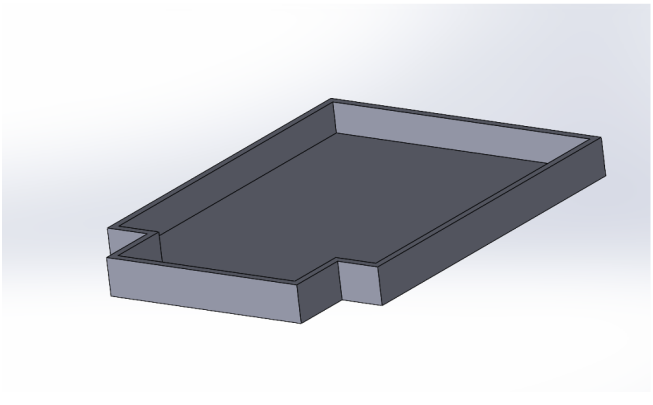

Figure 3.2: Battery housing of 500e

Due to confidentiality constraints, the CAD of the battery pack of the 500e can't be reported, neither its dimensions. Therefore, a schematic representation of the housing and of the modules has been provided to give an idea of the packaging. The goal is to validate our analysis, demonstrating that the proposed solution fully complies with the geometric constraints.
The scheme of the actual packaging of the Samsung SDI battery inside the housing (look at appendix B for the real pictures in bottom and top view) is reported in figure 3.3 with the modules indicated in red. As we can note the extremity of the housing is exploited by an additional module of the battery, while a large space is left behind for the BMS.

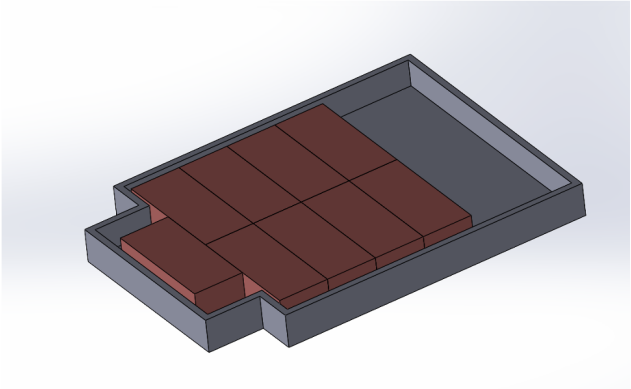

Figure 3.3: Samsung SDI actual packaging

The proposed alternative solution with CALB L221N147A instead consists in a battery pack with 14s4p configuration (14s2p in frugal).
Considering the dimensions of the cell reported in the table 3.9 the final dimensions of the battery pack in the dual configuration would be:

- Total width of the pack: thickness of the cell multiplied by the number of cells in series (14 cells) = **616 mm**
- Total length of the pack: width of the cell multiplied by the number of cells

in series (4 cells) = **880 mm**

- Total height of the pack: height of the cell = **105 mm**

Cell Width	220	mm
Cell Thickness	44	mm
Cell Height	105	mm

Table 3.9: CALB L221N147A dimensions [50]

The proposed packaging that would be obtained is represented in the figure below (3.4). As we can note the total width and length of the pack wouldn't be an issue, since it fits in the housing. The major problem is that no space available behind the battery pack would be left for the BMS.
However this issue can be solved, because not the whole width of the space behind the Samsung SDI pack of figure3.3 is occupied by the BMS, which instead has a width smaller than the one of the housing front end extremity. For this reason with a rearrangement of the components, the battery management system could be placed in this available space which wouldn't be occupied anymore by a battery module as it was done in the Samsung SDI battery.

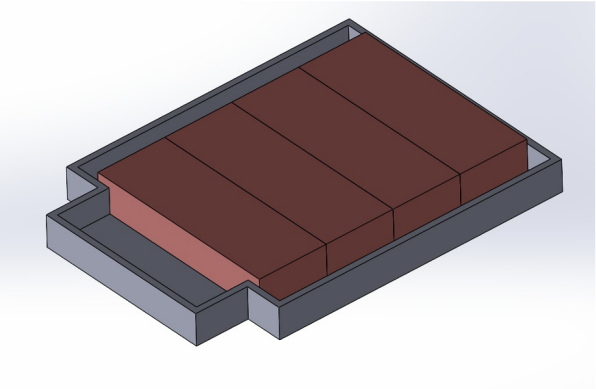

Figure 3.4: CALB proposed packaging

In conclusion, the CALB L221N147A proposed as an alternative to the Samsung SDI not only represents the optimal solution among the cells examined, but also guarantees that the resulting battery pack, in both frugal and dual configurations, meets the geometric requirements.

3.2 Thermal model

Once the optimal cell is defined, the focus can shift to the second objective of this thesis: developing a thermal model of the cell to predict temperature rise and trends under different current profiles.
The definition of an effective Battery Thermal Management System (BTMS) is critical for ensuring safety, durability of the pack, and maintaining the battery within the appropriate temperature range, thereby minimizing temperature differences and reducing degradation.
This thermal model will be experimentally validated in Chapter 4.
Based on the resulting data, which analyzes the cell's temperature behavior under given current profiles, the appropriate cooling method can be determined. If the temperature increase is minimal and controlled, air cooling may be sufficient, if instead higher cooling performance is required to maintain optimal cell temperature, a more effective liquid-based cooling system will be necessary.

3.2.1 Theoretical Background

Before starting with the definition of the model, a theoretical background of the equations involved is needed.
Considering our battery cell as a closed system, we can affirm that the thermal power absorbed $\dot{Q}$ is defined as the difference between the thermal power generated

$\dot{Q}_{\text{in}}$ inside the system and the thermal power dissipated $\dot{Q}_{\text{out}}$.
This difference is proportional to the mass of the cell m, its specific heat capacity at constant pressure c_{p}, and the rate of change of cell's temperature [53]:

$$\dot{Q}_{\text{in}} - \dot{Q}_{\text{out}} = mc_{\text{cell}}\frac{dT_{cell}}{dt} \tag{3.14}$$

The thermal power generated inside the cell $\dot{Q}_{\text{in}}$ can be defined as the sum of two effects: the Joule heating $\dot{Q}_{\text{joule}}$ and the entropy change $\dot{Q}_{\text{entropy}}$ [54]:

$$\dot{Q}_{\text{in}} = \dot{Q}_{\text{joule}} + \dot{Q}_{\text{entropy}} \tag{3.15}$$

The first contribution is also referred as irreversible effect since it's always a positive ohmic contribution to the thermal power dissipated. It can be defined as the difference between the actual voltage of the cell V and the open circuit voltage V_{ocv} multiplied by the current [55].

$$\dot{Q}_{\text{joule}} = i(t)(V - V_{\text{ocv}}) \tag{3.16}$$

The difference of voltages represents the voltage drop due to internal resistance when current flows through the cell. For this reason equation it can be also written as:

$$V - V_{\text{ocv}} = R_{\text{int}}i(t) \tag{3.17}$$

Substituting equation 3.17 in equation 3.16 we get the final form of the joule contribution to $\dot{Q}_{\text{in}}$:

$$\dot{Q}_{\text{joule}} = R_{\text{int}}i(t)^2 \tag{3.18}$$

The second contribution in equation 3.15 instead refers to the heat generated or

absorbed due to changes in entropy during the electrochemical reactions within the battery. It's also indicated as reversible effect because theoretically if the reactions are reversed, the heat released can be absorbed

$$\dot{Q}_{\text{entropy}} = -i(t)T_{\text{cell}}(t)\frac{\Delta S}{nF} \tag{3.19}$$

ΔS indicates the change of entropy of the system, n is the number of electrons involved in the chemical reaction (n=1) and F is the Faraday's number.
The current flowing in the cell is positive in discharge ($\dot{Q}_{\text{entropy}}$ becomes a negative contribution to $\dot{Q}_{\text{in}}$) and negative in charge.
Entropy change can be also written as a function of the change rate of V_{ocv} with temperature gradient [54]:

$$\frac{\Delta S}{nF} = \frac{dV_{\text{ocv}}}{dT} \tag{3.20}$$

The full form of equation 3.15 can be now written:

$$\dot{Q}_{\text{in}} = R_{\text{int}}i(t)^2 - i(t)T_{\text{cell}}(t)\frac{dV_{\text{ocv}}}{dT} \tag{3.21}$$

As affirmed by Akbarzadeh et al. [56], several studies have demonstrated that neglecting the entropic heat generation is reasonable, especially for high current applications, as it is small compared to the the ohmic heat generation. Hence the total thermal power generated in the cell will be indicated only with its irreversible contribution $\dot{Q}_{\text{joule}}$ as in equation 3.18.
Focusing instead to the thermal power dissipated $\dot{Q}_{\text{out}}$, heat exchange can occur in three possible ways:

- Conduction: when the heat transfer is related to the direct contact of solid materials at different temperatures

- Convection: when heat transfer occurs through the contact with a fluid (liquid or gas) in motion, due to the temperature gradient
- Radiation: when heat is exchanged through electromagnetic waves, without the need of a medium

In the thermal models, the contribution of radiation to the overall heat exchange of the battery cell will be neglected, as it is negligible compared to the heat exchange with air through convection and with the cold plate through conduction.
In the thermal model, the battery cell is assumed to have a uniform temperature, meaning that the core and surface temperatures are considered equal, and the current flow within the cell is uniformly distributed [57].
Similarly, the cold plate is modeled with a uniform temperature, neglecting any temperature gradients between the coolant and the cold plate material.
After having specified these assumptions, it's possible to proceed with the definition of the dissipated thermal power $\dot{Q}_{\text{out}}$.

$$\dot{Q}_{\text{out}} = \dot{Q}_{\text{conv}} + \dot{Q}_{\text{cond}} \tag{3.22}$$

where $\dot{Q}_{\text{conv}}$ is the thermal power dissipated by covection with the air surrounding the cell, while $\dot{Q}_{\text{cond}}$ is the thermal power dissipated by conduction with the cold plate in contact with the base of the cell. Details on the geometry of the model will be provided in the following sections.
$\dot{Q}_{\text{conv}}$ is proportional to the temperature difference between the cell and the air [58][59]:

$$\dot{Q}_{\text{conv}} = hA_{\text{air}}(T_{\text{cell}}(t) - T_{\text{air}}) \tag{3.23}$$

A_{air} is the surface of contact between cell and air where heat transfer occurs and h is the heat transfer coefficient between air and cell. It represents the rate of

heat transfer per unit area per unit temperature difference: the higher the heat transfer coefficient is, the lower the temperature rise will be [60].
$\dot{Q}_{\text{cond}}$ instead can be defined through the Fourier's law and it is proportional to the temperature difference between the cell and the cold plate [58]:

$$\dot{Q}_{\text{cond}} = \frac{k_{\text{cp}} A_{\text{cond}}}{s_{\text{cp}}} (T_{\text{cell}}(t) - T_{\text{cp}}) \tag{3.24}$$

k_{cp} is the thermal conductivity of the cold plate and it's an indication of material's ability to conduct heat. A_{cond} is the surface of contact between cell and cold plate (in our case the base surface of the cell) and s_{cp} is the thickness of the cold plate. Equation 3.14 can be now written in its complete form, considering the conduction and convection contribution, and neglecting the entropic term for $\dot{Q}_{\text{in}}$:

$$mc_{\text{cell}} \frac{dT_{cell}}{dt} = R_{\text{int}} i(t)^2 - \frac{k_{\text{cp}} A_{\text{cond}}}{s_{\text{cp}}} (T_{\text{cell}}(t) - T_{\text{cp}}) - hA_{\text{air}} (T_{\text{cell}}(t) - T_{\text{air}}) \tag{3.25}$$

3.2.2 Thermal model only with convection

For the definition of a comprehensive and realistic thermal model of the battery cell a bottom-up approach has been adopted, starting from the simplest ideal case of the battery cell entirely surrounded by air with heat exchanged only by convection, as schematized in figure 3.5.

Equation 3.25 in this case can be simplified:

$$mc_{\text{cell}} \frac{dT_{cell}}{dt} = R_{\text{int}} i(t)^2 - hA_{\text{air}} (T_{\text{cell}}(t) - T_{\text{air}}) \tag{3.26}$$

In this case A_{air} is the sum of all lateral surfaces and top and bottom surfaces of the prismatic cell, since no cold plate is considered.
The product of the mass m and the specific heat capacity c_{cell} can be also written

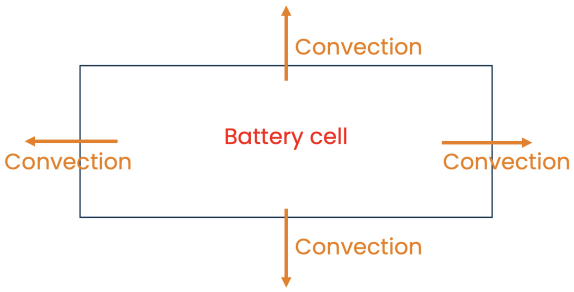

Figure 3.5: Schematization of convection heat transfers

as:

$$mc_{\text{cell}} = C_{\text{cell}} \tag{3.27}$$

where C_{cell} is the overall cell heat capacity and indicates the amount of heat required to raise the temperature of a given mass by one degree Celsius.
It's possible to define an analogy between thermal systems and electrical circuits, based on the similarity between the equations governing heat flow and electrical current flow.
As affirmed by Ramirez-Laboreo et al. [61] this similarity is sustained with two pairs of thermal and electrical equations. Equation 3.14 in fact can be correlated to the charge of a capacitor:

$$I = C\frac{dV}{dt} \tag{3.28}$$

where C is the capacitance and I is the current needed to charge it.
Equation 3.23 instead can be correlated with the Ohm's law:

$$I = \frac{\Delta V}{R} \tag{3.29}$$

where ΔV is the voltage difference across the material.

This law establishes that current flow between two points is driven by their difference of voltage and the constant of proportionality that relates the two quantities is the electrical resistance R. Similarly in thermal systems, both in case of conduction and convection the heat flow is driven by a temperature difference.
Therefore ΔT in thermal systems can be defined as the analogous to the voltage difference in electrical circuits, while the resulting heat flow $\dot{Q}$, corresponds to the current I.
For this reason it's possible to determine an equivalent thermal resistance, defined as the ratio of the temperature difference ΔT and the resulting heat flow $\dot{Q}$.
Both electrical and thermal resistance depend on the properties of the material and measure how much it opposes the flow respectively of electrical current or heat through it.
Since in this first model we are just considering convection with air, $\dot{Q}$ is equal to $\dot{Q}_{\text{conv}}$ and making reference to equation 3.23, convection thermal resistance R_{conv} will be:

$$R_{\text{conv}} = \frac{1}{hA_{air}} \tag{3.30}$$

Subtituting equations 3.27 and 3.30 in equation 3.26 we obtain:

$$\frac{dT_{\text{cell}}}{dt} = \frac{R_{\text{int}} i(t)^2}{C_{cell}} - \frac{(T_{\text{cell}}(t) - T_{\text{air}})}{R_{\text{conv}} C_{cell}} \tag{3.31}$$

Which can be rewritten isolating the terms related to T_{cell}:

$$\frac{dT_{\text{cell}}}{dt} + \frac{T_{\text{cell}}(t)}{R_{\text{conv}} C_{cell}} = \frac{R_{\text{int}} i(t)^2}{C_{cell}} + \frac{T_{\text{air}}}{R_{\text{conv}} C_{cell}} \tag{3.32}$$

This is a first-order linear ordinary differential equation (ODE), because the highest derivative of $T_{\text{cell}}(t)$ is the first derivative with respect to t, $T_{\text{cell}}(t)$ and $\frac{dT_{cell}}{dt}$ appear to the first power and are not multiplied together, and the equation

involves only t as independent variable.

In the context of this thesis, it is fundamental to highlight an additional assumption: we are considering sufficiently small time intervals during which the current can be approximated as constant. This simplification facilitates the resolution of the differential equation.

The generic form of first-order ODE is:

$$y' + p(t)y = q(t) \tag{3.33}$$

and the corresponding solution will be in the form:

$$y(t) = e^{-P(t)} \left[c_1 + \int q(t) \cdot e^{P(t)}\, dt \right] \tag{3.34}$$

Where c_1 is a constant of integration and $P(t)$ is defined as:

$$P(t) = \int p(t)dt \tag{3.35}$$

In our study case:

$$y = T_{\text{cell}}(t) \tag{3.36}$$

$$p(t) = \frac{1}{R_{\text{conv}} C_{cell}} \tag{3.37}$$

$$P(t) = \int p(t)dt = \frac{t}{R_{\text{conv}} C_{cell}} \tag{3.38}$$

$$q(t) = \frac{R_{\text{int}} i(t)^2}{C_{cell}} + \frac{T_{\text{air}}}{R_{\text{conv}} C_{cell}} \tag{3.39}$$

For this reason the solution of the differential equuation 3.32 will be:

$$T_{cell}(t) = e^{-\frac{t}{R_{conv} C_{cell}}} \left(c_1 + \int \left(\frac{R_{int} i(t)^2}{C_{cell}} + \frac{T_{cp}}{R_{conv} C_{cell}} \right) e^{\frac{t}{R_{conv} C_{cell}}}\, dt \right) \tag{3.40}$$

The constant of integration c_1 has to be determined by imposing the condition that the temperature at the first instant has to be equal to the initial temperature of the cell T_0

$$T(0) = T_0 \tag{3.41}$$

By setting equations 3.40 and 3.41 as a system we get:

$$c_1 = T_0 - R_{conv} \cdot R_{int} \cdot i(t)^2 - T_{air} \tag{3.42}$$

substituting equation 3.42 in equation 3.40, the solution of differential equation 3.32 is finally derived:

$$T_{cell}(t) = R_{conv} \cdot R_{int} \cdot i(t)^2 (1 - e^{-\frac{t}{R_{conv} C_{cell}}}) + (T_0 - T_{air}) e^{-\frac{t}{R_{conv} C_{cell}}} + T_{air} \tag{3.43}$$

Similarly to electrical circuits also in this case the product $R_{conv}C_{cell}$ in the exponent's denominator is the time constant τ_{th} which defines the transient behaviour of the thermal system. Specifically, it represents the rate at which the system responds to temperature changes, indicating the time required to reach the final stable temperature after a step change in the electrical power input.

$$T_{cell}(t) = R_{conv} \cdot R_{int} \cdot i(t)^2 (1 - e^{-\frac{t}{\tau_{th}}}) + (T_0 - T_{air}) e^{-\frac{t}{\tau_{th}}} + T_{air} \tag{3.44}$$

Alternatively differential equation 3.31 can be analytically solved using the Euler discretization method, which consists in the definition of a sufficiently small time constant τ such that the following approximation is valid:

$$\frac{dT_{cell}}{dt} = \frac{T_{cell}(i) - T_{cell}(i-1)}{\tau} \tag{3.45}$$

where $T_{cell}(i) - T_{cell}(i-1)$ represents the cell temperature difference in two consecutive instants. As convention we have considered:

$$T_{cell}(t) = T_{cell}(i-1) \tag{3.46}$$

Adopting this method, the differential equation can be transformed into an approximated algebraic equation:

$$\frac{T_{cell}(i) - T_{cell}(i-1)}{\tau} = \frac{R_{\text{int}} i(t)^2}{C_{cell}} - \frac{(T_{\text{cell}}(i-1) - T_{\text{air}})}{R_{\text{conv}} C_{cell}} \tag{3.47}$$

Rearranging the terms and isolating $T_{cell}(i)$, we get the discretized solution of the equation:

$$T_{cell}(i) = \tau \cdot \frac{R_{\text{int}} i(t)^2}{C_{cell}} + \left(1 - \tau \frac{1}{R_{conv} C_{cell}}\right) \cdot T_{cell}(i-1) + \tau \cdot \frac{1}{R_{conv} C_{cell}} \cdot T_{air} \tag{3.48}$$

This is the resolution approach that is adopted by Simulink to solve differential equations.

3.2.3 Thermal model with constant temperature cold plate

A cold plate in contact with the bottom surface of the cell is now introduced in the model, and also conduction heat exchange is considered.

In this case the temperature of the cold plate is simplified as a constant, which means that the cold plate is assumed to have ideally an infinite heat capacity and keeps the same T_{cp} even if heat exchange with the cell is occurring.

Since both conduction and convection are occurring, the thermal evolution of the

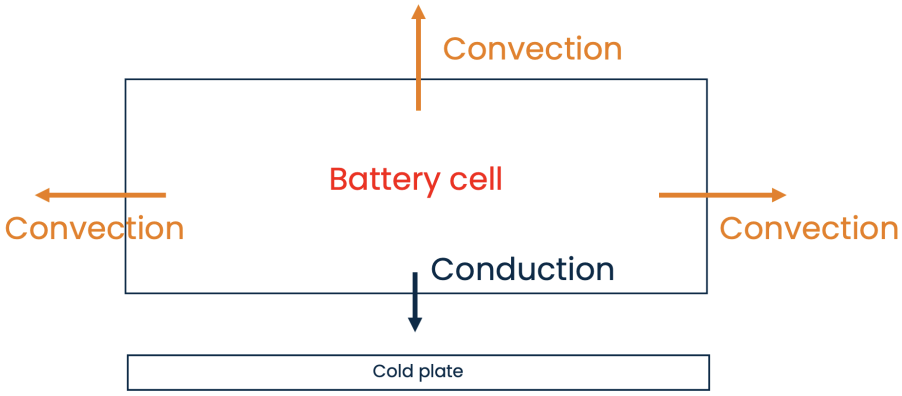

Figure 3.6: Schematization of heat transfers with the cold plate at constant temperature

cell is already described by equation 3.25.

Also in this case it's possible to define an electric analogy between $\dot{Q}_{\text{cond}}$ (3.24) and the Ohm's law (3.29), as we have done previously with the convection.

The equivalent conduction thermal resistance R_{cond}, is defined again as the ratio of the temperature difference ΔT across the material to the heat flow $\dot{Q}_{\text{cond}}$ through it, and making reference to equation 3.24 it will be:

$$R_{cond} = \frac{s_{cp}}{k_{cp} A_{cond}} \tag{3.49}$$

The thermal behavior of the cell is precisely described by equation 3.25, taking into account both conduction with the cold plate and convection with the air, as it's schematized in figure 3.6. For the calculation of A_{air}, the bottom surface is excluded with respect to the previous case, because now it corresponds to the area where heat is exchanged by conduction with the cold plateA_{cp}.

Considering 3.27, 3.30 and 3.49, the differential equation can be written as:

$$\frac{dT_{cell}}{dt} = \frac{R_{\text{int}} i(t)^2}{C_{cell}} - \frac{(T_{\text{cell}}(t) - T_{\text{cp}})}{R_{cond} C_{cell}} - \frac{(T_{\text{cell}}(t) - T_{\text{air}})}{R_{conv} C_{cell}} \tag{3.50}$$

The resolution of the differential equation follows the same methodology applied

in the previous section and will not be further detailed in this section or subsequent ones. Additionally, the thermal dynamics of the system will be directly analyzed in its differential form using Simulink.

3.2.4 Thermal model with variable temperature cold plate

A more realistic model is now created, considering the thermal evolution not only of the cell but also of the cold plate, and the interaction between the two.
For this reason two correlated differential equations have to be introduced to describe the overall system behaviour: one related to the cell as in the previous case, and one related to the cold plate. This means that in this case we no longer assume that the cold plate has an infinite heat capacity: (T_{cp} is not a constant anymore but its dependency on time is specified ($T_{cp}(t)$).

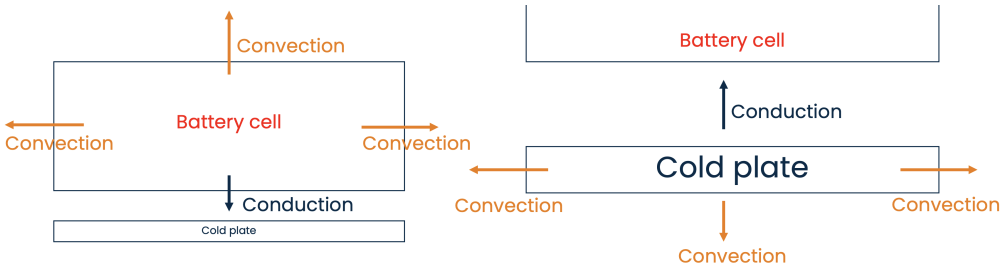

Figure 3.7: On the left the schematization of cell heat transfers, on the right the schematization of cold plate heat transfers

Focusing on the battery cell, the same heat transfer scheme described in section 3.2.3 applies: convection occurs on the lateral and top surfaces, while conduction occurs on the bottom surface. For the cold plate, convection with air takes place on the lateral surfaces, and conduction with the battery cell occurs on the top surface. The theoretical considerations outlined previously also apply to the cold plate.
The theoretical considerations outlined previously for the cell, also apply to the cold plate.

With reference to equation 3.14 in this case no thermal power $\dot{Q}_{in}$ is generated in the cold plate since no current is flowing inside ($\dot{Q}_{joule} = \dot{Q}_{entropy} = 0$).
$\dot{Q}_{out}$ is still the sum of the dissipated conduction and convection thermal powers of the cold plate, $\dot{Q}_{conv-cp}$ and $\dot{Q}_{cond-cp}$:

$$\dot{Q}_{\text{conv-cp}} = hA_{\text{air-cp}}(T_{\text{cp}}(t) - T_{\text{air}}) \tag{3.51}$$

where $A_{\text{air-cp}}$is the area of contact cold plate-air

$$\dot{Q}_{\text{cond-cp}} = \frac{k_{\text{cell}}A_{\text{cond}}}{s_{\text{cell}}}(T_{\text{cp}}(t) - T_{\text{cell}}) \tag{3.52}$$

where A_{cond} is kept identical to the one in equation 3.24, since heat flows cold plate-cell and cell-cold plate are obviously referred to the same area, k_{cell} is the thermal conductivity of the cell and s_{cell} is the thickness of the cell in the direction of the heat flow, so cell's height in this case.
After these considerations equation 3.25 can be expressed for the cold plate as:

$$m_{cp}c_{\text{cp}}\frac{dT_{cp}}{dt} = -\frac{k_{\text{cell}}A_{\text{cond}}}{s_{\text{cell}}}(T_{\text{cp}}(t) - T_{\text{cell}}(t)) - hA_{\text{air-cp}}(T_{\text{cp}}(t) - T_{\text{air}}) \tag{3.53}$$

Also in this case the product of the mass m_{cp} and the specific heat capacity c_{cp} can be written as:

$$m_{cp}c_{\text{cp}} = C_{cp} \tag{3.54}$$

with C_{cp} the heat capacity of the cold plate.
Similarly to what we have done for the cell again we can define the convective thermal resistance:

$$R_{\text{conv-cp}} = \frac{1}{hA_{air-cp}} \tag{3.55}$$

and the conductive thermal resistance:

$$R_{\text{cond-cp}} = \frac{s_{cell}}{k_{cell}A_{cond}} \tag{3.56}$$

The final form of equation 3.53 is now derived:

$$\frac{dT_{\text{cp}}}{dt} = \frac{T_{cell}(t)}{R_{\text{cond-cp}}C_{cp}} + \frac{T_{\text{air}}}{R_{\text{conv-cp}}C_{cp}} - T_{\text{cp}}(t)\left(\frac{1}{R_{\text{cond-cp}}C_{cp}} + \frac{1}{R_{\text{conv-cp}}C_{cp}}\right) \tag{3.57}$$

In conclusion the thermal evolution of the battery cell in this more realistic scenario has to be described by combining equations 3.50 (with $T_{cp}(t)$ instead of T_{cp}) and 3.57 into a single system:

$$\begin{cases} \dfrac{dT_{cell}}{dt} = \dfrac{R_{\text{int}}i(t)^2}{C_{cell}} + \dfrac{T_{\text{cp}}(t)}{R_{\text{cond}}C} + \dfrac{T_{\text{air}}}{R_{\text{conv}}C} - T_{cell}(t)\left(\dfrac{1}{R_{\text{cond}}C_{cell}} + \dfrac{1}{R_{\text{conv}}C_{cell}}\right) \\ \dfrac{dT_{\text{cp}}}{dt} = \dfrac{T_{cell}(t)}{R_{\text{cond-cp}}C_{cp}} + \dfrac{T_{\text{air}}}{R_{\text{conv-cp}}C_{cp}} - T_{\text{cp}}(t)\left(\dfrac{1}{R_{\text{cond-cp}}C_{cp}} + \dfrac{1}{R_{\text{conv-cp}}C_{cp}}\right) \end{cases} \tag{3.58}$$

For the resolution of the system, the initial temperature of the cold plate T_{cp0} has to be established:

$$T_{cp}(0) = T_{cp0} \tag{3.59}$$

3.2.5 Thermo-electrical model

Thus far the internal resistance of the cell R_{int} has been assumed to be constant, but in practice this constitutes a simplification, as it depends both on the SOC and

on the ambient temperature $R_{\text{int}}(SOC, T)$. An increase in temperature leads to an increase of ionic conductivity thereby reducing the internal resistance; conversely a reduction of the SOC indicates a reduction of reactant concentration, leading to less efficient and slower electrochemical reactions and, consequently, higher internal resistance.
Considering the purposes of this analysis, experimental validation of the model has been conducted in a laboratory under controlled environmental conditions and constant temperature, thus only the influence of the SOC has been taken into account ($R_{\text{int}}(SOC)$).

$$\frac{dT_{cell}}{dt} = \frac{R_{\text{int}}(SOC)i(t)^2}{C_{cell}} + \frac{T_{\text{cp}}(t)}{R_{\text{cond}}C} + \frac{T_{\text{air}}}{R_{\text{conv}}C} - T_{cell}(t)\left(\frac{1}{R_{\text{cond}}C_{cell}} + \frac{1}{R_{\text{conv}}C_{cell}}\right) \tag{3.60}$$

For this reason an accurate description of the SOC evolution as function of the input current provided, has to be incorporated in the model.
Electrical performance of the cell can be studied on Simulink using the Equivalent Circuit Battery. This unit schematize the behaviour of the cell through an Equivalent Circuit Model (ECM) that provides as output the SOC and the voltage of the cell (Simulink model will be displayed in the next chapter).
A second order RC circuit model, reported in figure 3.4, has been chosen for our study case, since it represents the best trade-off in terms of complexity and accuracy of the results to describe cell's electrical dynamic behaviour.

It consists of four different components connected in series:

- V_{ocv}: which is the open circuit voltage, indicated with an ideal voltage source. It represents the voltage across the cell terminals when no external load is connected and can be considered as the ideal output voltage that the cell

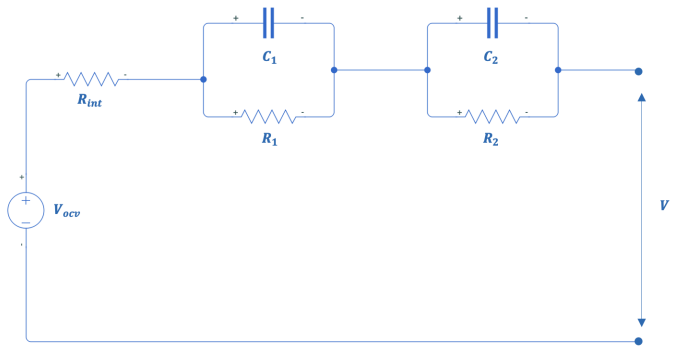

Figure 3.8: Equivalent Circuit Model

would have if no voltage drops were occurring when current is flowing.

- R_{int}: which is the internal resistance, of the cell

- R_1C_1: which is the first RC branch. They are parallel connected and represent respectively the electrochemical polarization resistance and the transient response of cell's charge and discharge process [62]

- R_2C_2: which is the second RC branch. Again parallel connected, they represent respectively the concentration polarization resistance and the polarization caracteristic of the cell

All these parameters $(R_1, R_2, C_1, C_2, V_{ocv})$ are functions of the state of charge and for this reason they have to be provided as vectors, using look-up tables taken from the datasheets, describing their dependency on the SOC.
For the estimation of the outputs, the Simulink block uses the following equations [63]:

$$V = V_{ocv} - R_{\text{int}} i(t) - V_1 - V_2 \tag{3.61}$$

$$V_{1,2} = \int_0^t \left[\frac{i(t)}{C_{1,2}} - \frac{V_{1,2}}{R_{1,2}C_{1,2}} \right] dt \tag{3.62}$$

$$\mathrm{SOC} = -\frac{1}{C} \int_0^t i(t)\, dt \tag{3.63}$$

where V_1 and V_2 are the voltages drop of the two RC branches connected in series to R_{int} and V_{ocv}, V is the cell output voltage and C is the cell capacity. The computed SOC is used to define the corresponding internal resistance, $R_{\mathrm{int}}(SOC)$. Together with the current they represent the inputs of the cell thermal model which is now integrated as a subsystem within the final thermo-electrical model.
This comprehensive cell model will be adopted for the validation of experimental results obtained in the laboratory.

Chapter 4

Simulation Results and Analysis

The comprehensive thermo-electric model of the cell, formulated in the methodology and derived from the previously described equations, requires experimental validation to ascertain its accuracy and consistency.

The objective of this fourth chapter is to implement the system on Simulink, populating it with input specifications of the real cell taken from datasheets, and to compare the experimentally obtained results with those predicted by our model.

As we have already mentioned the equivalent circuit cell block models the electrical behaviour of the cell as a second order equivalent circuit (3.8), and the link with the thermal model is related to the internal resistance. Equivalent circuit block requires as inputs the data of the electrical components of the circuit as function of the SOC ($V_{ocv}(SOC), R_1(SOC), R_2(SOC), C_1(SOC), C_2(SOC)$), as well as the current profile to which the cell is subjected; no ambient temperature dependency is taken into account since the tests are conducted at controlled and constant T_{air}. The outputs instead are the cell voltage and the SOC evolution: the former is

compared with the experimental measured voltage of the cell to assess the validity of the equivalent circuit block while the latter one serves as the input of the internal resistance look up table (with $R_{int}(SOC)$ sourced from datasheets).
The output of this table together again with the input current profile, are the inputs of the thermal model, which as we have already mentioned is now a subsystem of the overall one.
The final output of the system is the cell temperature $T_{cell}(t)$ which has to be compared to the experimentally measured one to assess the validity of the result.

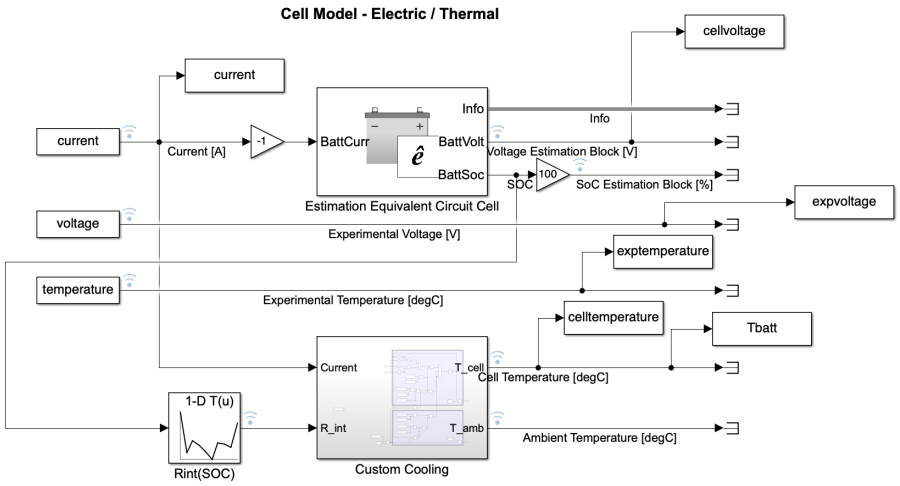

Figure 4.1: Thermo-electric simulink model

Even if CALB L221N147A turned out to be the best cell for our case study (reasons listed at the end of section 3.1.2), it hasn't been possible to acquire and test this specific cell in the laboratory. Additionally, there are no accessible online data detailing the thermal behavior of the cell, nor are there any available parameters for resistance and capacitance as functions of the SOC, which are essential for populating the equivalent circuit block.
The objective of validation however, is to establish the model's accuracy and verify its predictive capability. Once the model reliability is assessed, the equations on

which it's based have general validity independently from the type of cell considered, and do not vary from case to case. Consequently, in the absence of laboratory availability for experimental testing on the CALB, an alternative approach has been adopted, identifying a possible online cell database that could provide both the necessary parameters required for the model and the cell temperature evolution $T_{cell}(t)$ under a specified current profile.
SAMSUNG INR 21700 30T cell has been selected for model validation. Experimental tests on this type of cell were conducted by Kollemeyer et al. [64] at McMaster University in 2020, and the results have been made available on Mendeley Data. The datasheet provides all necessary parameters for validation, including the thermal evolution of the cell under various ambient temperatures; in this study, we have specifically considered the case where $T_{air} = 24°C$.

4.1 Validation of the model with SAMSUNG IN21700 30T

The SAMSUNG INR 21700 30T, considered for validation in this study, is a Lithium-ion cell characterized by a hybrid chemistry composed of Nickel, Manganese, and Cobalt (NMC), as the prismatic CALB. The designation '21' refers to the cell's diameter in millimeters, '70' denotes its height in millimeters, and the final '0' indicates its cylindrical form. The '30T' instead is related to the capacity of 3000 mAh. Figure 4.2 illustrates the geometry of the cell, while cell characteristics documented in the datasheet have been collected and summarized in table below 4.1. Cell specific heat capacity has been realistically estimated to be 1800 $\frac{J}{kg \cdot K}$.

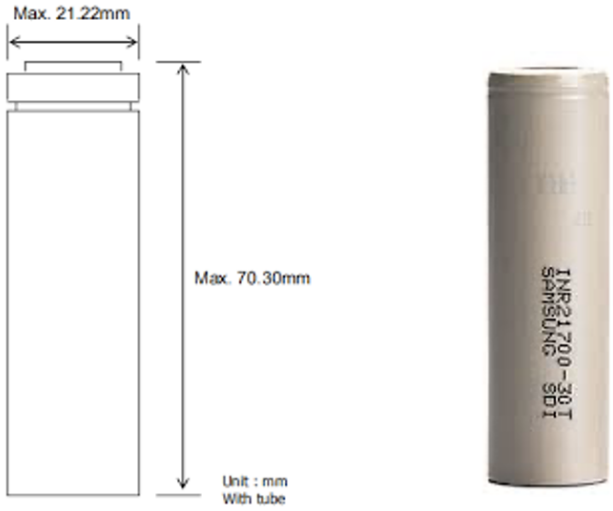

Figure 4.2: SAMSUNG INR 21700 30T geometry

Geometry	Cylindrical	-
Height	70.3	mm
Diameter	21.22	mm
Weight	69	g
Max Voltage	4.2	V
Nominal Voltage	3.6	V
Nominal Capacity	3	Ah
Max discharge current	35	A
Max recharge current	10	A
Discharge cut-off voltage	2.5	V

Table 4.1: SAMSUNG INR 21700 30T data

Before describing the simulation setup and analyze the results, the electrical parameters have still to be defined for the different SOCs considering the temperature at which the test is conducted (24°). Resistances and capacitances of the second order equivalent circuit are detailed in table 4.2

SOC%	$R_{int}[ohm]$	$R_1[ohm]$	$C_1[F]$	$R_2[ohm]$	$C_2[F]$
10%	0.0135	0.0071	254.83	0.0053	93.222
20%	0.0089	0.0081	7981.3	0.0019	1356.7
30%	0.0102	0.0097	7726.9	0.0020	2097.1
40%	0.0097	0.0099	7556.9	0.0019	1952.0
50%	0.0090	0.0063	6875.9	0.0023	1072.3
60%	0.0081	0.0141	6072.1	0.0035	630.45
70%	0.0100	0.0136	7042.4	0.0018	1840.9
80%	0.0099	0.0084	4146.3	0.0020	1149.1
90%	0.0095	0.0019	6358.1	0.0018	1541.8
100%	0.0122	0.0236	5376.6	0.0019	1478.4

Table 4.2: SAMSUNG electrical parameters as function of SOC [65]

The last electric parameter to be defined is the cell open circuit voltage V_{ocv}: its dependency on the state of charge in this case is not reported in a table but it's graphically represented in figure 4.3. When the cell is charged, the concentration of lithium ions increases in the anode, increasing the electrochemical potential. This increase in potential difference results in a higher V_{ocv} which therefore will be larger at higher SOCs

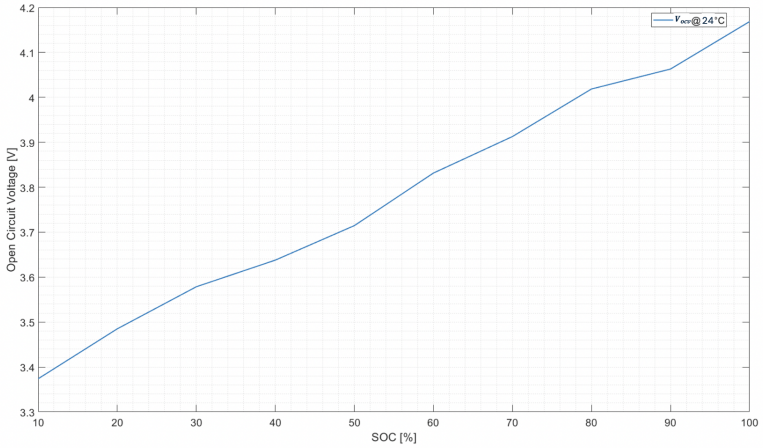

Figure 4.3: SAMSUNG V_{ocv} as function of SOC

4.1.1 Simulation setup and parameters estimation

It's now possible to focus on describing the procedure for the validation of the thermo-electrical model and how it has been carried out.

As previously mentioned, the objective of the test is to experimentally measure the temperature evolution of the cell and compare it with the $T_{cell}(t)$ output of the simulink model, verifying the similarity and coherence between the two signals, to assess the reliability of the system. Although the terminals typically experience a greater temperature increase than the rest of the cell during charging, the cell temperature has been considered uniform for this analysis, which is a reasonable simplification for achieving a model that is the best trade-off between accuracy and computational efficiency.

The current profile adopted in the test is a repeated four-pulse discharge HPPC test, with discharge rates of 1C, 2C, 6C and 12C and charge rates of 0.5C, 1C, 2C and 4C.

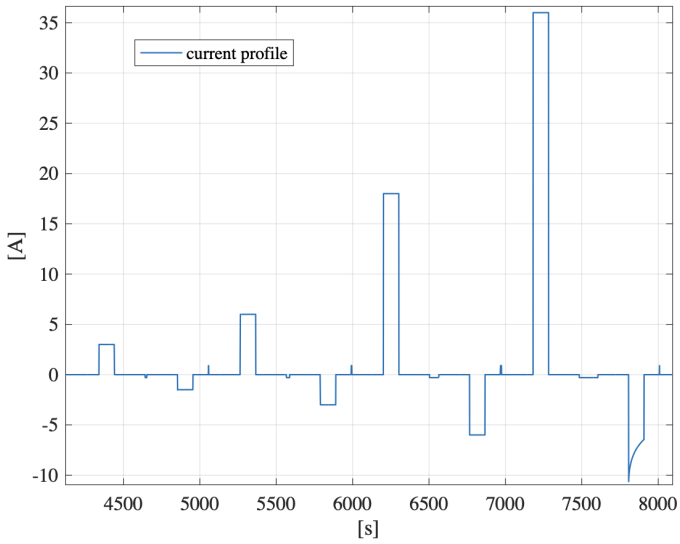

Figure 4.4: Four pulse HPPC test

In Simulink, the estimation equivalent circuit cell block conventionally considers current to be positive during charging and negative during discharging, which is the opposite of what is depicted in figure 4.4. For this reason, in figure 4.1 the current is multiplied by -1 before being used as input for the ECM.
The cell is connected to the test cycler using conductive clamps placed at its extremities, as illustrated in figure 4.5. As a result the surface for convection heat transfer with air A_{air} will be the lateral surface of the cell, while the surface for conduction heat transfer A_{cond} is the sum of the two base surfaces in contact with the clamps.

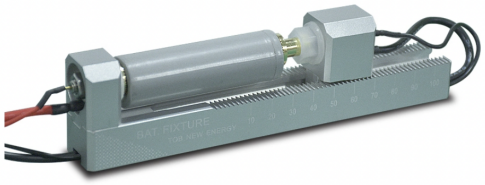

Figure 4.5: Cell arrangement for the test

Since A_{cond} is sufficiently small, the thermal evolution of the clamps (analogous to the cold plate described in the methodology) has not been taken into account. Its influence on the final results is very marginal, and it would only increase the complexity of the system.
Datasheets do not provide information regarding the thickness of the clamps, which has been assumed to be realistically 20 mm, and clamps material, which has been assumed to be alumina. The corresponding thermal conductivity is detailed in table **??**.

k_{cp}	20	$\frac{W}{m \cdot K}$
s_{cp}	20	mm

Table 4.3: Clamps thermal conductivity and thickness

The last parameter required before launching the simulation is the convective heat transfer coefficient h. This parameter is very challenging to be estimated and it's generally obtained experimentally, as it varies from case to case according to the fluid dynamics and the characteristics of the surface through which convection occurs. For this study a realistic value of $h = 7.5 \frac{W}{m^2 \cdot K}$ has been considered.
With this parameter defined, the thermo electric model is now complete and the simulation can start.

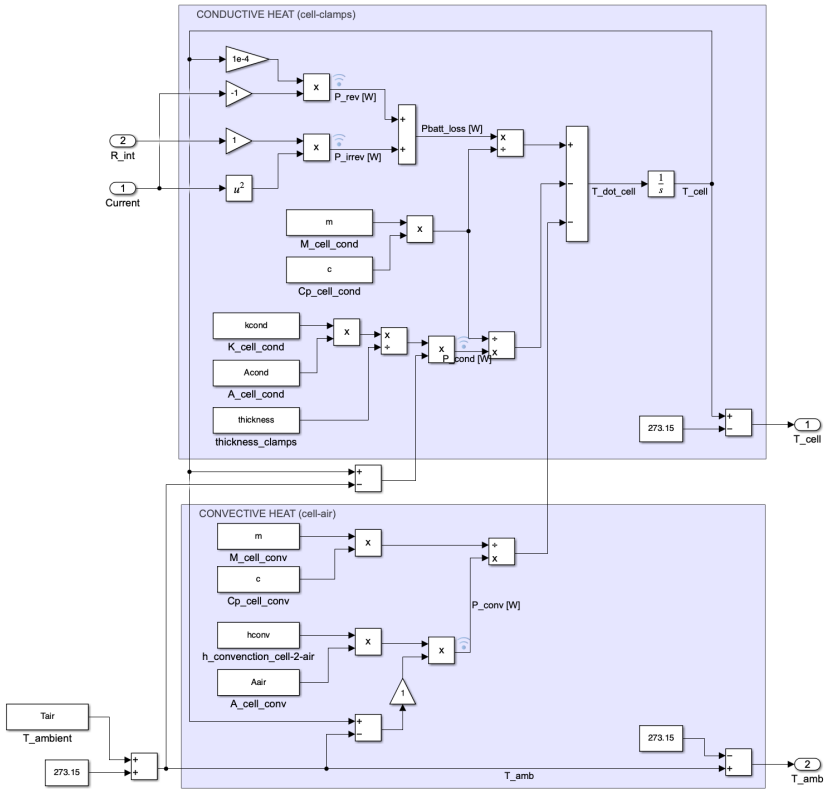

Figure 4.6: Thermal subsystem

A focus on the thermal subsystem of the complete thermo-electric simulink model (figure 4.1) is illustrated in the figure 4.6, which depicts the Simulink implementation of the cell thermal differential equation. The initial temperature of the clamps is assumed to be equal to the ambient temperature $T_{air} = T_{cp}$=24° while the initial cell temperature in the test of Kollemeyer, has been set equal to 23.5°.

The simplified purely convective thermal model, as described in section 3.2.1 (when no cold plate is present), can be easily obtained by setting k_{cp} to zero.

For completeness the entropy contribution is also included $\dot{Q}_{\text{entropy}}$: the ratio of equation 3.20 has been approximated to a realistic value of 1×10^{-4}. As previously noted, this contribution is negligible and does not affect the results obtained.

4.1.2 Results and Experimental Data Comparison

We can now analyze the outputs obtained from the simulation and compare them with the experimental results provided by Kollemeyer et.al. The simulation has started with the fully charged cell (initial SOC = 100%) and has been carried out for 105.000 seconds (almost 30 hours), following the repeated current profile described in section 4.1.1 until the cell has reached a state of charge of 15%.

Figure 4.7 illustrates the state of charge evolution. It can be observed that after each repeated cycle, there is nearly a 10% drop in SOC. This drop is primarily due to the last discharging pulse of 12C in the cycle (refer to figure 4.4). The small increases of the SOC that can be noted in the plot instead are related to the charging phases of the current profile, which however are relatively minor compared to the discharging ones. Consequently, the overall effect of the repeated current profile is the gradual discharge of the cell.

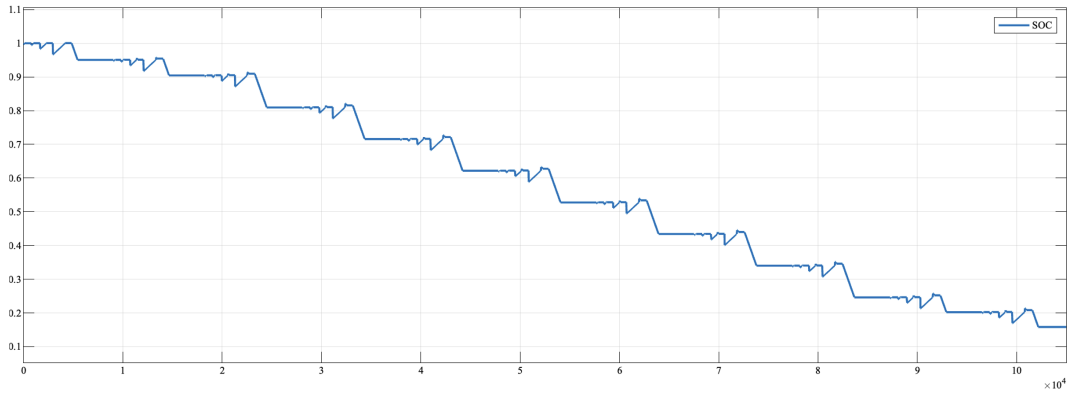

Figure 4.7: State of charge evolution

Before comparing the simulation $T_{cell}(t)$ with the experimental temperature, it is necessary to perform an intermediate validation of the equivalent circuit model. This validation aims to assess the reliability of the electrical parameters used in the model and to ensure that the internal resistance look-up table (and consequently the thermal subsystem) is receiving the correct input signal.
The experimentally measured voltage signal at cell's terminals is reported in the datasheet, and has been used as reference for the comparison with the simulated voltage obtained in Simulink. According to the decrease in the open circuit voltage shown in figure 4.3, a corresponding decrease in cell voltage is expected.

In the comparison shown in figure 4.8, the experimental voltage (indicated in orange) is nearly superimposed on the estimated voltage (in blue). The validation can be performed by analyzing the absolute error between the two signals according to equation 4.1, where $y(t)$ and $\hat{y}(t)$ are respectively the experimental voltage and the estimated one.

$$e(t) = |y(t) - \hat{y}(t)| \tag{4.1}$$

Although the model is less precise at very low SOC, for where its output is

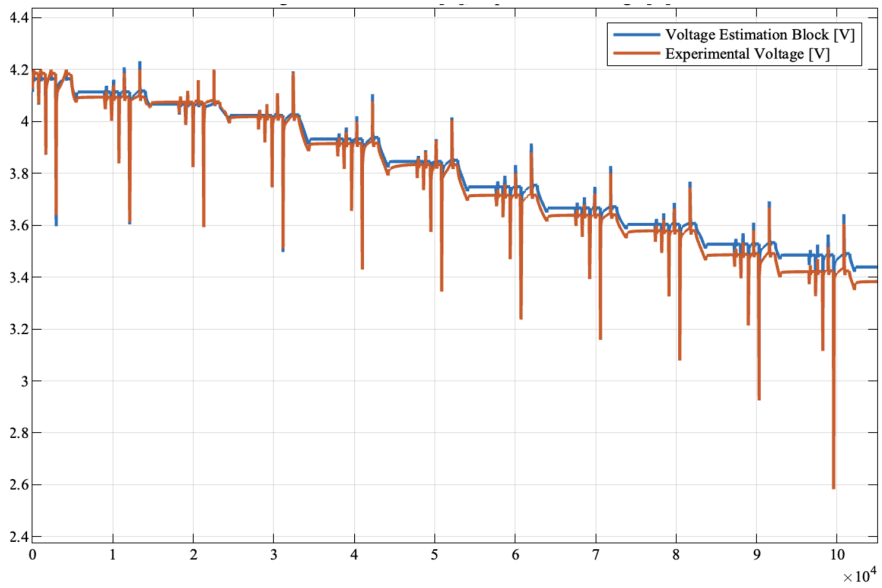

Figure 4.8: Experimental cell voltage vs Estimated cell voltage

slightly shifted to higher values compared to the experimental ones, the two trends are still consistent, and the maximum absolute error obtained is only of 0.36 V. Due to this small shift, a slight difference between the peak temperatures of the estimated and measured $T_{cell}(t)$ can be expected in the last cycles.

Another statistical index that can be considered for the validation, is the root mean square error, calculated as in 4.2 with again $y(t)$ and $\hat{y}(t)$ indicating the experimental and the estimated voltage signals.
A RMSE of 0.0317 has been obtained, which is a satisfactory result for assessing the validity of the ECM and the correctness of the parameters adopted for populating the simulink block.

$$\text{RMSE} = \sqrt{\frac{1}{n}\sum_{i=1}^{n}(y_i - \hat{y}_i)^2} \tag{4.2}$$

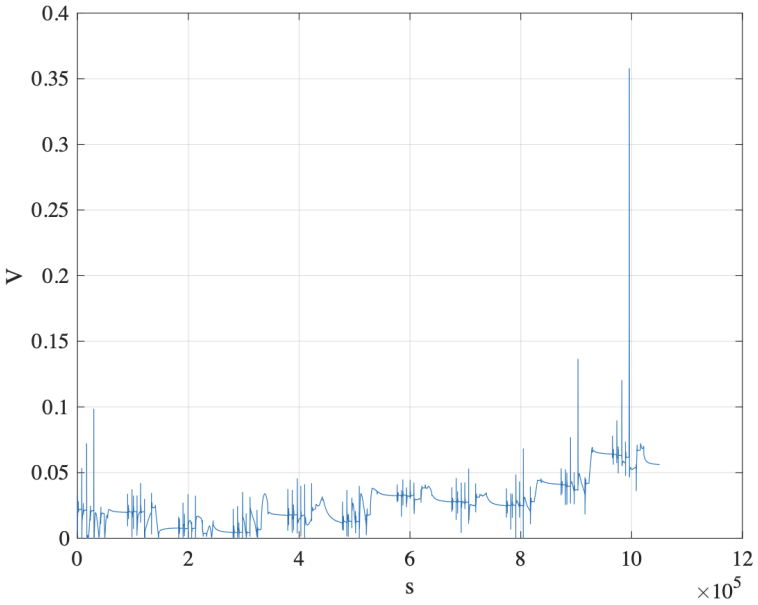

Figure 4.9: Voltage absolute error

Focusing on the temperature evolution, we initially considered a simplified model that only includes convection, neglecting the contribution of conduction heat transfer with the clamps. The resulting $T_{cell}(t)$ is represented in red in figure 4.10 together with the corresponding current profile (in blue).

Each current pulse, whether during charging or discharging, results in a temperature increase, starting from the initial temperature of 23.5° and reaching peak temperatures of 25.5° during the most demanding 12C discharging pulse. The evident initial increase of the temperature is also related to the 0.5° difference between T_0 and the surrounding air temperature (T_{air})=24°. For this reason at the beginning the cell experiences heating not only due to the current flow but also due to the positive contribution of convective thermal power, as the temperature difference in equation 3.31 is negative.

After each pulse a temperature decrease is registered, corresponding to the rest phases of current profile. The rate at which this temperature decreases depends on

the thermal time constant τ_{th} which in this case depends only on the convective thermal resistance R_{conv} and on the cell's heat capacity.

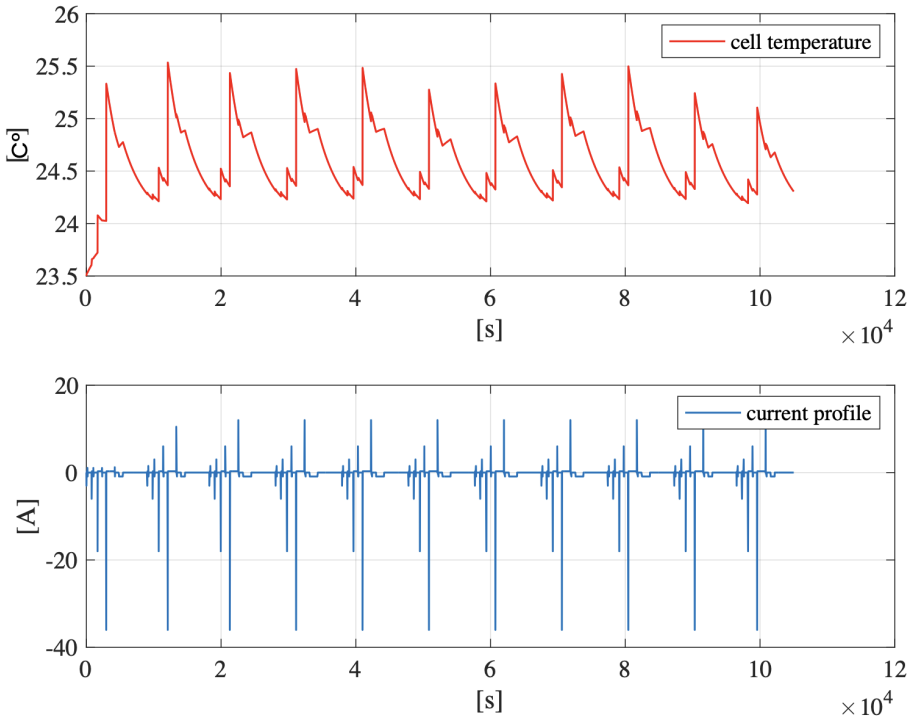

Figure 4.10: Estimated cell temperature only with convection

The result obtained can be now compared to the experimental one. In figure 4.10 the two signals are indicated: in blue the cell temperature estimated by the model and in orange the experimentally measured T_{cell}.

The first thing that can be observed is that the model provides an excellent approximation of the peak temperatures with max values of T_{cell} nearly perfectly superimposed, and accurately predicts the timing of each rise. A slight difference can be observed in the last two cycles. This discrepancy is more likely to be attributed to some inaccuracies of the ECM, highlighted and discussed previously comparing the voltage signals and shown in figure 4.9, rather than being related to the thermal model itself.

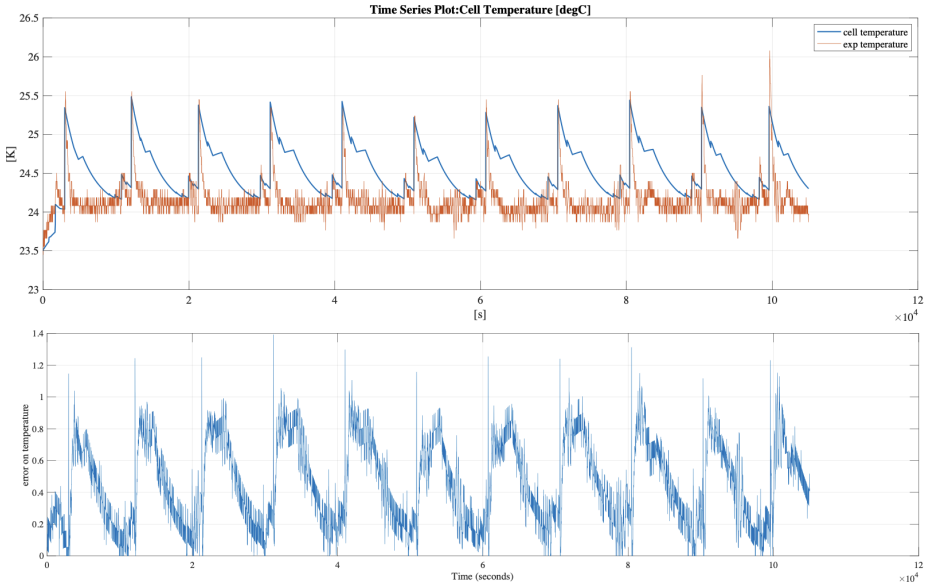

Figure 4.11: Experimental cell temperature vs Estimated cell temperature only with convection and absolute error

However the trends of the two temperature signals are not perfectly aligned, as it can be observed in 4.11 also by looking at the absolute error obtained, whose maximum value reached is 1.4°. The residuals are non negligible, oscillating with an amplitude of 0.9° after each cycle and also the computed RMSE of 0.5237 suggests that improvements are required. This indicates that the model's thermal time constant is not properly calibrated and is too large compared to the real case. By zooming in on a single cycle of figure 4.11, this misalignment appears evident: the temperature drop in the experimental data is much faster, reestablishing to the ambient temperature before the next cycle begins. In contrast, the estimated temperature drop is slower, preventing the cell from fully cooling down between consecutive cycles and stabilizing again at 24°C.

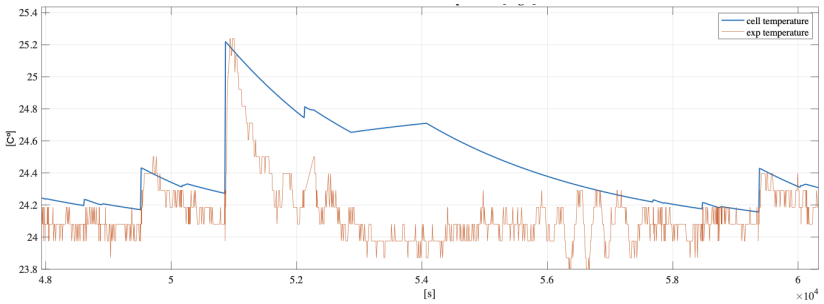

Figure 4.12: Zoom on cell temperature only with convection

This discrepancy could have been expected as the model is considering only convection heat transfer, completely neglecting the heat transfer exchanged with the clamps at the cell terminals. Given this simplification, model's performance can't be considered validated yet, as a more accurate superposition of the temperature trends and a reduction of the absolute errors is needed.

For this purpose, to achieve a more representative and realistic model of the tested cell, the simulation has been repeated including also the conduction thermal power contribution $\dot{Q}_{\text{cond}}$. Parameters of the clamps are reported in table 4.3 (as said the surface of conduction heat transfer A_{cond} is the sum of the base surfaces of the cell).

Again the resulting $T_{cell}(t)$ (in red) is reported together with the same current profile (in blue) in figure 4.13.

Also in this case each charge and discharge pulse results in a temperature increase, but the first evident difference can be observed during the rest phases of current profile: the temperature drops are significantly sharper compared to the previous scenario which only considered convection (figure 4.10), which indicates that the thermal time constant τ_{th} is much smaller in this case.

Again the absolute error is represented, and it can be noticed that despite the

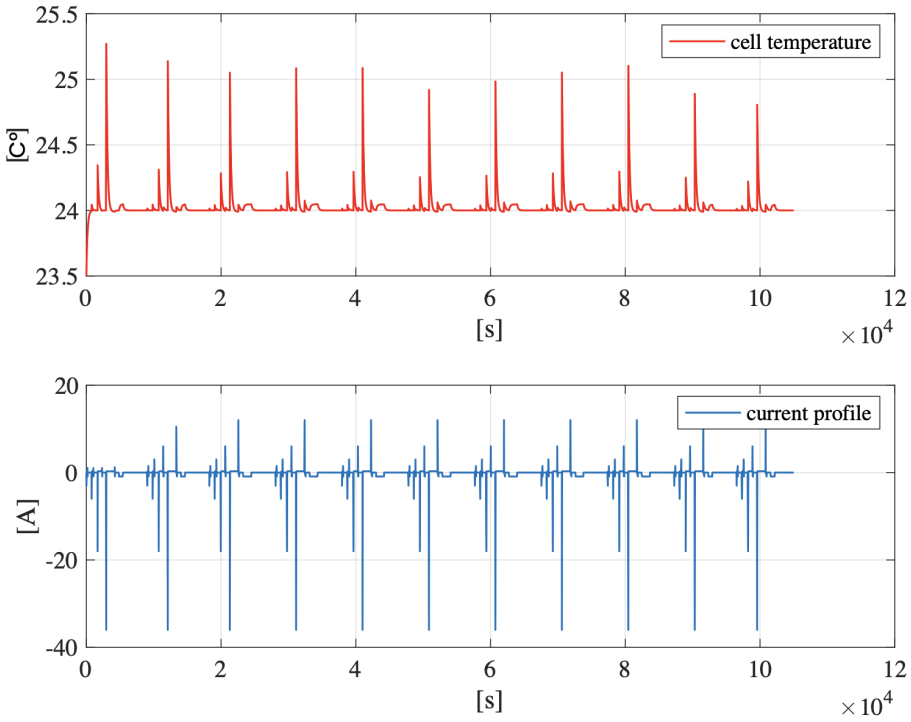

Figure 4.13: Estimated cell temperature with conduction

oscillations related to the noise of the measured experimental signals, and the few peaks of some seconds (depending on a minimum lag of the estimated T_{cell} with respect to the experimental one, in reaching the peak temperature), the max error obtained is of 0.4° which represents a consistent improvement with the previous simulation, allowing us to assess the reliability of the model.

The validity of the system is confirmed also by the RMSE that is reduced to 0.1315, which is a satisfactory result, sufficient for saying that the model created is capable of describing the thermal behaviour of the battery cell. This result is consistent with our expectations as in this case heat generated by the current flowing in the cell is dissipated not only by the surrounding air, but also through conduction heat transfer with the clamps, according to equation 3.50. Consequently the maximum temperatures reached will be slightly lower than the previous case.

The initial cell temperature T_0 and T_{air} have been kept the same as previously (respectively 23.5° and 24°), and the temperature of the clamps, as said previously, is simplified as constant and assumed to be equal to the air temperature. Therefore again an initial significant temperature rise can be observed, which however is even sharper than before. In this scenario the cell heats up not only due to the current flow and the positive contribution of convective thermal power described above, but also due to the positive conduction term indicated in equation 3.50, as the temperature difference $T_{cell}(t) - T_{cp}$ is negative at the beginning.

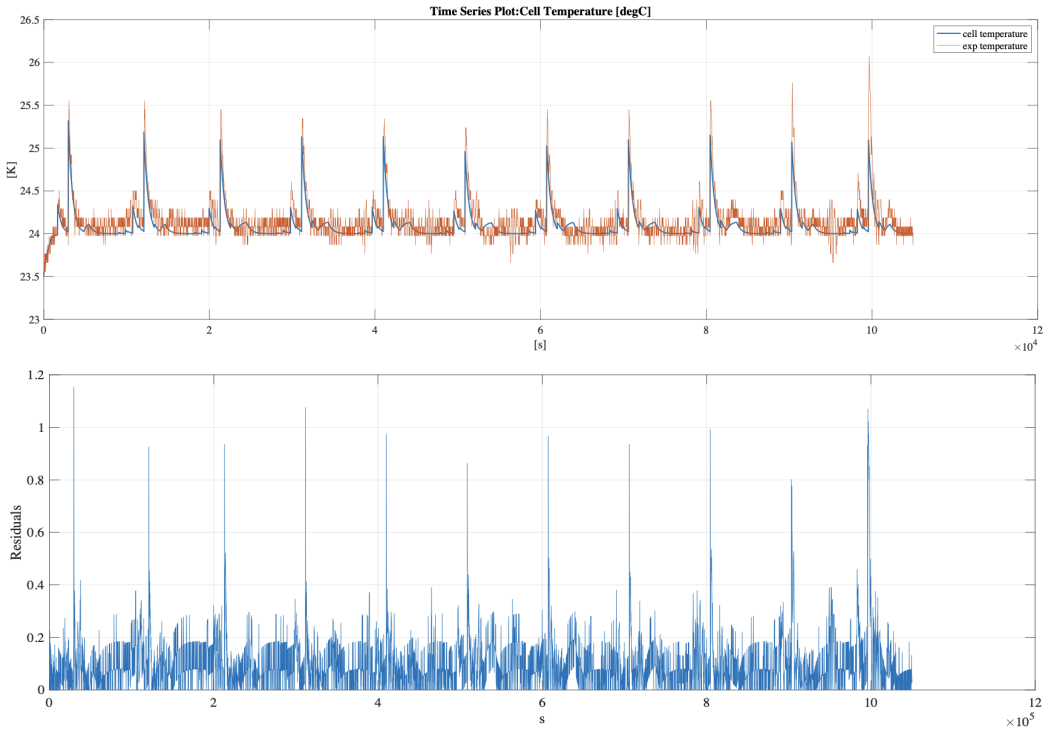

Figure 4.14: Experimental cell temperature vs Estimated cell temperature with conduction and absolute error

By zooming in on a single cycle, we can appreciate how the trend of the two signals, are almost superimposed, despite some noise in the experimentally measured one, solving the problem of slow temperature decrease observed in the previous scenario. The slight imperfect matching of peak temperatures can be related not only

to inaccuracies of the ECM electrical parameters as before, but in this case it's also related to the uncertainty of k_{cp} and s_{cp}, since no data were provided in the reference.

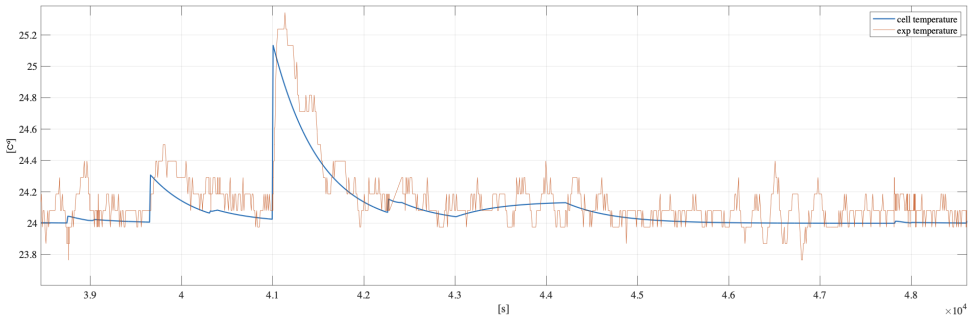

Figure 4.15: Zoom on cell temperature with conduction

In conclusion this comparison demonstrates that the model which includes also the conduction thermal contribution, provides an accurate approximation of the cell temperature in the given conditions, confirming its validity and the consistency of the equations on which it's based.
Having assessed its reliability, we have successfully achieved our objective of defining a comprehensive thermo-electrical system which can now be used to predict the thermal behavior of other battery cells with different current profiles by simply modifying the input parameters.

4.2 Thermo-Electrical Modeling of CALB L221N147A

The thermo-electric model validated with the cylindrical Samsung can be now exploited to predict the thermal behavior of the optimal cell defined in the preliminary battery sizing, for which no experimental data were available. Therefore the objective of the second part of this chapter on simulation results is to study the thermal evolution of CALB L221N147A as function of the provided current profile,

by changing the system's inputs parameters.

Figure 4.16: CALB L221N147A prismatic cell

As we are dealing with a prismatic cell, conduction heat transfer in this case occurs with the cold plate positioned in contact with its base surface, as schematized in figure 3.7, while on the lateral and on the top surface there will be the dissipation of convective thermal power with the air.
A further step that has been performed with respect to section 4.1 is eliminating the assumption of constant cold plate temperature with infinite heat capacity. Considering the dimensions of the cell reported in table 3.9, the surface of conduction heat transfer A_{cp} is much larger than the area of the previously described clamps. Consequently the thermal evolution of the cold plate can no longer be neglected, as done in the validation.

SOC	0%	10%	20%	30%	40%	50%	60%	70%	80%	90%	100%
V_{ocv}	3.411	3.494	3.576	3.630	3.669	3.736	3.864	3.977	4.091	4.178	4.312

Table 4.4: CALB Open circuit voltage

Open circuit voltage and cell internal resistance as function of the SOC are provided in the datasheet and reported in tables 4.4 and 4.5 considering an ambient

temperature of 25° (R_{int} reported in $m\Omega$). As we can see the internal resistance increases significantly only at very low SOCs, while for state of charges larger than 20% it's almost kept constant.

SOC	5%	20%	50%	80%	95%
R_{int}	0.84	0.43	0.41	0.43	0.44

Table 4.5: Internal resistance as function of the state of charge

The other parameters required for populating the ECM (R_1, R_2, C_1, C_2) are not provided in the datasheet. A first order ECM has been considered and R_1 and C_1 have been estimated and assumed as constants (respectively 0.5 $m\Omega$ and 2000 F). Real electrical parameters will be obtained by testing the real cell in the laboratory as mentioned in the future works.

4.2.1 Analysis and interpretation of model results

The model adopted for this analysis is the implementation of the system of differential equations described in section 3.2.4, since also the thermal evolution of the cold plate is being considered. For this reason the outcome of the simulation is not just $T_{cell}(t)$ anymore, but also $T_{cp}(t)$ is reported in figure 4.17.
In this case also the cold plate increases its temperature due to the conduction heat exchange with the CALB. The cell however experiences a more pronounced temperature rise because of its lower thermal conductivity.
The simulation on the CALB L221N147A has been carried out initially considering a step current profile of 150A (corresponding to cell capacity) for 30 minutes, followed by no current for the subsequent 30 minutes resulting in a total simulation time of one hour. Simulation has been then repeated considering a real WLTC cycle current profile, obtained by dividing the provided WLTC electrical power by the output voltage of ECM block. As it will be noted in both cases the temperature

increase registered for the cell is marginal, because both current profiles are not very demanding relatively to the very high cell nominal capacity of the CALB. The aim of this analysis however is to obtain a qualitative baseline for understanding the thermal behavior of the battery cell, identifying how it handles heat generation and dissipation; no experimental data are available for an outcome comparison, as well as no information on the cold plate thickness and material are indicated.

m	2.34	kg
c_{cell}	1040	$\frac{J}{kg \cdot K}$
k_{cell}	4.2	$\frac{W}{m \cdot K}$
T_0	308.15	K

Table 4.6: Cell parameters

Parameters required related to the CALB are reported in table 4.6. It's assumed that initially the cold plate and the cell have the same temperature of the surrounding air $T_{cp0} = T_0 = T_{air} = 25°$. Cell mass has been reported in the datasheet, while the thermal conductivity and the specific heat capacity have been realistically estimated according to the geometry and the chemistry of the CALB (prismatic NMC).

ρ	2700	$\frac{kg}{m^3}$
s_{cp}	0.035	m
k_{cp}	237	$\frac{W}{m \cdot K}$
c_{cp}	903	$\frac{J}{kg \cdot K}$
T_{cp0}	308.15	K

Table 4.7: Cold plate parameters

For this analysis we have assumed a cold plate with a thickness of 35mm, made of pure aluminum, whose properties in terms of density, thermal conductivity and

specific heat capacity are reported in table 4.7. Cold plate mass m_{cp} has been evaluated multiplying the density of the material by the volume (which is simply the product of the base surface of CALB cell multiplied by the thickness).

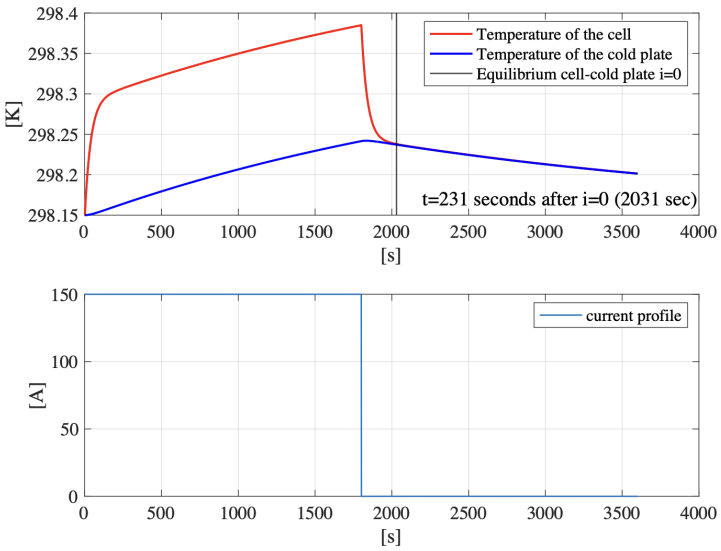

Figure 4.17: Thermal evolution of CALB cell and cold plate in correpsondance to the current profile

Considering the first simulation conducted with the step current of 150A, the initial rapid cell temperature increase is driven by Joule heating, until thermal equilibrium with the cold plate is achieved. Even if the two components have different temperatures, the difference is kept constant after the initial transient thermal evolution. Once the current instantly goes to zero, cell temperature drops down and it stabilizes again on the same temperature of the cold plate after 231 seconds. When the same temperature is reached, the further temperature decrease of the overall system is related to the heat dissipated by convection with air, and the rate of the decrease is governed by the component with slower thermal dynamics, in this case represented by the cold plate.

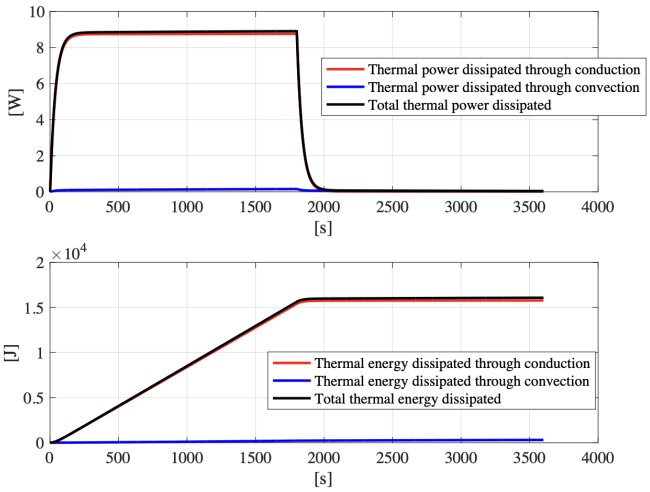

Figure 4.18: Thermal energy and power of CALB dissipated by conduction and convection

Figure 4.18 clearly illustrates how in this case convective heat dissipation is negligible compared to conductive dissipation: the black curve indicating the total $\dot{Q}_{out} = \dot{Q}_{conv} + \dot{Q}_{cond}$ is almost superimposed to the red one. Same considerations can be performed by observing the cumulative dissipated thermal energy, which is the integral in time of the corresponding dissipated power.

$$\begin{aligned} E_{conv} &= \int_0^t \dot{Q}_{conv}, dt \\ E_{cond} &= \int_0^t \dot{Q}_{cond}, dt \\ E_{tot} &= E_{cond} + E_{conv} \end{aligned} \tag{4.3}$$

Same considerations can be done for the results obtained in the second simulation with the WLTC current profile, reported in figure 4.19.
The simulation duration in this case is 1200s, one third of the previous case, with a variable current profile that lasts 1000 seconds and goes to zero for the final 200

seconds. In this plot is very evident how the thermal inertia of the cold plate is much larger compared to the one of the cell, because of the difference in thermal conductivities (k_{cp}=237 $\frac{W}{m \cdot K}$ vs k_{cell}=4.2 $\frac{W}{m \cdot K}$). For this reason also in this case, when the current turns to zero and T_{cell} reaches again T_{cp}, the thermal evolution of the overall system is driven by the cold plate thermal behavior.

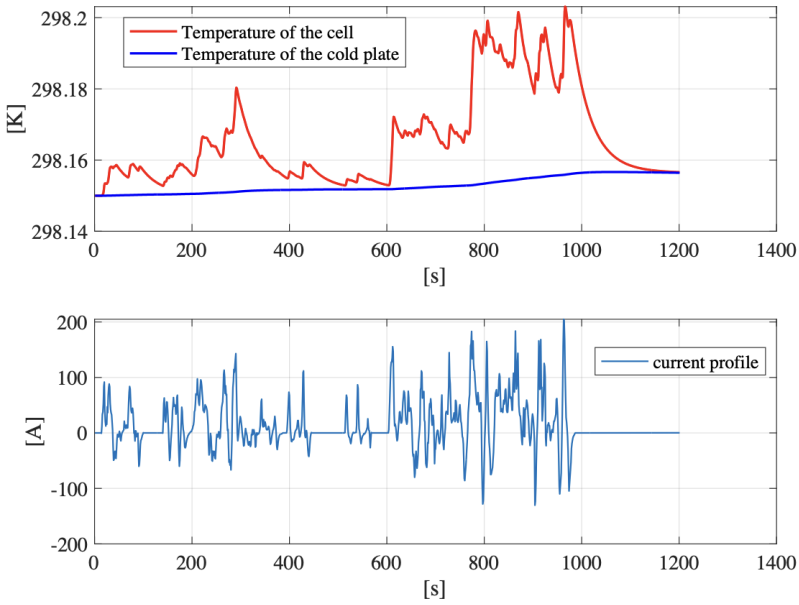

Figure 4.19: Thermal evolution of CALB cell and cold plate with WLTC current profile

The corresponding thermal dissipated powers and energies are represented in figure 4.20. Again $\dot{Q}_{conv}$ is marginal compared to $\dot{Q}_{cond}$, and for this reason the black and the red curves are almost superimposed in both subplots of the figure. However, after reaching the thermal equilibrium between cell and cold plate, the conductive contribution will go to zero (no temperature difference between cell and cold plate is driving heat exchange), and the further temperature decrease will be only related to the convective thermal power dissipated.

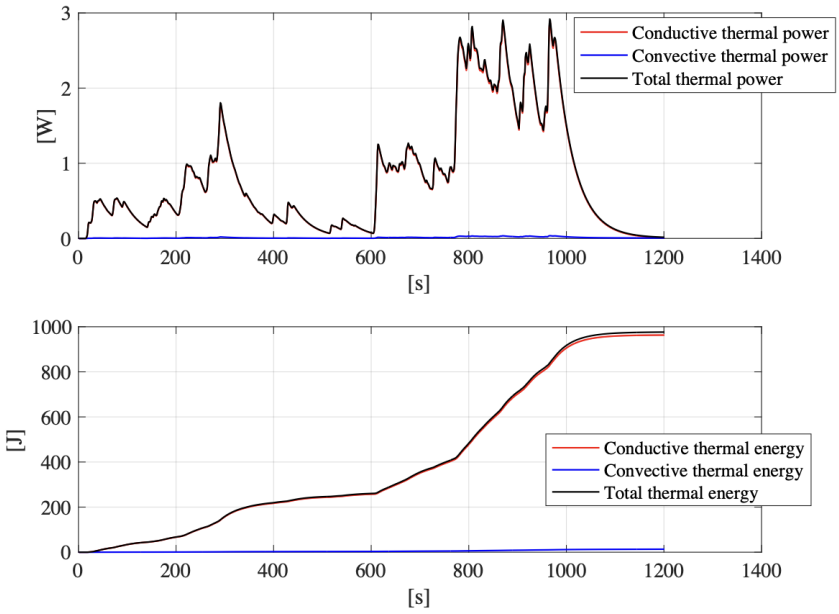

Figure 4.20: Thermal energy and power of CALB dissipated by conduction and convection with WLTC current profile

As previously noted, the thickness and the material of the cold plate had to be estimated from the literature, as no information was provided in the CALB datasheet. However due to the possible uncertainty on the estimations, this project has been concluded by performing a sensitivity analysis on these two parameters, firstly considering the effect of the cold plate material on the overall system's thermal behavior, and then changing the focus on the influence of the plate thickness.
The study has been described only with the first step current profile: the scope of this analysis in fact is to define qualitatively the influence of these parameters on the simulation results, which is independent from the current profile adopted. Considering it also for the WLTC current profile would be redundant since the same conclusions would be obtained.

4.2.2 Sensitivity analysis of cold plate parameters: influence of the material

Sensitivity analysis is defined as a systematic procedure used to determine how the variation in the output of a model can be attributed to the variation in its input parameters, and how the uncertainty on these parameters affects the final results. The first sensitivity analysis has been performed for different possible cold plate materials (thickness in this first analysis is considered constant $s_{cp} = 35mm$) . Even if pure aluminum cold plate has been assumed for the simulation on the CALB, aluminum alloys are more realistic to be considered.
When varying the material, the input parameters to be changed in the simulation script are:

- The density ρ, which is used to estimate the mass of the cold plate
- The thermal conductivity k_{cp}
- The specific heat capacity c_{cp}

These characteristics have been reported in table 4.8 for the four materials considered in the analysis.

Cold plate material	ρ	k_{cp}	c_{cp}
Pure aluminum	$2700\frac{kg}{m^3}$	$237\frac{W}{m\cdot K}$	$903\frac{J}{kg\cdot K}$
2024-T6 alloy	$2770\frac{kg}{m^3}$	$177\frac{W}{m\cdot K}$	$875\frac{J}{kg\cdot K}$
2017A alloy	$2790\frac{kg}{m^3}$	$134\frac{W}{m\cdot K}$	$860\frac{J}{kg\cdot K}$
6082 alloy	$2710\frac{kg}{m^3}$	$174\frac{W}{m\cdot K}$	$896\frac{J}{kg\cdot K}$

Table 4.8: Cold plate material parameters

Together these three parameters determine the thermal inertia of the corresponding material [66]:

$$\lambda = \sqrt{\rho c_{cp} k_{cp}} \tag{4.4}$$

The aim of this section is to define which of the three parameters affects majorly the thermal behavior of the overall system and has the strongest influence on model's outcomes.

According to the results obtained indicated in figure 4.21 it's possible to observe that the lowest temperature rise is registered with pure aluminum cold plate, while the highest increase both of $T_{cell}(t)$ and $T_{cp}(t)$ is obtained for the case of 2017A alloy. Pure aluminum and 2017A have respectively the highest and the lowest thermal conductivity k_{cp} and specific heat capacity c_{cp} while for the densities is exactly the opposite.

Analyzing the other two materials we observe that the temperature rises registered with cold plate made of 2024-T6 alloy and 6082 alloy, are approximately the same despite having different densities, and not so similar specific heat capacities (c_{cp} of 6082 alloy is much closer to the c_{cp} of pure aluminum). This can be justified only by the fact that they have almost identical values of thermal conductivity, with k_{cp} of 6082 alloy slightly lower with respect to 2024-T6, exactly as for the corresponding temperature rises registered. Observing the plot in fact, the curves are ordered according to the thermal conductivity of the materials as indicated by the black arrow.

We can conclude that the thermal behavior of the material is mainly affected by the thermal conductivity, therefore uncertainties on k_{cp} have the strongest influence on the resulting temperature evolution both of cell and cold plate.

In the case of 2017A alloy cold plate, the thermal equilibrium between the cell and the cold plate is reached with a lower rate compared to the aluminum, both during initial steep temperature rise (before the system stabilizes at a constant

temperature difference $T_{cell}(t) - T_{cp}(t)$) and both during temperature decrease after current has turned to zero. In particular in this second transient, with 2017A alloy cold plate $T_{cell} = T_{cp}$ is reached in 367 seconds differently from the transient of 231s of the pure aluminum mentioned in the previous section

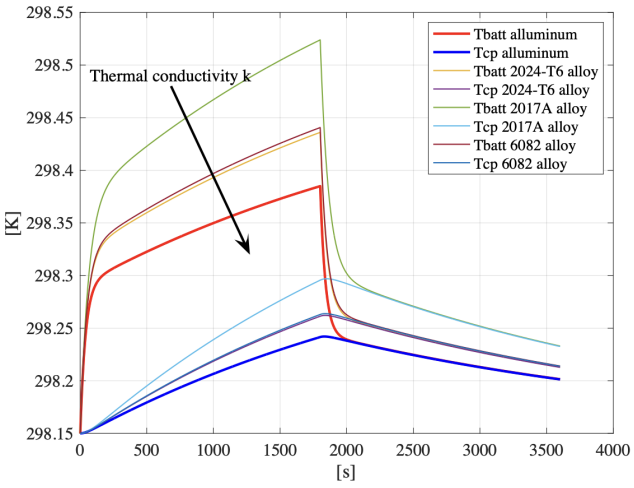

Figure 4.21: Influence of cold plate material on cell and cold plate temperature evolution

The highest is the thermal conductivity, the highest will be the the cooling performances of the plate. For this reason pure aluminum gives the best cooling effectiveness as can be noted in figure 4.20 in the first zoom: the highest is k_{cp} the highest will be the thermal power dissipated by conduction, accordingly to equation 3.24.

The mentioned slower temperature decrease of 2017A alloy is clearly visible in the second zoom: the higher corresponding $\dot{Q}_{cond}$ indicates that $T_{cell}(t) - T_{cp}(t)$ goes to zero less rapidly.

Considering the same initial condition of section 4.2.1 ($T_{cp0} = T_0 = T_{air} = 25°$), assuming that temperature of the air is kept constant, the higher will be the thermal conductivity (so lower temperature rise), lower will be $T_{cell}(t) - T_{air}$ and

as consequence heat dissipated by convection, as can be seen in the third zoom.

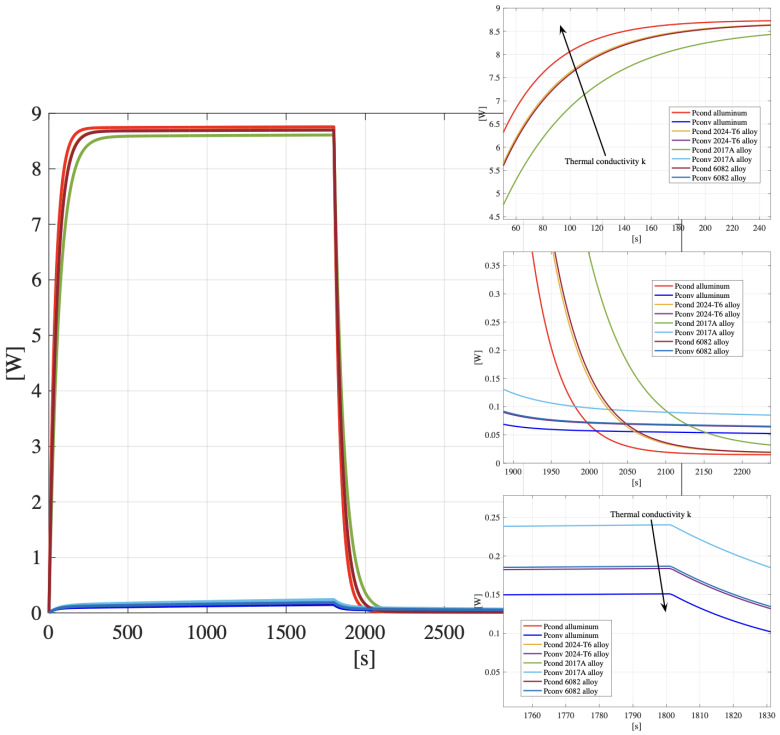

Figure 4.22: Influence of cold plate material on dissipated convective and conductive thermal powers

Having defined the thermal energies as the time integral of the corresponding thermal powers (4.3), analogous results to those discussed with reference to figure 4.22 can be observed in figure 4.23. Specifically, an increase in thermal conductivity results in an increase in conductive thermal energy E_{cond} and a decrease of the convective one E_{conv}.

For the sake of completeness also the influence of the material on the total dissipated power and energy of the system, has been represented and it's reported in appendix C.

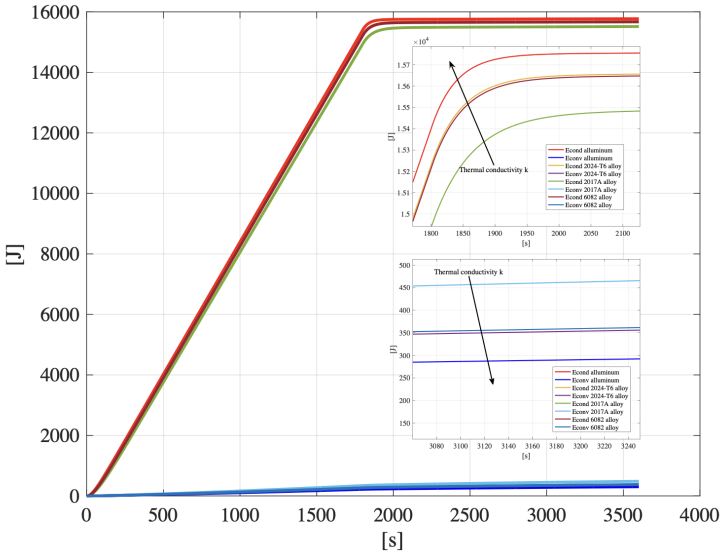

Figure 4.23: Influence of cold plate material on dissipated convective and conductive thermal energies

4.2.3 Sensitivity analysis of cold plate parameters: influence of the thickness

The same analysis can be performed by evaluating the influence of the variation of s_{cp} on the thermal behaviour of the system. Thicknesses of 15mm, 20mm, 25mm, 30mm and 35mm have been considered (cold plate has been assumed of pure aluminum).

Cold plate thickness is a fundamental parameter for the definition of the equivalent conductive R_{cond}, as can be stated from equation 3.49. An increase of s_{cp}, determines thermal resistance rise, since the amount of material through which heat is transferred is much larger. It also reduces the conduction thermal power that the cell can dissipate with the cold plate (see equation 3.24), explaining why in figure 4.24 the highest temperature increase both of T_{cell} and T_{cp} has been obtained by increasing s_{cp}.

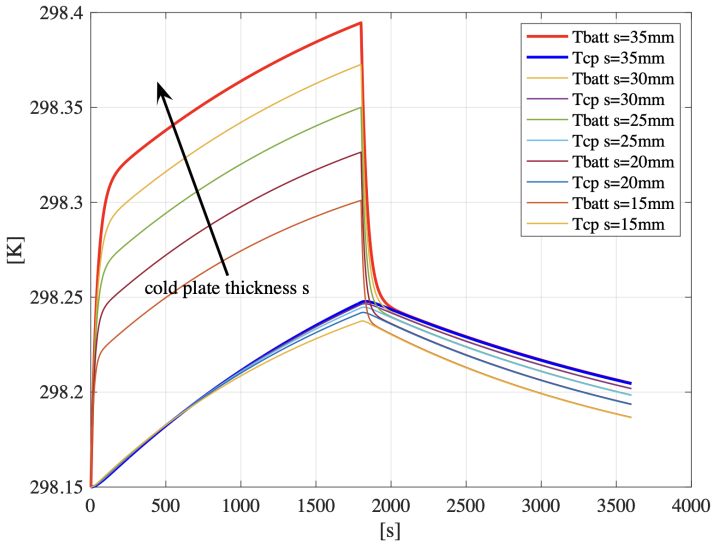

Figure 4.24: Influence of cold plate thickness on cell and cold plate temperature evolution

Once the cell and the cold plate reach the same temperature after the current has turned to zero, the further cooling of the system is related to the convection with the surrounding air, until all the components of the model come back to the initial temperature of 25°.

Focusing on the thermal dissipated power, we can observe in the first zoom of figure 4.25 what has been just affirmed: a lower $\dot{Q}_{cond}$ for larger thicknesses.

From the first and the second zoom of the figure, it's clear how a reduction of s_{cp} leads to a faster thermal transient behavior both during the initial temperature rise and the subsequent temperature decrease. Cold plate thickness in fact is related also to the thermal time constant τ_{th} which is the product of the thermal resistance and the heat capacity. An increase of cold plate thickness in fact leads also to an increase of the cold plate mass, and as consequence of C_{cp}.

But the higher is the thickness of the cold plate, the higher are its lateral surfaces

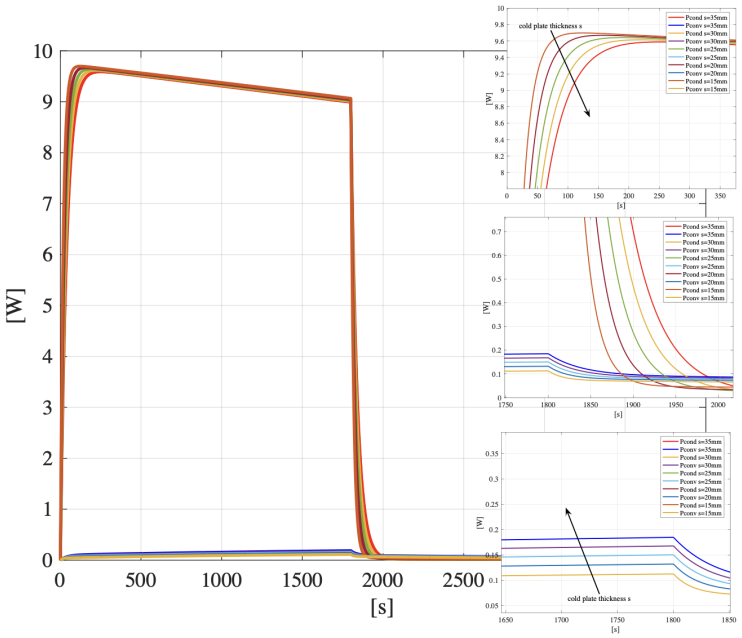

Figure 4.25: Influence of cold plate thickness on dissipated convective and conductive thermal powers

and the overall area in contact with air A_{air-cp}. For this reason in the third zoom of the previous figure an opposite trend of convective thermal dissipated power $\dot{Q}_{conv}$ as function of s_{cp} (with respect to $\dot{Q}_{cond}$), is displayed.
Consequently if considering the total dissipated thermal power (figure C.3 of appendix C), it will be larger for s_{cp}=15mm until conduction between cell and cold plate is occurring. Once the two components reach the same temperature after the current turns to zero, thermal power will be dissipated only by convection and consequently will be larger for s_{cp}=35mm.

As said in the previous section, since the thermal energies are the time integral of the corresponding thermal powers, the same considerations done for figure 4.25 are valid also for figure 4.26. A thicker cold plate leads to reduction of dissipated conductive thermal energy E_{cond} and an increase of convective thermal energy

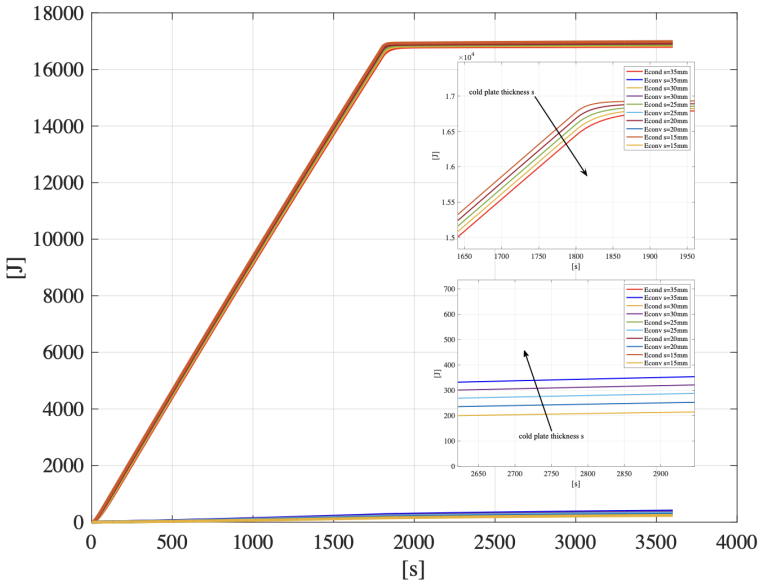

Figure 4.26: Influence of cold plate thickness on dissipated convective and conductive thermal energies

E_{conv}. However the increase of E_{cond} is larger than the reduction of E_{conv} obtained when reducing the cold plate thickness. For this reason the total dissipated thermal energy E_{tot} registered will be the highest in the case of s_{cp}=15mm, as can be observed in figure C.4 of appendix C.

Chapter 5

Conclusion and Future Work

According to the the literature review regarding this technology, battery swap has emerged as a promising technology for solving critical challenges that limit the widespread adoption of electric vehicles. It offers significant advantages with respect to conventional EV charging methods in terms of increased battery lifecycle, reduced charging times and lower vehicle purchasing price.
This thesis presents a comprehensive study on battery swap technology, highlighting the growth of research interest towards this solution and its potentialities.
The key findings of this work can be defined considering the two main objectives of the project:

- Identifying the most suitable battery cell for a low voltage modular swappable battery system that can be implemented on the existing FIAT 500e.
- Defining and validating a complete thermo-electric model to predict the thermal behavior of the cell under different current profiles.

The steps carried out to achieve these goals, are here summarized. Starting from the WLTC range and battery capacity requirements provided, a preliminary battery sizing has been performed. Several cells available on the market have

been evaluated, including those used in existing EVs and cells not yet employed in automotive applications.

For each cell, the corresponding battery arrangements for both urban (frugal configuration) and extra-urban (dual configuration) missions have been defined to meet the abovementioned requirements. The suitable cells were identified as those providing the lightest battery packs based on the calculated arrengements. A lighter battery pack is beneficial in battery swap applications not only for reducing the overall vehicle weight and consequently its energy demand, but also for the ease of handling the pack during the replacement and for the improvement of swapping efficiency considering that the process can be performed much faster if the battery is less heavy.

Among the potential solutions, prismatic cell CALB L221N147A has been selected as the optimal alternative for several reasons including:

i) very high nominal capacity and energy density (few cells required in parallel resulting in lower battery weight: 77.09 kg in frugal configuration and 154.18 kg in dual configuration)

ii) lower costs with respect to the other alternative cells

iii) prismatic geometry easy to be integrated on Fiat 500e

iv) high max c-rates both in charging and discharging (respectively 3.51C and 4.63C)

v) Compact dimensions, ensuring that the battery pack in dual configuration fits within the current battery housing of the 500e, meeting the geometrical constraints.

According to the results provided by the calculation the proposed solution would reduce the weight of the battery pack by 30% compared to the battery meeting the same requirements using the current prismatic SAMSUNG SDI cells of the Fiat 500.

For the second objective a bottom up approach has been followed, starting from

the definition of a simplified thermal model only with convection with surrounding air, up to a complete system which also considers the conduction with a variable temperature cold plate. This thermal model has then been merged together with an equivalent circuit model, capable of describing the electrical behaviour of the cell.

The comprehensive thermo-electric system has been validated populating the model with the parameters of the cylindrical SAMSUNG INR 21700 30T cell. This cell was chosen because of the availability of a complete datasheet (with the exception of thermal conductivity and thickness of the clamps whose values were set according to literature data). This datasheet included also the outcomes of the experimental tests which have been used for the validation.

The comparison of the model's estimated cell temperature with the experimentally measured SAMSUNG one showed a good superposition of the two signals. The resulting maximum absolute error of 0.4° and the calculated RMSE of 0.1315 allowed us to assess the validity of the model in predicting the cell thermal behavior.

Once the validity of the thermo-electric model was established, the model was applied to predict the thermal behaviour of the CALB cell, by simply modifying the input parameters.

As future work, laboratory testing of this cell will be necessary for the missing parameters extrapolation. Validating the model for the CALB prismatic cell would allow for further improvements to the thermo-electric model, moving from the cell model to a battery model, which considers also heat transfers between different cells and the battery housing.

By analyzing the temperature evolution of the overall battery pack under more demanding current profiles that simulate real driving conditions, the most suitable Battery Thermal Management System for battery swap could be defined. If the temperature increase is kept within the optimal range, an air-cooled cold plate

would be the best solution for battery swap applications due to its simplicity, low cost, reduced weight, and no leakage risk during the replacement process. Instead, if the temperature rise is excessive, not guaranteeing battery's correct operation and leading to degradation of the pack, it would be necessary to introduce an integrated liquid-based BTMS that can be swapped with the battery pack without the risk of coolant leakage.

Appendix A

Dual and Frugal Battery Configurations

A.1 BMW i3 (2016) battery cell

Cell Nominal Voltage	**3.68**	**V**
Cell Nominal Capacity	**94**	**Ah**
Cell Specific Energy Density	**175**	**Wh/kg**

Table A.1: BMW i3 (2016) battery cell characteristics [51]

Nominal Capacity	**14.5**	**kWh**
Useable Capacity	**13.1**	**kWh**
Is Useable Capacity > WLTC-city requirement	**NO**	
Cell Specific Energy Density	**175**	**Wh/kg**
Number of Series	**14**	-
Number of Parallels	**3**	-
Number of Cells	**42**	-
Cathode Material	**NMC622**	-
Nominal Voltage	**52**	**V**
Nominal Ampere-Hours	**282**	**Ah**
Battery Mass	**97.67**	**kg**
Battery pack Specific Energy Density	**146.20**	**Wh/kg**

Table A.2: Frugal configuration BMW i3 (2016) battery cells

Nominal Capacity	**29.06**	**kWh**
Useable Capacity	**26.15**	**kWh**
Is Useable Capacity > WLTC-city requirement	**NO**	
Cell Specific Energy Density	**175**	**Wh/kg**
Number of Series	**14**	-
Number of Parallels	**6**	-
Number of Cells	**84**	-
Cathode Material	**NMC622**	-
Nominal Voltage	**52**	**V**
Nominal Ampere-Hours	**564**	**Ah**
Battery Mass	**195.34**	**kg**
Battery pack Specific Energy Density	**146.20**	**Wh/kg**

Table A.3: Dual configuration BMW i3 (2016) battery cells

A.2 BMW i3 (2018) battery cell

Cell Nominal Voltage	**3.68**	**V**
Cell Nominal Capacity	**120**	**Ah**
Cell Specific Energy Density	**200**	**Wh/kg**

Table A.4: BMW i3 (2018) battery cell characteristics [51]

Nominal Capacity	**18.4**	**kWh**
Useable Capacity	**16.6**	**kWh**
Is Useable Capacity > WLTC-city requirement	**YES**	
Cell Specific Energy Density	**200**	**Wh/kg**
Number of Series	**14**	-
Number of Parallels	**3**	-
Number of Cells	**42**	-
Cathode Material	**NMC622**	-
Nominal Voltage	**52**	**V**
Nominal Ampere-Hours	**360**	**Ah**
Battery Mass	**108.21**	**kg**
Battery pack Specific Energy Density	**170.00**	**Wh/kg**

Table A.5: Frugal configuration BMW i3 (2018) battery cells

Nominal Capacity	**36.8**	**kWh**
Useable Capacity	**33.1**	**kWh**
Is Useable Capacity > WLTC-city requirement	**YES**	
Cell Specific Energy Density	**200**	**Wh/kg**
Number of Series	**14**	-
Number of Parallels	**6**	-
Number of Cells	**84**	-
Cathode Material	**NMC622**	-
Nominal Voltage	**52**	**V**
Nominal Ampere-Hours	**720**	**Ah**
Battery Mass	**216.42**	**kg**
Battery pack Specific Energy Density	**170.00**	**Wh/kg**

Table A.6: Dual configuration BMW i3 (2018) battery cells

A.3 KIA Niro battery cell

Cell Nominal Voltage	**3.63**	**V**
Cell Nominal Capacity	**60**	**Ah**
Cell Specific Energy Density	**242.5**	**Wh/kg**

Table A.7: KIA Niro battery cell characteristics [51]

Nominal Capacity	**15.2**	**kWh**
Useable Capacity	**13.7**	**kWh**
Is Useable Capacity > WLTC-city requirement	**NO**	
Cell Specific Energy Density	**242.5**	**Wh/kg**
Number of Series	**14**	-
Number of Parallels	**5**	-
Number of Cells	**70**	-
Cathode Material	**NMC622**	-
Nominal Voltage	**52**	**V**
Nominal Ampere-Hours	**300**	**Ah**
Battery Mass	**73.96**	**kg**
Battery pack Specific Energy Density	**206.13**	**Wh/kg**

Table A.8: Frugal configuration KIA Niro battery cells

Nominal Capacity	**30.5**	**kWh**
Useable Capacity	**27.4**	**kWh**
Is Useable Capacity > WLTC-city requirement	**NO**	
Cell Specific Energy Density	**242.5**	**Wh/kg**
Number of Series	**14**	-
Number of Parallels	**10**	-
Number of Cells	**140**	-
Cathode Material	**NMC622**	-
Nominal Voltage	**52**	**V**
Nominal Ampere-Hours	**600**	**Ah**
Battery Mass	**147.93**	**kg**
Battery pack Specific Energy Density	**206.13**	**Wh/kg**

Table A.9: Dual configuration KIA Niro battery cells

A.4 Volkswagen ID 3 battery cell

Cell Nominal Voltage	**3.65**	**V**
Cell Nominal Capacity	**78**	**Ah**
Cell Specific Energy Density	**161.5**	**Wh/kg**

Table A.10: Volkswagen ID 3 battery cell characteristics [51]

Nominal Capacity	**15.94**	**kWh**
Useable Capacity	**14.3**	**kWh**
Is Useable Capacity > WLTC-city requirement	**YES**	
Cell Specific Energy Density	**161.5**	**Wh/kg**
Number of Series	**14**	-
Number of Parallels	**4**	-
Number of Cells	**56**	-
Cathode Material	**NMC622**	-
Nominal Voltage	**52**	**V**
Nominal Ampere-Hours	**312**	**Ah**
Battery Mass	**116.14**	**kg**
Battery pack Specific Energy Density	**137.28**	**Wh/kg**

Table A.11: Frugal configuration Volkswagen ID 3 battery cells

Nominal Capacity	**31.89**	**kWh**
Useable Capacity	**28.7**	**kWh**
Is Useable Capacity > WLTC-city requirement	**YES**	
Cell Specific Energy Density	**161.5**	**Wh/kg**
Number of Series	**14**	-
Number of Parallels	**8**	-
Number of Cells	**112**	-
Cathode Material	**NMC712**	-
Nominal Voltage	**52**	**V**
Nominal Ampere-Hours	**624**	**Ah**
Battery Mass	**232.28**	**kg**
Battery pack Specific Energy Density	**137.28**	**Wh/kg**

Table A.12: Dual configuration Volkswagen ID 3 battery cells

A.5 CALB L300F177A battery cell

Cell Nominal Voltage	**3.2**	**V**
Cell Nominal Capacity	**177**	**Ah**
Cell Specific Energy Density	**180**	**Wh/kg**

Table A.13: CALB L300F177A battery cell characteristics [50]

Nominal Capacity	**18.12**	**kWh**
Useable Capacity	**16.3**	**kWh**
Is Useable Capacity > WLTC-city requirement	**YES**	
Cell Specific Energy Density	**180**	**Wh/kg**
Number of Series	**16**	-
Number of Parallels	**2**	-
Number of Cells	**32**	-
Cathode Material	**LiFePO4**	-
Nominal Voltage	**52**	**V**
Nominal Ampere-Hours	**354**	**Ah**
Battery Mass	**118.5**	**kg**
Battery pack Specific Energy Density	**153**	**Wh/kg**

Table A.14: Frugal configuration CALB L300F177A battery cells

Nominal Capacity	**36.24**	**kWh**
Useable Capacity	**32.62**	**kWh**
Is Useable Capacity > WLTC-city requirement	**YES**	
Cell Specific Energy Density	**180**	**Wh/kg**
Number of Series	**16**	-
Number of Parallels	**4**	-
Number of Cells	**64**	-
Cathode Material	**LiFePO4**	-
Nominal Voltage	**52**	**V**
Nominal Ampere-Hours	**708**	**Ah**
Battery Mass	**237**	**kg**
Battery pack Specific Energy Density	**153**	**Wh/kg**

Table A.15: Dual configuration CALB L300F177A battery cells

A.6 7914897-NMC battery cell

Cell Nominal Voltage	**3.7**	**V**
Cell Nominal Capacity	**153**	**Ah**
Cell Specific Energy Density	**214**	**Wh/kg**

Table A.16: 7914897-NMC battery cell characteristics [50]

Nominal Capacity	**15.85**	**kWh**
Useable Capacity	**14.26**	**kWh**
Is Useable Capacity > WLTC-city requirement	**YES**	
Cell Specific Energy Density	**214**	**Wh/kg**
Number of Series	**14**	-
Number of Parallels	**2**	-
Number of Cells	**28**	-
Cathode Material	**NMC**	-
Nominal Voltage	**52**	**V**
Nominal Ampere-Hours	**306**	**Ah**
Battery Mass	**87.14**	**kg**
Battery pack Specific Energy Density	**181.9**	**Wh/kg**

Table A.17: Frugal configuration 7914897-NMC battery cells

Nominal Capacity	**31.7**	**kWh**
Useable Capacity	**28.5**	**kWh**
Is Useable Capacity > WLTC-city requirement	**YES**	
Cell Specific Energy Density	**214**	**Wh/kg**
Number of Series	**14**	-
Number of Parallels	**4**	-
Number of Cells	**56**	-
Cathode Material	**NMC**	-
Nominal Voltage	**52**	**V**
Nominal Ampere-Hours	**612**	**Ah**
Battery Mass	**174.3**	**kg**
Battery pack Specific Energy Density	**181.9**	**Wh/kg**

Table A.18: Dual configuration 7914897-NMC battery cells

A.7 CALB L221N113A battery cell

Cell Nominal Voltage	**3.7**	**V**
Cell Nominal Capacity	**113.5**	**Ah**
Cell Specific Energy Density	**233.3**	**Wh/kg**

Table A.19: CALB L221N113A battery cell characteristics [50]

Nominal Capacity	**17.64**	**kWh**
Useable Capacity	**15.87**	**kWh**
Is Useable Capacity > WLTC-city requirement	**YES**	
Cell Specific Energy Density	**233.3**	**Wh/kg**
Number of Series	**14**	-
Number of Parallels	**3**	-
Number of Cells	**42**	-
Cathode Material	**NMC811**	-
Nominal Voltage	**52**	**V**
Nominal Ampere-Hours	**340.5**	**Ah**
Battery Mass	**88.94**	**kg**
Battery pack Specific Energy Density	**198.3**	**Wh/kg**

Table A.20: Frugal configuration CALB L221N113A battery cells

Nominal Capacity	**35.28**	**kWh**
Useable Capacity	**31.75**	**kWh**
Is Useable Capacity > WLTC-city requirement	**YES**	
Cell Specific Energy Density	**233.3**	**Wh/kg**
Number of Series	**14**	-
Number of Parallels	**6**	-
Number of Cells	**84**	-
Cathode Material	**NMC811**	-
Nominal Voltage	**52**	**V**
Nominal Ampere-Hours	**681**	**Ah**
Battery Mass	**177.88**	**kg**
Battery pack Specific Energy Density	**198.3**	**Wh/kg**

Table A.21: Dual configuration CALB L221N113A battery cells

A.8 CALB L173F280A battery cell

Cell Nominal Voltage	**3.65**	**V**
Cell Nominal Capacity	**280**	**Ah**
Cell Specific Energy Density	**188.6**	**Wh/kg**

Table A.22: CALB L173F280A battery cell characteristics [50]

Nominal Capacity	**15.3**	**kWh**
Useable Capacity	**13.8**	**kWh**
Is Useable Capacity > WLTC-city requirement	**NO**	
Cell Specific Energy Density	**188.6**	**Wh/kg**
Number of Series	**15**	-
Number of Parallels	**1**	-
Number of Cells	**15**	-
Cathode Material	**LiFePO4**	-
Nominal Voltage	**52**	**V**
Nominal Ampere-Hours	**280**	**Ah**
Battery Mass	**95.63**	**kg**
Battery pack Specific Energy Density	**160.3**	**Wh/kg**

Table A.23: Frugal configuration CALB L173F280A battery cells

Nominal Capacity	**30.7**	**kWh**
Useable Capacity	**27.63**	**kWh**
Is Useable Capacity > WLTC-city requirement	**YES**	
Cell Specific Energy Density	**188.6**	**Wh/kg**
Number of Series	**15**	-
Number of Parallels	**2**	-
Number of Cells	**30**	-
Cathode Material	**LiFePO4**	-
Nominal Voltage	**52**	**V**
Nominal Ampere-Hours	**560**	**Ah**
Battery Mass	**191.25**	**kg**
Battery pack Specific Energy Density	**160.3**	**Wh/kg**

Table A.24: Dual configuration CALB L173F280A battery cells

A.9 CALB L221N147A battery cell

Cell Nominal Voltage	**3.76**	**V**
Cell Nominal Capacity	**150**	**Ah**
Cell Specific Energy Density	**241**	**Wh/kg**

Table A.25: CALB L221N147A battery cell characteristics [50]

Nominal Capacity	**15.79**	**kWh**
Useable Capacity	**14.21**	**kWh**
Is Useable Capacity > WLTC-city requirement	**YES**	
Cell Specific Energy Density	**241**	**Wh/kg**
Number of Series	**14**	-
Number of Parallels	**2**	-
Number of Cells	**28**	-
Cathode Material	**NMC811**	-
Nominal Voltage	**52**	**V**
Nominal Ampere-Hours	**300**	**Ah**
Battery Mass	**77.09**	**kg**
Battery pack Specific Energy Density	**204.9**	**Wh/kg**

Table A.26: Frugal configuration CALB L221N147A battery cells

Nominal Capacity	**31.58**	**kWh**
Useable Capacity	**28.42**	**kWh**
Is Useable Capacity > WLTC-city requirement	**YES**	
Cell Specific Energy Density	**241**	**Wh/kg**
Number of Series	**14**	-
Number of Parallels	**4**	-
Number of Cells	**56**	-
Cathode Material	**NMC811**	-
Nominal Voltage	**52**	**V**
Nominal Ampere-Hours	**600**	**Ah**
Battery Mass	**154.18**	**kg**
Battery pack Specific Energy Density	**204.9**	**Wh/kg**

Table A.27: Dual configuration CALB L221N147A battery cells

A.10 EVE D21 battery cell

Cell Nominal Voltage	**3.63**	**V**
Cell Nominal Capacity	**52**	**Ah**
Cell Specific Energy Density	**255**	**Wh/kg**

Table A.28: EVE D21 battery cell characteristics [50]

Nominal Capacity	**15.86**	**kWh**
Useable Capacity	**14.27**	**kWh**
Is Useable Capacity > WLTC-city requirement	**YES**	
Cell Specific Energy Density	**255**	**Wh/kg**
Number of Series	**14**	-
Number of Parallels	**6**	-
Number of Cells	**84**	-
Cathode Material	**NMC**	-
Nominal Voltage	**52**	**V**
Nominal Ampere-Hours	**312**	**Ah**
Battery Mass	**73.15**	**kg**
Battery pack Specific Energy Density	**216.75**	**Wh/kg**

Table A.29: Frugal configuration EVE D21 battery cells

Nominal Capacity	**31.71**	**kWh**
Useable Capacity	**28.54**	**kWh**
Is Useable Capacity > WLTC-city requirement	**YES**	
Cell Specific Energy Density	**255**	**Wh/kg**
Number of Series	**14**	-
Number of Parallels	**12**	-
Number of Cells	**168**	-
Cathode Material	**NMC**	-
Nominal Voltage	**52**	**V**
Nominal Ampere-Hours	**624**	**Ah**
Battery Mass	**146.3**	**kg**
Battery pack Specific Energy Density	**216.75**	**Wh/kg**

Table A.30: Dual configuration EVE D21 battery cells

A.11 LEXUS UX 300e battery cell

Cell Nominal Voltage	**3.7**	**V**
Cell Nominal Capacity	**51**	**Ah**
Cell Specific Energy Density	**213**	**Wh/kg**

Table A.31: LEXUS UX 300e battery cell characteristics [51]

Nominal Capacity	**15.85**	**kWh**
Useable Capacity	**14.27**	**kWh**
Is Useable Capacity > WLTC-city requirement	**YES**	
Cell Specific Energy Density	**213**	**Wh/kg**
Number of Series	**14**	-
Number of Parallels	**6**	-
Number of Cells	**84**	-
Cathode Material	**No data**	-
Nominal Voltage	**52**	**V**
Nominal Ampere-Hours	**306**	**Ah**
Battery Mass	**87.55**	**kg**
Battery pack Specific Energy Density	**181.04**	**Wh/kg**

Table A.32: Frugal configuration LEXUS UX 300e battery cells

Nominal Capacity	**31.7**	**kWh**
Useable Capacity	**28.54**	**kWh**
Is Useable Capacity > WLTC-city requirement	**YES**	
Cell Specific Energy Density	**213**	**Wh/kg**
Number of Series	**14**	-
Number of Parallels	**12**	-
Number of Cells	**168**	-
Cathode Material	**NMC**	-
Nominal Voltage	**52**	**V**
Nominal Ampere-Hours	**612**	**Ah**
Battery Mass	**175.1**	**kg**
Battery pack Specific Energy Density	**181.04**	**Wh/kg**

Table A.33: Dual configuration LEXUS UX 300e battery cells

Appendix B

Samsung SDI battery pack

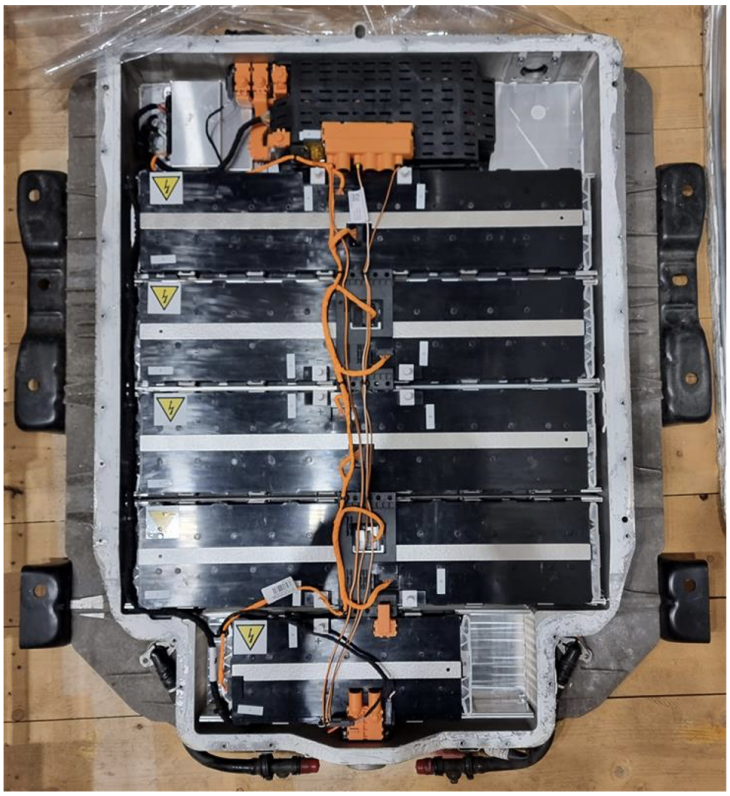

Figure B.1: Fiat 500e battery pack top view

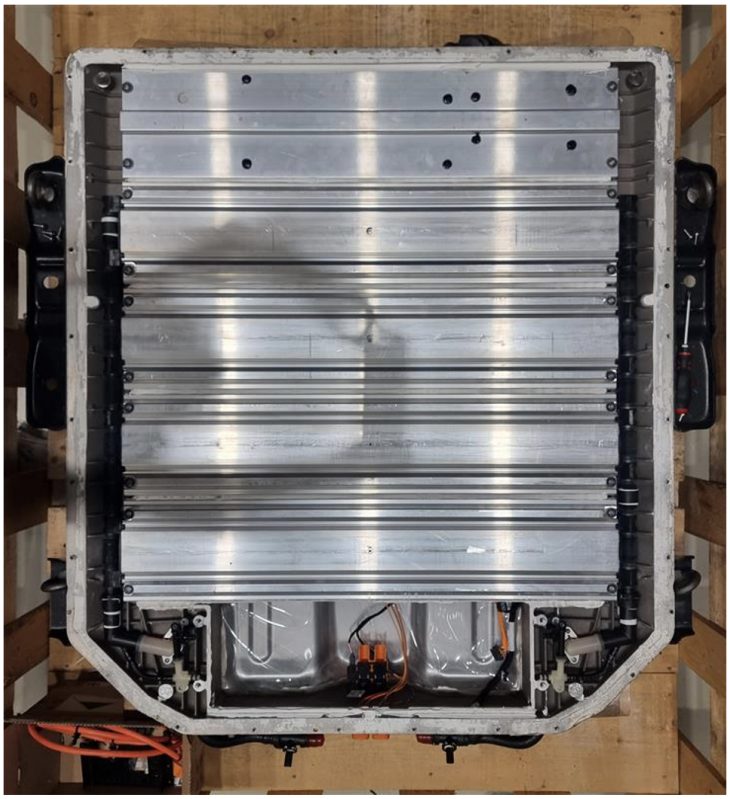

Figure B.2: Fiat 500e battery pack bottom view

Appendix C

Sensitivity analysis

C.1 Effect of cold plate material

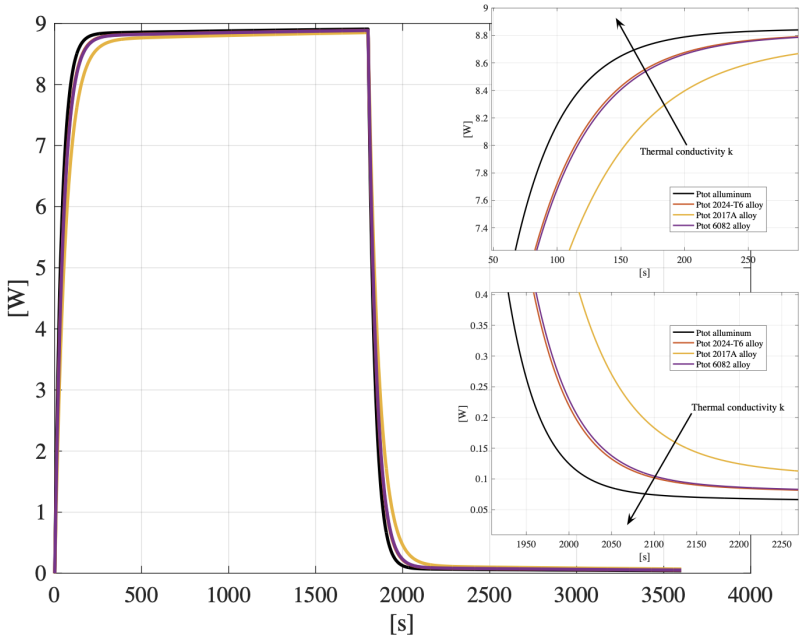

Figure C.1: Influence of cold plate material on total dissipated power $\dot{Q}_{out}$

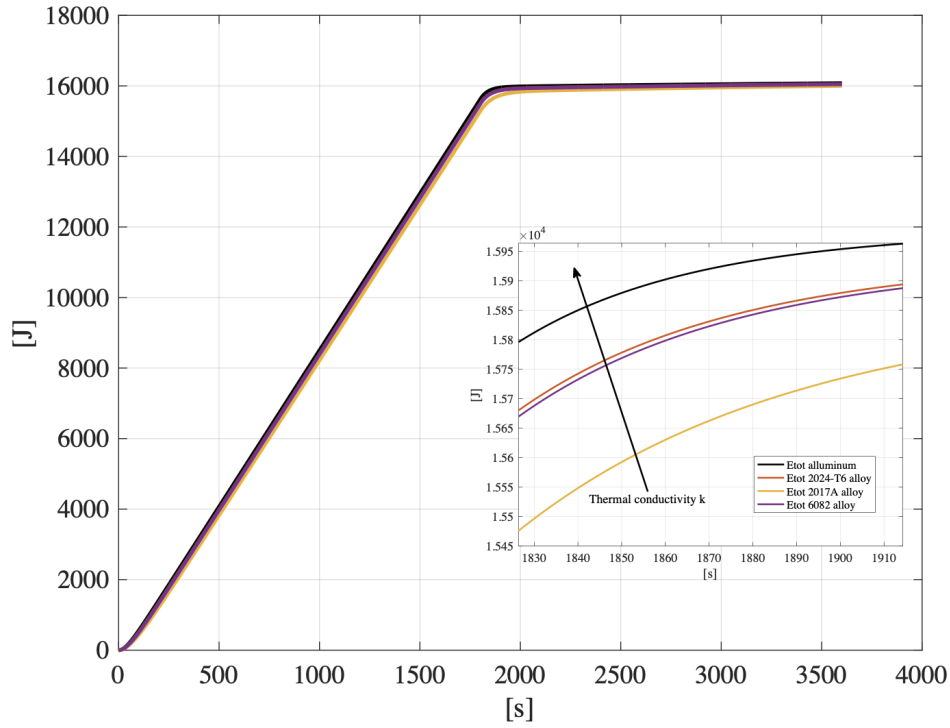

Figure C.2: Influence of cold plate material on total dissipated energy E_{tot}

C.2 Effect of cold plate thickness

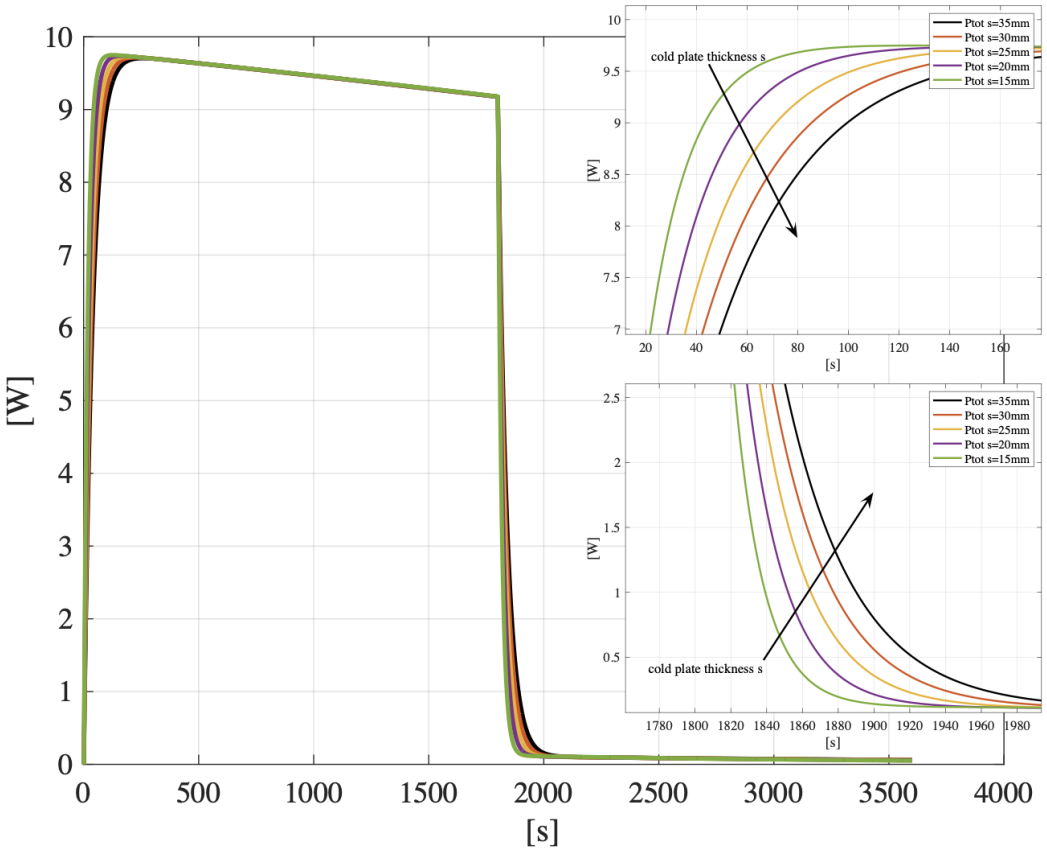

Figure C.3: Influence of cold plate thickness on total dissipated power $\dot{Q}_{out}$

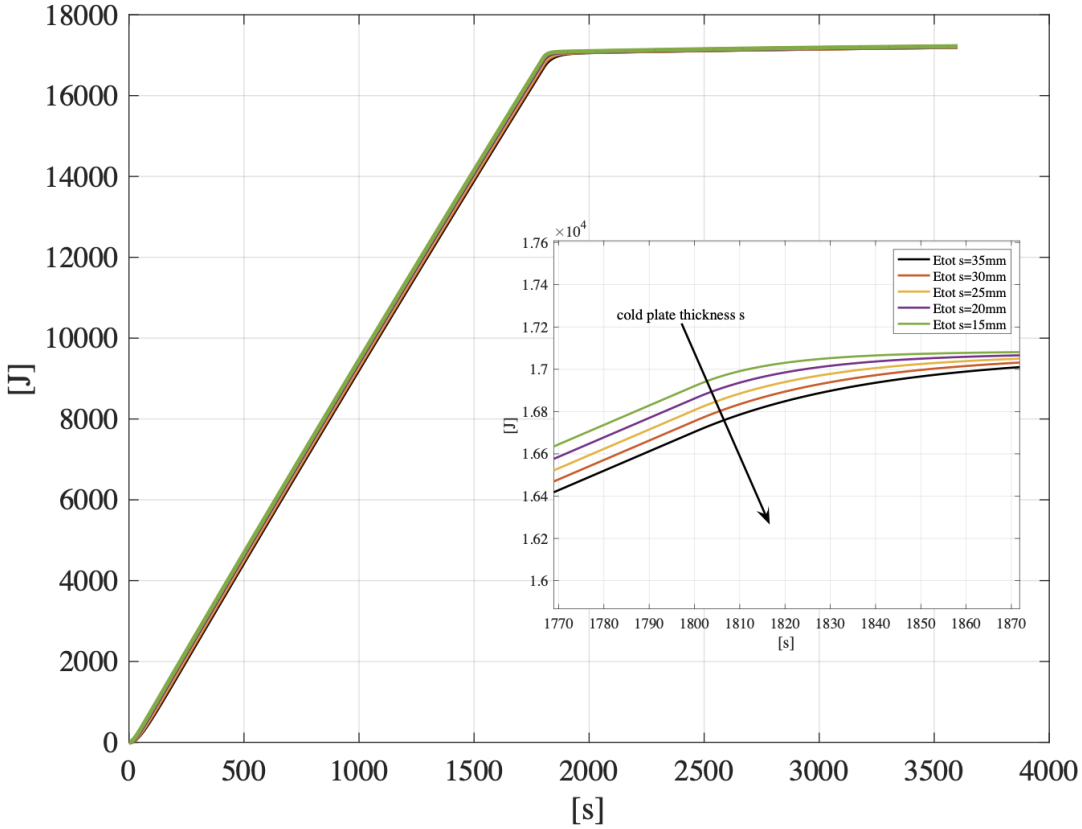

Figure C.4: Influence of cold plate thickness on total dissipated energy E_{tot}

Bibliography

[1] European Union. *CO_2 emission performance standards for cars and vans*. 2024. URL: https://climate.ec.europa.eu/eu-action/transport/road-transport-reducing-co2-emissions-vehicles/co2-emission-performance-standards-cars-and-vans_en (cit. on p. 1).

[2] Centro Nazionale per la Mobilità Sostenibile. *Spoke 2 Sustainable road vehicle*. 2024. URL: https://www.centronazionalemost.it/Spoke2.html (cit. on p. 7).

[3] Till Gnann, Simon Funke, Niklas Jakobsson, Patrick Plötz, Frances Sprei, and Anders Bennehag. «Fast charging infrastructure for electric vehicles: Today's situation and future needs». In: *Transportation Research Part D: Transport and Environment* 62 (2018), pp. 314–329 (cit. on p. 10).

[4] Simon Árpád Funke, Frances Sprei, Till Gnann, and Patrick Plötz. «How much charging infrastructure do electric vehicles need? A review of the evidence and international comparison». In: *Transportation research part D: transport and environment* 77 (2019), pp. 224–242 (cit. on p. 10).

[5] Pierpaolo Dini, Sergio Saponara, and Antonio Colicelli. «Overview on Battery Charging Systems for Electric Vehicles». In: *Electronics* 12.20 (2023), p. 4295 (cit. on p. 11).

[6] Shahram Mohrehkesh and Tamer Nadeem. «Toward a wireless charging for battery electric vehicles at traffic intersections». In: *2011 14th international IEEE conference on intelligent transportation systems (ITSC)*. IEEE. 2011, pp. 113–118 (cit. on p. 12).

[7] Chirag Panchal, Sascha Stegen, and Junwei Lu. «Review of static and dynamic wireless electric vehicle charging system». In: *Engineering science and technology, an international journal* 21.5 (2018), pp. 922–937 (cit. on p. 12).

[8] Qianqian Liu, Chunyu Du, Bin Shen, Pengjian Zuo, Xinqun Cheng, Yulin Ma, Geping Yin, and Yunzhi Gao. «Understanding undesirable anode lithium plating issues in lithium-ion batteries». In: *RSC advances* 6.91 (2016), pp. 88683–88700 (cit. on p. 13).

[9] Ratnakumar V Bugga and Marshall C Smart. «Lithium plating behavior in lithium-ion cells». In: *ECS transactions* 25.36 (2010), p. 241 (cit. on p. 14).

[10] Feyijimi Adegbohun, Annette Von Jouanne, and Kwang Y Lee. «Autonomous battery swapping system and methodologies of electric vehicles». In: *Energies* 12.4 (2019), p. 667 (cit. on pp. 15, 16).

[11] Furkan Ahmad, Mohammad Saad Alam, Ibrahim Saad Alsaidan, and Samir M Shariff. «Battery swapping station for electric vehicles: opportunities and challenges». In: *IET Smart Grid* 3.3 (2020), pp. 280–286 (cit. on p. 18).

[12] Wei Liu, Tobias Placke, and KT Chau. «Overview of batteries and battery management for electric vehicles». In: *Energy Reports* 8 (2022), pp. 4058–4084 (cit. on p. 19).

[13] Shubham Jain, Zaurez Ahmad, Mohammad Saad Alam, and Yasser Rafat. «Battery swapping technology». In: *2020 5th IEEE International Conference on Recent Advances and Innovations in Engineering (ICRAIE)*. IEEE. 2020, pp. 1–4 (cit. on p. 19).

[14] Astha Arora, Mohit Murarka, Dibakar Rakshit, and Sukumar Mishra. «Multiobjective optimal operation strategy for electric vehicle battery swapping station considering battery degradation». In: *Cleaner Energy Systems* 4 (2023), p. 100048 (cit. on p. 20).

[15] Hao Wu, Grantham Kwok Hung Pang, King Lun Choy, and Hoi Yan Lam. «An optimization model for electric vehicle battery charging at a battery swapping station». In: *IEEE Transactions on Vehicular Technology* 67.2 (2017), pp. 881–895 (cit. on p. 20).

[16] Mushfiqur R Sarker, Hrvoje Pandžić, and Miguel A Ortega-Vazquez. «Electric vehicle battery swapping station: Business case and optimization model». In: *2013 International Conference on Connected Vehicles and Expo (ICCVE)*. IEEE. 2013, pp. 289–294 (cit. on p. 21).

[17] Sujie Shao, Shaoyong Guo, and Xuesong Qiu. «A mobile battery swapping service for electric vehicles based on a battery swapping van». In: *Energies* 10.10 (2017), p. 1667 (cit. on p. 21).

[18] Xi Chen, Kai Xing, Feng Ni, Yujie Wu, and Yongxiang Xia. «An electric vehicle battery-swapping system: Concept, architectures, and implementations». In: *IEEE Intelligent Transportation Systems Magazine* 14.5 (2021), pp. 175–194 (cit. on p. 23).

[19] Hao Wu. «A survey of battery swapping stations for electric vehicles: Operation modes and decision scenarios». In: *IEEE Transactions on Intelligent Transportation Systems* 23.8 (2021), pp. 10163–10185 (cit. on p. 24).

[20] AM Vallera, PM Nunes, and MC Brito. «Why we need battery swapping technology». In: *Energy Policy* 157 (2021), p. 112481 (cit. on pp. 24, 25).

[21] Vedran Bobanac, Hrvoje Pandzic, and Tomislav Capuder. «Survey on electric vehicles and battery swapping stations: Expectations of existing and future EV owners». In: *2018 IEEE International Energy Conference (ENERGYCON)*. IEEE. 2018, pp. 1–6 (cit. on p. 25).

[22] Jignesh Sindha, Jagruti Thakur, and Mutayab Khalid. «The economic value of hybrid battery swapping stations with second life of batteries». In: *Cleaner Energy Systems* 5 (2023), p. 100066 (cit. on p. 26).

[23] Charles-Victor Hémery. «Studies of thermal phenomena in Li-ion batteries». In: *University of Grenoble* (2013) (cit. on p. 26).

[24] Marwa Mahmoud Hamed, A El-Tayeb, Ibrahim Moukhtar, AZ El Dein, and Esam H Abdelhameed. «A review on recent key technologies of lithium-ion battery thermal management: External cooling systems». In: *Results in Engineering* 16 (2022), p. 100703 (cit. on pp. 26, 29, 30).

[25] Qian Huang, Manming Yan, and Zhiyu Jiang. «Thermal study on single electrodes in lithium-ion battery». In: *Journal of Power Sources* 156.2 (2006), pp. 541–546 (cit. on p. 27).

[26] Rami Sabbah, R Kizilel, JR Selman, and S Al-Hallaj. «Active (air-cooled) vs. passive (phase change material) thermal management of high power lithium-ion packs: Limitation of temperature rise and uniformity of temperature distribution». In: *Journal of power sources* 182.2 (2008), pp. 630–638 (cit. on pp. 27, 33).

[27] Yuqian Fan, Yun Bao, Chen Ling, Yanyan Chu, Xiaojun Tan, and Shuting Yang. «Experimental study on the thermal management performance of air cooling for high energy density cylindrical lithium-ion batteries». In: *Applied Thermal Engineering* 155 (2019), pp. 96–109 (cit. on pp. 28, 29).

[28] Liwu Fan, JM Khodadadi, and AA Pesaran. «A parametric study on thermal management of an air-cooled lithium-ion battery module for plug-in hybrid electric vehicles». In: *Journal of Power Sources* 238 (2013), pp. 301–312 (cit. on p. 29).

[29] Shahabeddin K Mohammadian and Yuwen Zhang. «Thermal management optimization of an air-cooled Li-ion battery module using pin-fin heat sinks for hybrid electric vehicles». In: *Journal of Power Sources* 273 (2015), pp. 431–439 (cit. on p. 29).

[30] Kai Chen, Yiming Chen, Zeyu Li, Fang Yuan, and Shuangfeng Wang. «Design of the cell spacings of battery pack in parallel air-cooled battery thermal management system». In: *International Journal of Heat and Mass Transfer* 127 (2018), pp. 393–401 (cit. on p. 29).

[31] Yuanwang Deng, Changling Feng, E Jiaqiang, Hao Zhu, Jingwei Chen, Ming Wen, and Huichun Yin. «Effects of different coolants and cooling strategies on the cooling performance of the power lithium ion battery system: A review». In: *Applied Thermal Engineering* 142 (2018), pp. 10–29 (cit. on p. 30).

[32] Anisha and Anil Kumar. «Identification and mitigation of shortcomings in direct and indirect liquid cooling-based battery thermal management system». In: *Energies* 16.9 (2023), p. 3857 (cit. on p. 31).

[33] Gang Zhao, Xiaolin Wang, Michael Negnevitsky, and Chengjiang Li. «An up-to-date review on the design improvement and optimization of the liquid-cooling battery thermal management system for electric vehicles». In: *Applied Thermal Engineering* 219 (2023), p. 119626 (cit. on p. 31).

[34] Kunal Sandip Garud, Le Duc Tai, Seong-Guk Hwang, Nghia-Huu Nguyen, and Moo-Yeon Lee. «A review of advanced cooling strategies for battery thermal management systems in electric vehicles». In: *Symmetry* 15.7 (2023), p. 1322 (cit. on pp. 31, 33, 34).

[35] Yang Li, Zhifu Zhou, Leiming Hu, Minli Bai, Linsong Gao, Yulong Li, Xuanyu Liu, Yubai Li, and Yongchen Song. «Experimental studies of liquid immersion cooling for 18650 lithium-ion battery under different discharging conditions». In: *Case Studies in Thermal Engineering* 34 (2022), p. 102034 (cit. on p. 31).

[36] Giuseppe Volpe, Yew Chuan Chong, David Alan Staton, and Mircea Popescu. «Thermal management of a racing e-machine». In: *2018 XIII International Conference on Electrical Machines (ICEM)*. IEEE. 2018, pp. 2689–2694 (cit. on p. 32).

[37] Hadi Bashirpour-Bonab. «Thermal behavior of lithium batteries used in electric vehicles using phase change materials». In: *International Journal of Energy Research* 44.15 (2020), pp. 12583–12591 (cit. on p. 33).

[38] Zhonghao Rao and Shuangfeng Wang. «A review of power battery thermal energy management». In: *Renewable and Sustainable Energy Reviews* 15.9 (2011), pp. 4554–4571 (cit. on p. 33).

[39] Adil Wazeer, Apurba Das, Chamil Abeykoon, Arijit Sinha, and Amit Karmakar. «Phase change materials for battery thermal management of electric and hybrid vehicles: A review». In: *Energy Nexus* 7 (2022), p. 100131 (cit. on p. 33).

[40] Dingsong Cui, Zhenpo Wang, Peng Liu, Shuo Wang, David G Dorrell, Xiaohui Li, and Weipeng Zhan. «Operation optimization approaches of electric vehicle battery swapping and charging station: A literature review». In: *Energy* 263 (2023), p. 126095 (cit. on p. 35).

[41] Benjamin K Sovacool, Lance Noel, and Renato J Orsato. «Stretching, embeddedness, and scripts in a sociotechnical transition: Explaining the failure of electric mobility at Better Place (2007–2013)». In: *Technological Forecasting and Social Change* 123 (2017), pp. 24–34 (cit. on p. 35).

[42] Dan Mihalascu. *CATL Opens Its First Battery Swapping Stations In China*. 2022. URL: https://insideevs.com/news/580916/catl-opens-its-first-battery-swapping-stations-china/ (cit. on p. 36).

[43] Shuxia Yang, Ruoyang Li, and Jialin Li. «"Separation of Vehicle and Battery" of Private Electric Vehicles and Customer Delivered Value: Based on the Attempt of 2 Chinese EV Companies». In: *Sustainability* 12.5 (2020), p. 2042 (cit. on p. 36).

[44] *Stellantis and Ample Establish Partnership to Leverage Ample's Modular Battery Swapping Technology for Use in Stellantis Electric Vehicles*. December 2023. URL: https://www.media.stellantis.com/nl-nl/corporate-communications/press/stellantis-and-ample-establish-partnership-to-leverage-ample-s-modular-battery-swapping-technology-for-use-in-stellantis-electric-vehicles (cit. on p. 37).

[45] Shantanu Bhattacharya and Lipika Bhattacharya. «NIO's Battery-as-a-Service strategy». In: (2022) (cit. on p. 37).

[46] Alessandro Pisano, Manuel Saba, and Jair Arrieta Baldovino. «A Critical Review of NIO's Business Model». In: *World Electric Vehicle Journal* 14.9 (2023), p. 251 (cit. on p. 37).

[47] Evvy Kartini and Carla Theresa Genardy. «The future of all solid state battery». In: *IOP Conference Series: Materials Science and Engineering*. Vol. 924. 1. IOP Publishing. 2020, p. 012038 (cit. on p. 37).

[48] Mark Kane. *China: NIO Reports 4 Millionth EV Battery Swap*. 2021. URL: https://insideevs.com/news/537644/nio-4-million-battery-swaps (cit. on p. 39).

[49] *NIO Power Swap Station 4.0 Now Operational*. June 2024. URL: https://www.nio.com/news/nio-pss-4.0 (cit. on p. 39).

[50] *Evlithium.com*. URL: https://www.evlithium.com/ (cit. on pp. 44, 56, 116–121).

[51] *Batterydesign.net*. URL: https://www.batterydesign.net/benchmarking-battery-pack/ (cit. on pp. 44, 45, 47, 50, 111, 113–115, 122).

[52] Putri Nur Halimah, Samuel Rahardian, and Bentang Arief Budiman. «Battery cells for electric vehicles». In: *International Journal of Sustainable Transportation Technology* 2.2 (2019), pp. 54–57 (cit. on p. 51).

[53] Rekabra Youssef, Jiacheng He, Mohsen Akbarzadeh, Joris Jaguemont, Lysander De Sutter, Maitane Berecibar, and Joeri Van Mierlo. «Investigation of thermal behavior of large lithium-ion prismatic cell in natural air convection». In: *2020 9th International Conference on Renewable Energy Research and Application (ICRERA)*. IEEE. 2020, pp. 43–47 (cit. on p. 58).

[54] Piyatida Trinuruk, Warongkorn Onnuam, Nutthanicha Senanuch, Chinnapat Sawatdeejui, Papangkorn Jenyongsak, and Somchai Wongwises. «Experimental and numerical studies on the effect of lithium-ion batteries' shape and chemistry on heat generation». In: *Energies* 16.1 (2022), p. 264 (cit. on pp. 58, 59).

[55] Xiaogang Wu, Siyu Lv, and Jizhong Chen. «Determination of the optimum heat transfer coefficient and temperature rise analysis for a lithium-ion battery under the conditions of Harbin city bus driving cycles». In: *Energies* 10.11 (2017), p. 1723 (cit. on p. 58).

[56] Mohsen Akbarzadeh, Theodoros Kalogiannis, Joris Jaguemont, Jiacheng He, Lu Jin, Maitane Berecibar, and Joeri Van Mierlo. «Thermal modeling of a high-energy prismatic lithium-ion battery cell and module based on a new thermal characterization methodology». In: *Journal of Energy Storage* 32 (2020), p. 101707 (cit. on p. 59).

[57] Clemente Capasso, Luigi Iannucci, Stanislao Patalano, Ottorino Veneri, and Ferdinando Vitolo. «Design approach for electric vehicle battery packs based on experimentally tested multi-domain models». In: *Journal of Energy Storage* 77 (2024), p. 109971 (cit. on p. 60).

[58] Çengel Yunus A. *Termodinamica e trasmissione del calore*. McGraw Hill Italia, 2020 (cit. on pp. 60, 61).

[59] Joris Jaguemont, Mohsen Sokkeh, Sazzad Hosen, Lu Jin, Geng Qiao, Theodoros Kalogiannis, and Joeri van Mierlo. «1D-thermal analysis and electro-thermal modeling of prismatic-shape LTO and NMC batteries». In: *2019 IEEE Vehicle Power and Propulsion Conference (VPPC)*. IEEE. 2019, pp. 1–5 (cit. on p. 60).

[60] Fen Zhu, Heng Yan, Liangde Liu, and Xiangyun Liu. «Simulation of thermal behavior of a lithium-ion battery». In: *2016 5th International Conference on Sustainable Energy and Environment Engineering (ICSEEE 2016)*. Atlantis Press. 2016, pp. 528–532 (cit. on p. 61).

[61] Edgar Ramírez-Laboreo, Carlos Sagüés, and Sergio Llorente. «Thermal modeling, analysis and control using an electrical analogy». In: *22nd Mediterranean Conference on Control and Automation*. IEEE. 2014, pp. 505–510 (cit. on p. 62).

[62] Manh-Kien Tran, Andre DaCosta, Anosh Mevawalla, Satyam Panchal, and Michael Fowler. «Comparative study of equivalent circuit models performance in four common lithium-ion batteries: LFP, NMC, LMO, NCA». In: *Batteries* 7.3 (2021), p. 51 (cit. on p. 72).

[63] *The MathWorks Inc., MATLAB version R2024a, Equivalent Circuit Battery.* URL: `https://it.mathworks.com/help/autoblks/ref/equivalentcircuitbattery.html` (cit. on p. 72).

[64] Phillip Kollmeyer and Michael Skells. «Samsung INR21700 30T 3Ah Li-ion Battery Data». In: *Mendeley Data* (2020) (cit. on p. 76).

[65] Pietro Ronzio. «Thermal model of Li-ion battery based on a single temperature lumped parameter model». MA thesis. Politecnico di Torino, 2022 (cit. on p. 78).

[66] J Wang, RL Bras, G Sivandran, and RG Knox. «A simple method for the estimation of thermal inertia». In: *Geophysical Research Letters* 37.5 (2010) (cit. on p. 100).